Technology and device development for active/passive integration on InP_based membrane on Si (IMOS)

Citation for published version (APA):
Zhang, R. (2013). *Technology and device development for active/passive integration on InP_based membrane on Si (IMOS)*. [Phd Thesis 1 (Research TU/e / Graduation TU/e), Electrical Engineering]. Technische Universiteit Eindhoven. https://doi.org/10.6100/IR757861

DOI:
10.6100/IR757861

Document status and date:
Published: 01/01/2013

Document Version:
Publisher’s PDF, also known as Version of Record (includes final page, issue and volume numbers)

Please check the document version of this publication:

• A submitted manuscript is the version of the article upon submission and before peer-review. There can be important differences between the submitted version and the official published version of record. People interested in the research are advised to contact the author for the final version of the publication, or visit the DOI to the publisher's website.
• The final author version and the galley proof are versions of the publication after peer review.
• The final published version features the final layout of the paper including the volume, issue and page numbers.

Link to publication

General rights
Copyright and moral rights for the publications made accessible in the public portal are retained by the authors and/or other copyright owners and it is a condition of accessing publications that users recognise and abide by the legal requirements associated with these rights.

- Users may download and print one copy of any publication from the public portal for the purpose of private study or research.
- You may not further distribute the material or use it for any profit-making activity or commercial gain
- You may freely distribute the URL identifying the publication in the public portal.

If the publication is distributed under the terms of Article 25fa of the Dutch Copyright Act, indicated by the “Taverne” license above, please follow below link for the End User Agreement:

www.tue.nl/taverne

Take down policy
If you believe that this document breaches copyright please contact us at:

openaccess@tue.nl

providing details and we will investigate your claim.

Download date: 17. Nov. 2023

Technology and Device Development for Active/Passive integration on InP_based Membrane on Si (IMOS)

PROEFSCHRIFT

ter verkrijging van de graad van doctor aan de
Technische Universiteit Eindhoven, op gezag van de
rector magnificus, prof.dr.ir. C.J. van Duijn, voor een
commissie aangewezen door het College voor
Promoties in het openbaar te verdedigen
op donderdag 5 september 2013 om 16.00 uur

door

Rui Zhang

geboren te Shaanxi, China

Dit proefschrift is goedgekeurd door de promotor:

prof.dr.ir. M.K. Smit

Copromotor:
dr. J.J.G.M. van der Tol

This research printed in this thesis was supported by the European FP7 project Heterogeneous InP on Silicon Technology for Optical Routing and LogIC Hisand(HISTORIC) under grant number 223876 and the NRC photonics grant.

Printed by Proefschriftmaken.nl || Uitgeverij BOXPress
Published by Uitgeverij BOXPress, Oisterwijk

A catalogue record is available from the Eindhoven University of Technology Library.

Technology and Device Development for Active/Passive integration on InP_based Membrane on Si (IMOS) / by Rui Zhang. – Eindhoven: Technische Universiteit Eindhoven, 2013.
Proefschrift.-ISBN: 978-90-386-3426-5
NUR 959

Subject headings: integrated circuits / photonic integrated circuits / III-V semiconductors / semiconductor lasers / passive components / active-passive integration / AlInAs oxidation / quantum well / photonic crystal

To my families

Table of Contents

Chapter 1

Introduction

"If I have seen further, it is by standing on the shoulders of giants", as said by Sir Isaac Newton, the great genius of human beings. Since science is always evolving, no one can just move forward without understanding progress of the previous researchers. Therefore the introduction of this thesis first goes back to mid-20th century and starts from the groundbreaking invention of Integrated circuits (ICs). Next, in Section 1.2, the next generation of ICs, the photonic integrated circuits (PICs) are introduced. These should help their electronic counterparts to cope with fundamental problems as the size of electronic ICs are getting smaller and meanwhile the speed is getting faster. In Section 1.3, InP-based membrane on Si (IMOS), which is an integration platform combining the best of electronic and photonic ICs, is presented. In Section 1.4, various types of active/passive integration techniques for the IMOS platform are presented and compared. Finally Section 1.5 gives a brief overview of the structure of this thesis.

1.1 Integrated circuits

Integrated Circuits (ICs), which is a breakthrough in semiconductors' development in the mid 20th century, have reshaped our world completely. They are used in virtually all electronic equipment today and have revolutionized our world. Computers, smart phones and tablets and many other digital home appliances, which are now integrated parts of modern societies, would not be possible without the first invention of a simple integrated circuit (see Fig. 1.1) made by Jack Kilby at Texas Instruments in 1958.

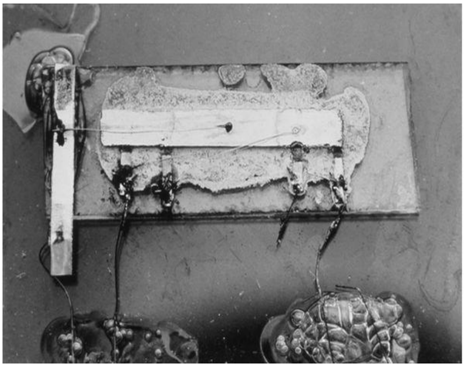
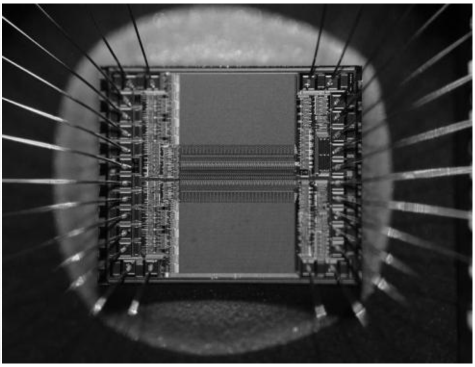

Figure 1.1:The first IC by Jack Kilby [1.1]. Figure 1.2: A common modern IC with an area of 5x4 mm^2 .

The realization of this first integrated circuit showed that semiconductor devices could perform the same functions as vacuum tubes. The integration of large numbers of tiny transistors into a small chip (see Fig 1.2) was an enormous improvement over the manual assembly of circuits using discrete electronic components. ICs have three main advantages over discrete compounds: low cost, ultra small footprint and high performance. Cost can be low because the chips, with all their components, can be printed as a single unit by photolithography rather than being constructed one by one. Furthermore, since everything can be integrated on a single chip, the size of the devices can be made smaller and meanwhile cheaper. Finally the performance is high because the components can switch quickly and they consume less power than their discrete counterparts, because of their small size and the close proximity of the components. Moreover, the IC's mass production capability, reliability and the building-block approach of the circuit design ensures a rapid adoption of standardized ICs to various systems [1.2]. Therefore together with the rise of digital processing, ICs have gradually taken over the position of vacuums tubes and became the dominant element for data processing.

For the last 50 years, integration complexity has been increasing from "small-scale integration (SSI)", with only a few transistors, to "very large-scale integration (VLSI)", having billions of transistor per chip. This trend was noticed by Gorden Moore in 1965, who basically stated that the number of transistors that can be placed on an integrated circuit doubles approximately every two years. Moore's Law has been surprisingly accurate for almost half a century and is expected to continue until at least 2020 [1.3].

However, many challenges emerge as we shrink device sizes of electronic ICs even further. First of all, the information transmission rate using purely electronic means is fundamentally limited: as the frequency of an electrical signal propagating through a conductor increases, the impedance of the conductor also increases, thus the propagation characteristics of the electrical wire become less favorable [1.4]. Secondly, following Moore's law, the miniaturization of the micro-processors will continue and this will result in a dense packaging. However, as the size getting smaller, the parasitic capacitance and resistance of the metal wires will also increase, which subsequently increases the dissipated power density. Consequently, the power efficiency of the chip is limited. Currently, the fundamental limit of the electrical interconnect is considered as one of the major limitations to maintain Moore's law. Finally, as the amount of the information processed in the computer microchip increases, the communication delay between the different ports of the chip must be minimized in order to process the information sufficiently fast. Nowadays, the delay due to the communication between the ports is getting so much that it has almost approached the delay due to the computation itself.

1.2 Photonic integrated circuits

Photonic integrated circuits provide potential solutions to help its electronic counterpart to cope with these problems and to maintain Moore’s law even further. First of all, for most optical materials used in optical communications and photonic devices, the useful frequency window falls in the visible and near-infrared range of the electromagnetic spectrum, which corresponds to light frequencies in the range of 150-800 THz, which is much more than the frequency used in electrical transmission. This high frequency gives the possibility of higher modulation frequencies which can lead to higher bit rates [1.5]. Secondly, since the photonic devices are manufactured from standard electronic materials, complex hybrid devices can be constructed from side by side integration of the photonic and electronic devices. For instance the metallic wires which give high parasitic capacitance and resistance as the size getting smaller, can be replaced by a photonic membrane on top of the Complementary Metal Oxide Semiconductor (CMOS) circuit to provide the high-speed on-chip data transport. This will greatly alleviate the negative effect of the parasitic capacitance of the small metal wires and decrease power dissipation.

Photonic integrated circuits can be realized with different semiconductor material systems, such as Silicon On Insulator (SOI) and Indium Phosphide (InP). The SOI platform, which is commonly called Si photonics, seems to be an ideal candidate since the same material is also the standard material for electronic ICs. Furthermore, due to the strong optical confinement caused by the high refractive index difference between Si (n=3.5) and SiO_2 (n=1.5), quite small passive components such as narrow waveguides and ring resonators with high quality factors have already been presented [1.6].

Unfortunately, Si is born with an intrinsic disadvantage: an indirect band gap, which means that it is intrinsically difficult to realize active functions such as light generation and amplification in the SOI Platform.

InP photonics enables light generation, amplification, propagation and detection at telecom wavelengths. Devices having these functionalities can be integrated in a single chip to maximize the efficiency and the speed of the optical communication network. Classic InP photonics confine light by the refractive index difference between InGaAsP and InP (See Fig.1.3). However, since this refractive index difference is quite small, the layer thickness has to be much larger compared to the SOI platform, in order to confine the light within the core layer. Moreover, since the optical confinement is less, the size of the InP PIC components is relatively large compared to the SOI platform. This ultimately limits the integration complexity of InP photonics.

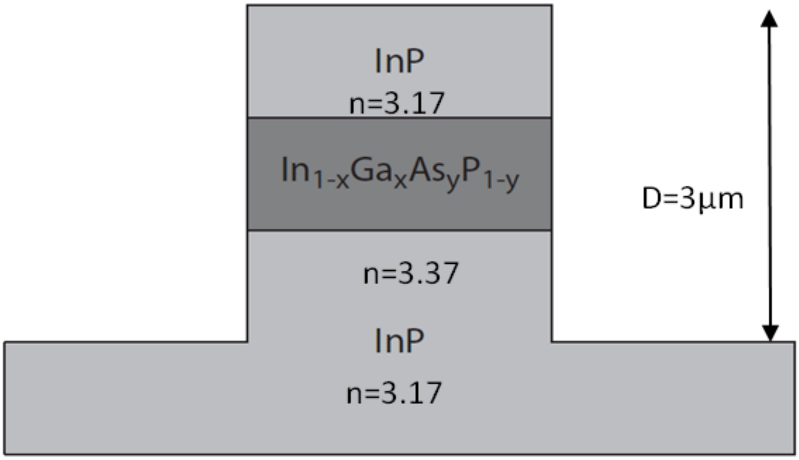

Figure 1.3: Schematic representation of a ridge waveguide in the classic InP platform .

1.3 The evolution to IMOS

In this thesis, we describe a new approach: An InP-based Membrane on Silicon (IMOS) which proposes to use an InP-membrane bonded on a Si wafer by a bonding layer of the polymer benzocyclobutene (BCB) (see Fig.1.4).

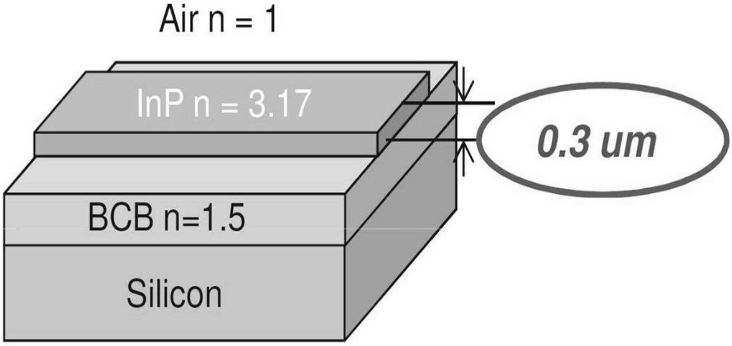

Figure.1.4: Schematic view of the IMOS platform

This platform brings a number of advantages in comparison to the classic InP platform. First of all, IMOS keeps the major advantages of InP-based photonics; both passive and active functions can be realised in the InP-based material system. Secondly, it also has one of the key features of Si photonics: a high vertical refractive index contrast. This basically means that light can be confined in an order of magnitude thinner core layer, compared to the classic InP platform(See Fig.1.4). This high index contrast and the small thickness of IMOS will allow the realization of much smaller devices. In Chapter 2, a series of realized small photonic components will be presented. Furthermore, due to the use of bonding BCB layer, there is a large flexibility with respect to the silicon carrier [1.7-1.8]. Any surface morphology can be possible, which makes this approach potentially a universal approach to replace the metal wires for providing the high-speed on-chip data transport and be fully integrated with CMOS. Last but not least, this platform is potentially compatible with CMOS which makes it possible to use the mature and advanced IC fabrication.

1.4 Active/Passive integration for IMOS platform

To develop a platform for photonic integration, active devices such as lasers and amplifiers, should be integrated together with passive components, such as waveguides and splitters. In this thesis, “active” refers to a material whose band gap energy is less than or comparable to the photon energy, for example the gain medium of a laser or amplifier, the absorbing layer of a waveguide photo-detector, or a medium used in an electro-absorption modulator. Passive components have a band gap energy substantially greater than the propagating photon energy, in order to avoid absorption and provide low loss propagation. One of the essential problems in the integration of guided-wave photonic devices is the proper engineering and fabrication of the coupling between active and passive components. In order to maintain high performance of the various components in an integration platform, efficient optical power transfer between these different optical functions must be realized [1.9]. For IMOS, three different integration techniques for active-passive integration are considered. In this section they will be briefly reviewed and compared.

1.4.1 Twin-guide structures

In twin-guide (TW) structures the light generation and guiding functions are separated into two vertically displaced waveguides, separated by a transparent layer (see Fig.1.5). Integration is realized by selective removal of the upper active waveguide while the lower, passive waveguide remains unaffected. This technique is not complicated and for classic InP photonics, with this technique various photonic devices like lasers[1.10], all optical demultiplexers [1.11] and wavelength converters[1.12] have already been demonstrated. Moreover, due to its simplicity, the TW structures are already in commercial use [1.13].

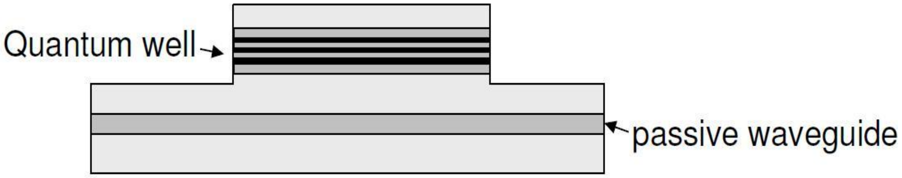

Figure 1.5: Twin guide structures for active passive integration.

However, the principle disadvantage of the TW structure is the large threshold current needed in lasers. This is because the mode power splits between the active and the passive waveguides. Furthermore, since light is coupled between the guide layers using lateral tapers, the size of such structures are relatively large due to long tapers, 200 µm for instance. Also absorption in the tapers may lead to decreased gain in lasers and SOAs. Last but not least, the small parasitic reflections from the taper tips can cause spurious mode coupling effects in lasers, leading to instabilities and can increase the relative intensity noise [1.9].

1.4.2 Polarization based Integration Scheme (POLIS)

Besides using different waveguide layers, polarization manipulation can also be used to realize active-passive integration. The "Polarization based Integration Scheme" (POLIS) makes use of a single layer structure on an InP substrate, which can guide light with one polarization, but absorbs light with the opposite polarization. This approach creates the possibility to integrate lasers and detectors together with waveguides, switches and demultiplexers within one material. Transparency for one polarization and absorption for the other polarization at the same wavelength is achieved by manipulating the strain in the quantum wells. With polarization converters it is possible to obtain the required polarization, transparent or absorbent, in each component of the optical circuit. The basic POLIS layer stack is illustrated in Fig. 1.6, with a compressively strained quantum well in the middle of the waveguiding InGaAsP layer. For TE polarization the material is absorbent, while for TM the material is transparent [1.9].

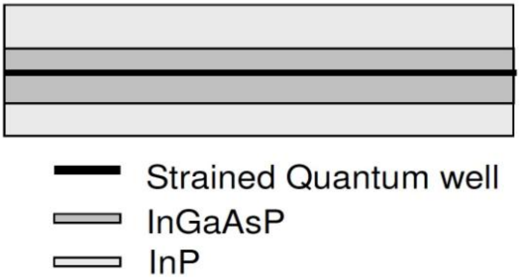

Figure 1.6: POLIS layer stack with strained quantum well.

Since POLIS uses one material system with only one waveguide layer for both active and passive components, it results in a relatively simple growth process. The technology to grow strained quantum wells and the devices based on them are already at a mature stage, so it is quite convenient to make use of the strained quantum wells. It is possible to obtain sufficiently large transition energy shifts between the two polarizations, so that low loss propagation can be achieved [1.9]. However, the use of one single layer stack implies compromise regarding the performance of the other devices. For example, QWs are good as the gain medium for lasers and amplifiers, but not so efficient as the absorbing material for the detectors. Moreover, since the required etching depth for the polarization converter and other passive components can be different. Therefore extra lithography and etching steps might be added, which may complicate the process.

1.4.3 Selective area regrowth

Selective area regrowth is an approach in which different functions are created by optimizing the material through sequential growth in different regions of the wafer. This implies selective removal of the active material using dry etching and chemical wet etching (see Chapter 3), followed by multiple regrowths of passive and other materials (see Fig. 1.7). This method is a horizontal (in-plane) integration technique, in which the active and passive materials occupy the same layer. In this respect it is similar to POLIS. However in this regrowth technique, there is much more freedom of choice for the active and passive materials and hence better optimization is possible [1.14]. In such an approach PICs designers are relatively independent to select the compositional and dimensional design parameters for active and passive regions. This can be used to obtain high coupling efficiency between the active and passive devices. All of these advantages make selective area regrowth currently the principle integration method for classic InP photonics in COBRA.

Although regrowth provides more freedom to optimize each required function, the other side of the coin for this approach is the multiple extra growth steps required on processed surfaces. This make it difficult to get a highly reproducible regrowth quality in each processing run and therefore might cause a serious yield problem.

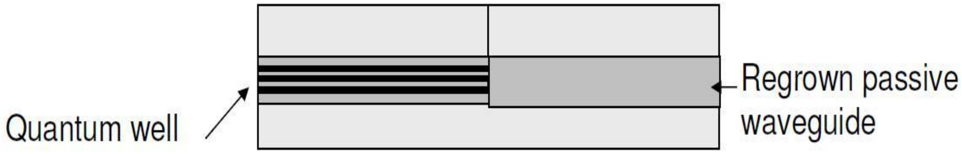

Figure 1.7: Selective area regrowth for active passive integration.

For the IMOS platform, currently all these three types of A/P integration technology are explored. In this thesis, we will focus on the selective area regrowth technique for active-passive integration in the IMOS platform.

1.5 Thesis outline

As one of the first investigations into the IMOS technology, this thesis focuses on the exploration of the key technologies for both passive and active devices, which will form basic building blocks in IMOS platform. In Chapter 2 the first generation IMOS passive components are first presented because of its relative simplicity to realize. Various types of basic PICs components with small sizes and relatively good performances are presented. Since complete PICs include both active and passive components, Chapter 3 focuses on the active-passive integration for the IMOS platform based on a selective area regrowth technique. The morphology after regrowth is checked with FIB and SEM. Furthermore, the optical properties of the regrown sample are evaluated by micro-PL. Next in Chapter 4, in order to realize direct electrical pumping for the IMOS active devices, a dielectric aperture technique is developed by the use of the AlInAs oxidation. Also here, FIB and SEM are used to evaluated the morphology. The electrical properties of the oxidized samples are analyzed with I-V measurements. Afterwards, based on these key technology developments, the first IMOS active device: an electrical pumped PhC laser is pursued. Before going to the fabrication, first in Chapter 5, the design and the simulations are first performed. In Chapter 6 and 7 the fabrication and characterization process of this electrically pumped PhC laser are explained. Finally Chapter 8 summarizes this thesis and gives an outlook to the future researches.

Chapter 2

First Generation IMOS Passive Devices

The high vertical refractive index contrast and the small thickness of IMOS membranes will allow the realization of very small and compact devices. In this chapter, the results of the first generation IMOS passive components with small size and good performance are presented. These components, including waveguides, MMI splitters and ring resonators, are basic passive building blocks for PICs.

Section 2.1 gives a brief introduction to the IMOS passive devices. Section 2.2 explains the fabrication technique for making such components. Section 2.3 is the key part of this chapter. It shows various types of fabricated and characterized IMOS passive components. Section 2.4 gives the conclusions and an outlook to the future development of the IMOS passive components.[1]

---

[1] The design is done by Dr. Fred Bordas. The author involved in the fabrication and characterization of the chips.

2.1 Introduction

As it was already mentioned in Chapter 1, the complexity of PICs has increased significantly over the last few years, following Moore's law in Photonics [2.1]. To satisfy the need for even higher complexity, devices and waveguides have to be made smaller and less power consuming. IMOS technology, with its high vertical refractive index contrast and small thickness, allows the realization of such very small and power efficient devices.

Photonic devices can be divided into two main types: passive and active. Passive devices, such as waveguides, splitters, ring resonators, etc, are mainly used for light propagation, combination and splitting, filtering etc. In active devices such as SOAs and lasers, light amplification and lasing can be achieved. Active devices require more complex design and fabrication processes. Since IMOS is a new PIC platform, it is logical to first develop passive components, which are easier to realize. Therefore the first generation of IMOS components are basic passive circuit components. Since IMOS uses a very small membrane thickness (a few hundred nms), it is difficult to directly couple light in and out of chip via the edge facets. Therefore diffractive grating couplers are made in the membrane to couple light in and out vertically. In the following sections, the results of this first generation IMOS passive components will be presented.

2.2 Process technology

In this section, the process technology for fabricating IMOS passive components will be explained first. Next, since IMOS is a new platform for photonic integration, the process development and optimization, are described. A key optimization parameter for achieving smooth sidewalls for the waveguide will also be described.

2.2.1 Fabrication technique

The fabrication of IMOS passive components starts from a layer structure containing a 200 nm InP-membrane layer on top of several sacrificial etch-stop layers (InGaAs-InP-InGaAs) on InP-substrate. On this layer stack patterns are defined by electron-beam lithography (EBL) with a positive resist (ZEP) on a 50 nm thick Si_xN_y layer, deposited by plasma enhanced chemical vapour deposition (PECVD). After the development and an optimized post-bake of the resist (see Section 2.2.2), the layer is etched with CHF_3-based reactive ion etching (RIE) to transfer the pattern from the ZEP into the Si_xN_y hard mask. Optical lithography is then used to cover the area where gratings will be made. A CH_4/H_2 based inductively coupled plasma (ICP) etching step follows, to etch the top InP layer in the open parts of the mask. After the removal of the photo resist, a second etch step of 70 nm is performed to obtain the gratings. Therefore, there is a shallow-deep transition between the grating and the waveguide region, as shown in Fig. 2.1. Afterwards the Si_xN_y hard mask is removed with a HF solution.

Table 2.1 Layer stack for IMOS passive components

Layer	Material	Thickness	Doping	Function
1	InP	200 nm	n.i.d.	Membrane
2	InGaAs	30 nm	n.i.d	Sacrificial layer
3	InP	300 nm	n.i.d.	Sacrificial layer
4	InGaAs	500 nm	n.i.d.	Sacrificial layer
5	InP	300 µm	n=1e18cm-3	Substrate

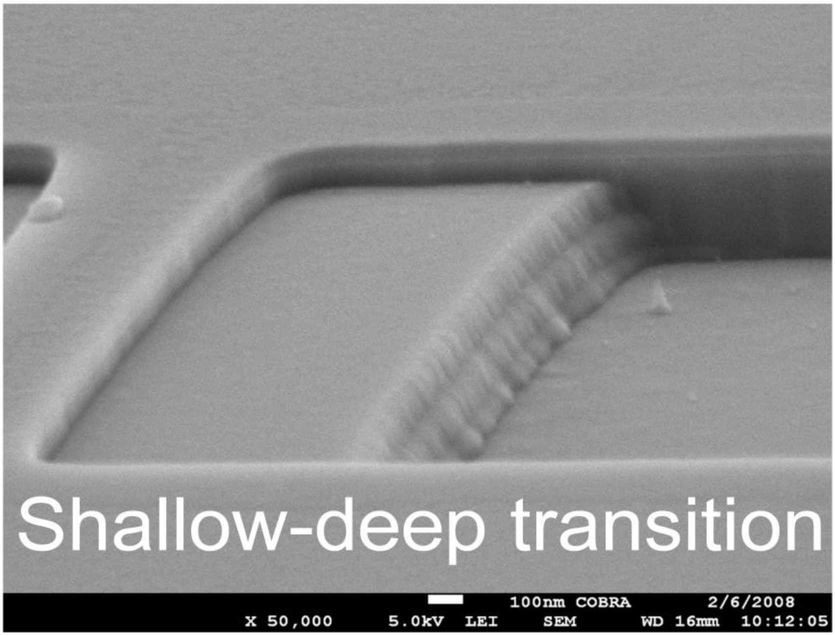

Figure 2.1: Etching test for a shallow-deep transition between grating and waveguide region. The deeply etched part is for the waveguide and the shallow etched regions are for the grating coupler. Fig. 2.5 shows a realized grating coupler based on this shallow-deep transition.

As shown in Fig. 2.2, after pattern definition, a layer of BCB is spin-coated onto the InP-sample. Then the sample is bonded up-side down onto a host-substrate (Si) with a spun BCB-layer. The combined BCB-layer is then cured for 1 hour at 250 ℃ in a nitrogen environment. The InP-substrate is removed using wet-etching in the standard InP etchant ($4H_3PO_4 : 1HCl$) until the first InGaAs etch stop layer are used. Finally the sacrificial layers (InGaAs-InP-InGaAs) are removed by successive selective wet etching steps[2.2].

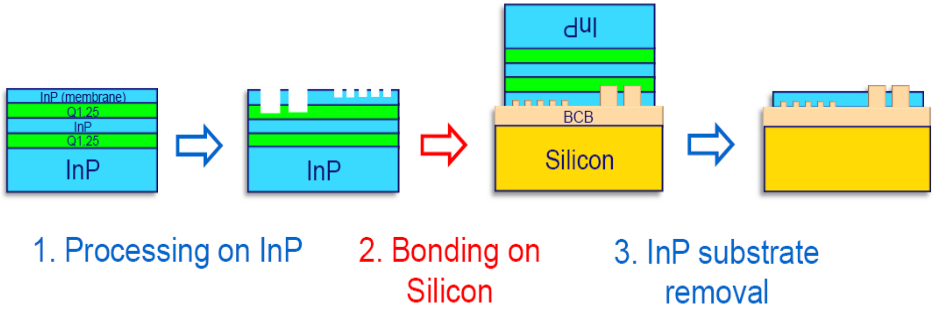

Figure 2.2: Basic fabrication scheme of IMOS passive devices.

2.2.2 Process optimization-Post development baking

As mentioned in the last section, after development of the resist (ZEP), a post development baking step is used to reduce the sidewall roughness. This is critical for low propagation losses in the photonic waveguides since sidewall roughness is one of the main sources for the waveguide loss. Therefore, the post development baking temperature is a critical parameter, which needs to be optimized. Post development baking of ZEP is done at temperatures close to the melting point. The surface tension will then smoothen the side walls. However, if the temperature is too high during the post baking step, the resist will flow so much that the control of the pattern width and shape are lost. Fig 2.3 shows a comparison of SEM images of ZEP-patterns after post development baking at various temperatures for 2 minutes. One can see that if the temperature is not high enough, for instance T=145 ^{o}C, the roughness of the side wall still remains. However if the post development baking temperature is too high, for example T=155 ^{o}C, the resist tends to lose its shape. Therefore an optimized temperature (T=150 ^{o}C for 2 minutes) is chosen which reduces the side wall roughness sufficiently, but maintains the resist patterns.

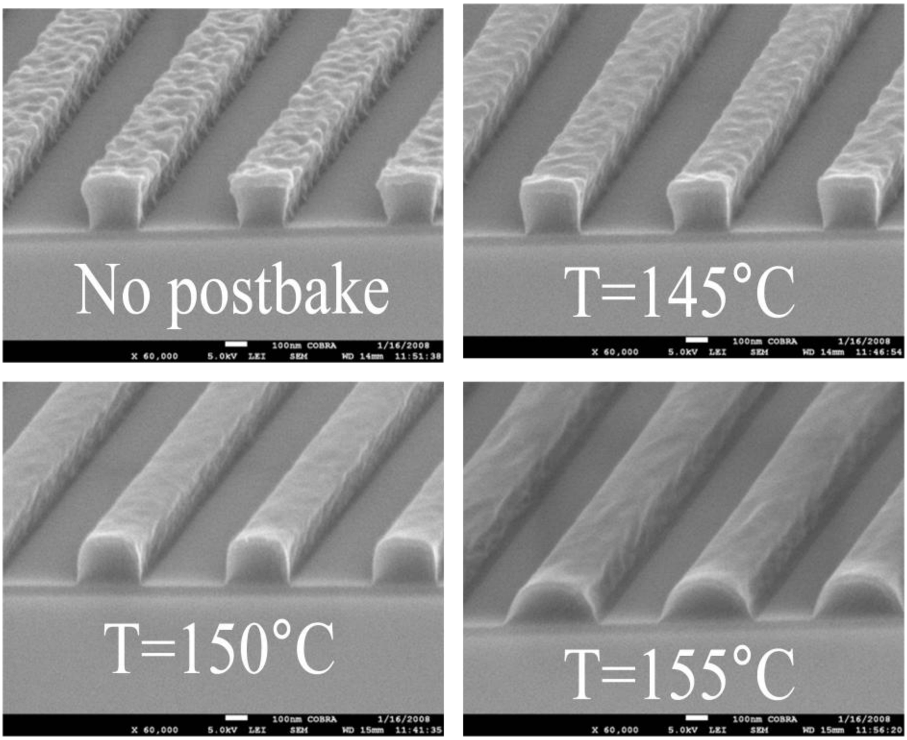

Figure 2.3: ZEP-patterns after different post-baking temperatures.

2.3 Fabricated passive components

In this section, a number of realized IMOS passive components will be presented and characterized. The characterization setup is shown in Fig. 2.4. Transmission spectrum measurements are performed with a tuneable laser as a source. Fibers and grating couplers are used to guide the light in and out of the measured chip. The output light is collected by a photo detector. In the following section, first the grating couplers which are used to couple light in and out will be introduced. Next, various types of passive components will be described.

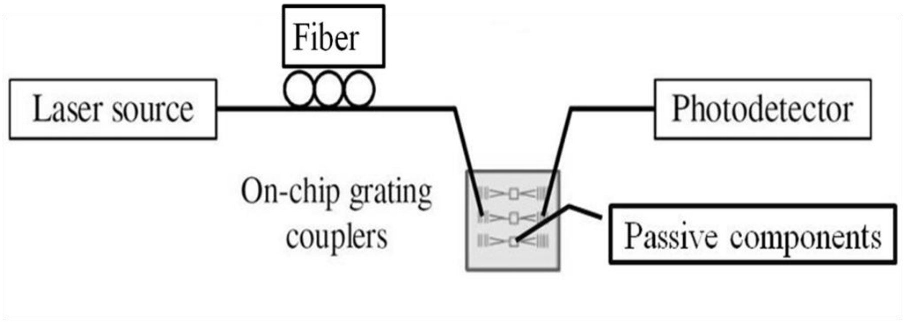

Figure 2.4:Schematic view of the characterization set-up used for the passive devices [2.3].

2.3.1 Grating coupler

As mentioned previously, IMOS uses a very small membrane thickness (a few hundred nm), which means that the propagating mode has a very small size (around 0.5 µm^2). However, the standard single mode fibre has a mode diameter of 10 µm^2. This makes it very difficult to couple light directly in and out of the chip from the edge: without mode adapters more than 20 dB will be lost.

Therefore in order to solve the problem of high optical loss of the edge coupling technique, diffractive grating couplers are made in the membrane to couple light in and out vertically, as shown in Fig. 2.5. The first demonstrations of coupling light into thin film waveguides using gratings date back to the 1970-ties [2.4-2.5]. Since then, a lot of research has been performed on this topic. An instructive analysis of grating couplers and simple design rules is given by Tamir [2.6].

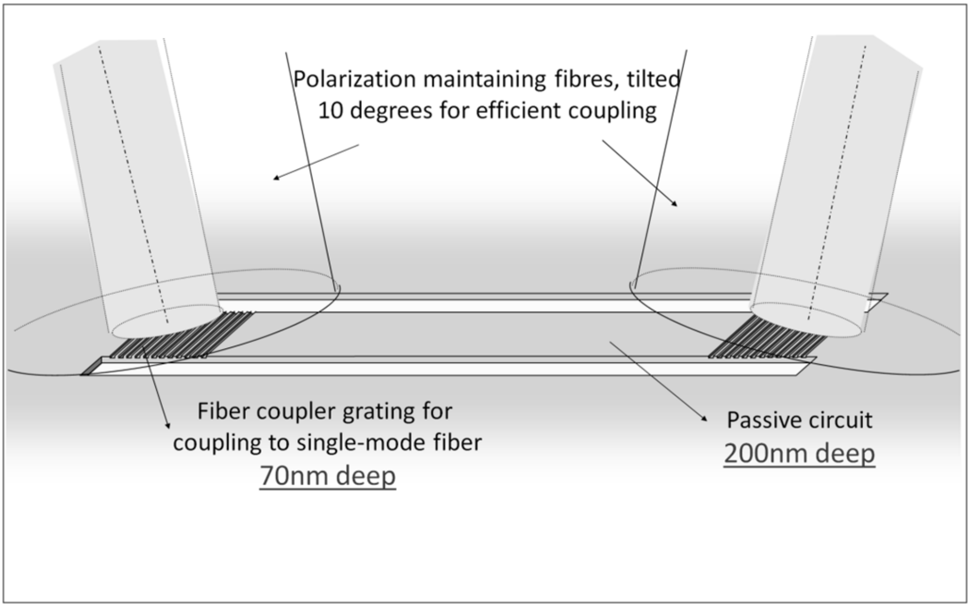

Figure 2.5: A schematic view of the fibre grating coupler[2.7].

a) Grating design

The gratings are designed for optimal coupling from an optical fibre to a membrane waveguide and vice versa at a wavelength of 1550 µm, with the fibre tilted 10^{o} from the normal in order to couple selectively in a single direction. The designed etching depth of the gratings is 70 nm, to allow for an efficient overlap of the diffracted field with an optical fibre mode. The grating period is 730 nm, with a filling factor of around 50%. The optimal simulated BCB thickness is 780 nm + $0.994p\lambda/2n$, where λ is the wavelength in vacuum (1550 nm), p is an integer and n is the refractive index of the BCB layer (1.55). The numerical factor in the second term is a geometrical correction due to refraction of the light. In our case p=1. This particular thickness allows for maximum fibre-chip coupling with its original design in [2.8]. Figure 2.6 shows a fabricated grating coupler, one can see the shallow-deep transition clearly. Grating couplers for input and output, each covering an area of $10x10\mu m^2$, are designed and fabricated.

The gratings are connected to a 50 µm long 400 nm wide waveguide by 600 µm long tapers on each side.

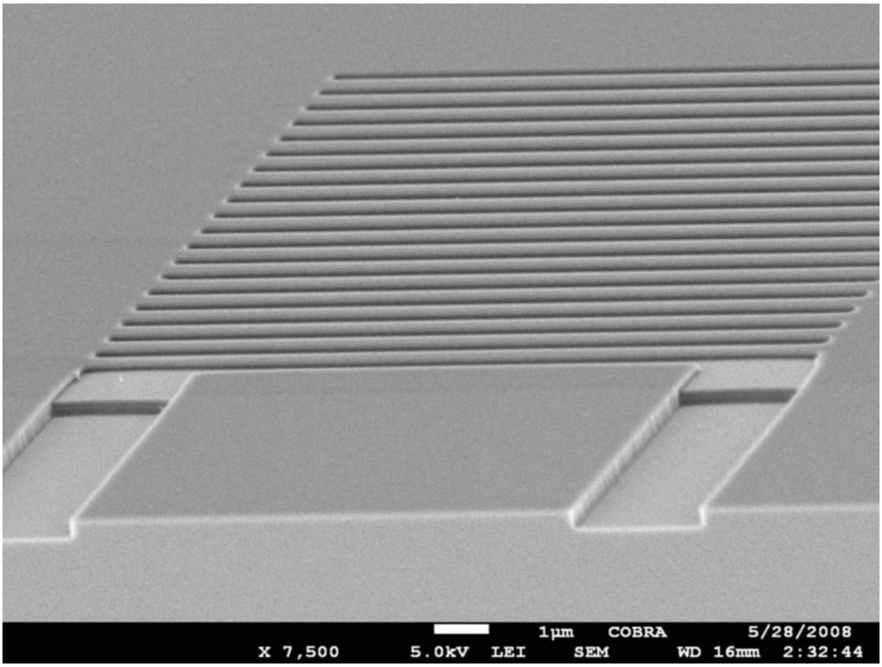

Figure 2.6: SEM picture of one fabricated grating coupler. In the lower side the beginning of a waveguide taper is visible.

b) Measurement

The transmission spectrum measurement through this structure is shown in Fig.2.7. The measured fiber-to-fiber loss at the peak wavelength is 6.8 dB. As the waveguide is very short, it is assumed that losses primarily arise from the two grating couplers. This assumption will be confirmed in the next section. One can see that for this grating coupler, the maximum coupling efficiency is around 47%. Moreover the spectrum has a broad bandwidth with a FWHM of more than 70 nm. The peak wavelength is around 1520 nm which is shifted from the designed value (1550 nm). This is mainly due to over etching of the gratings, which can be corrected and optimized in the next runs.

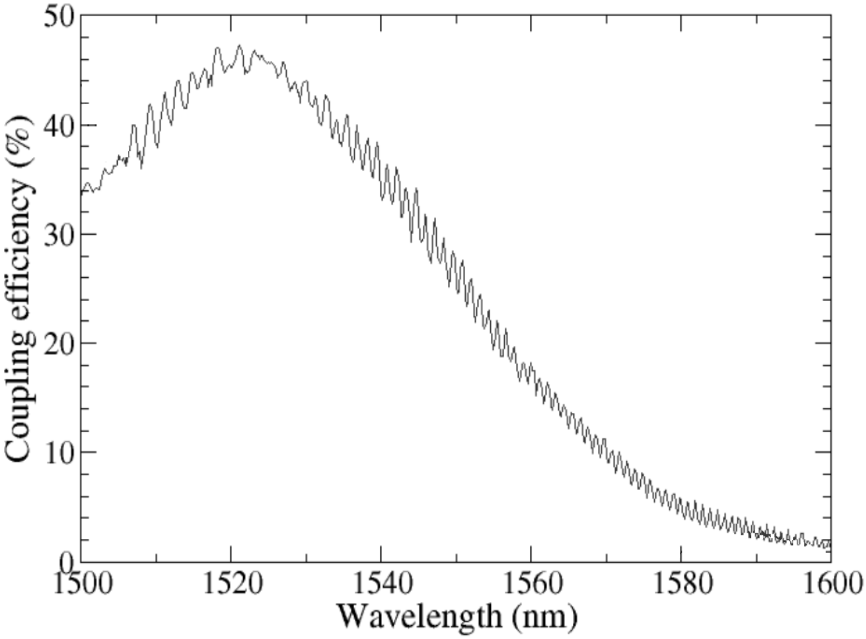

Figure 2.7: Transmission spectrum for one grating coupler.

2.3.2 Waveguide

Waveguides are the most basic elements of PICs. They determine the path of the light signals propagating from one component to another. Thanks to the high refractive index contrast of the IMOS platform, very narrow photonic waveguides (400 nm) can be realized (See Fig 2.7).

Four different waveguide lengths are included in the design in order to determine the propagation losses. Fig.2.8 shows the transmission spectra for 500 µm, 300 µm, 100 µm and 50 µm long waveguides. No apparent differences in transmission spectrum can be seen for the different lengths.

Since the difference between the spectra for the longest and the shortest waveguides is less than 0.5 dB, an upper boundary of 10 dB/cm for the propagation losses can be deduced. This confirms the assumption made in the preceding section that the propagation loss of a 50 μm long waveguide can be neglected. Moreover this low propagation loss is also confirmed by the results for the ring resonator in Section 2.3.4. Compared with SOI and InP waveguides, the propagation loss value is still a bit higher. However, we believe that by further optimization and applying improved technology (See Section 2.4), the propagation loss can be further reduced.

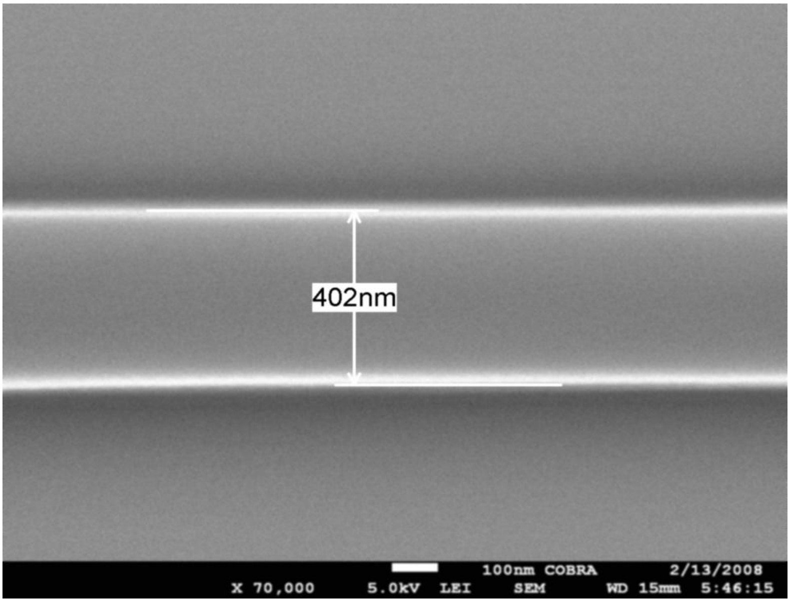

Figure 2.7: 400 nm wide photonic waveguide on IMOS

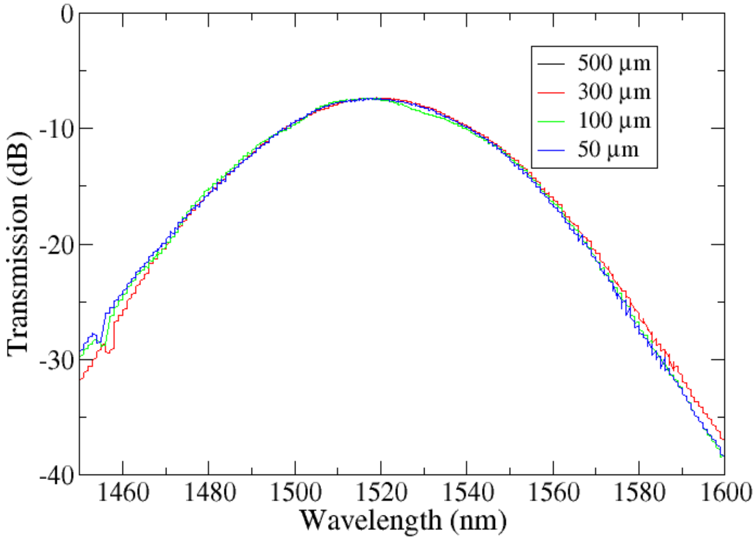

Figure 2.8: Transmission spectrum through 400 nm wide waveguides of different lengths, including two grating couplers.

2.3.3 Bends

Waveguides cannot always go straight. To make more complex PICs, curved waveguides with low loss are essential. Due to strong optical confinement brought by the high refractive index contrast of the IMOS platform, small bending radii with low loss are possible. Three different S-bends are designed, fabricated and measured, with a radius of 40 µm, 20 µm and 5 µm. Fig. 2.9 shows a SEM picture of an S-bend with a radius of 20 µm.

The transmission spectra are shown in Fig 2.10. Assuming that the coupling efficiency of the gratings is the same for all devices, no obvious difference between the bends with different radius can be measured. This result is comparable with the result of bends in the SOI platform since both platforms have very high refractive index contrast [2.9]. Compared with the classical InP platform, which uses low index contrast between InGaAsP and InP, these small bending radii and loss are a big improvement [2.10]. In conclusion sharp bends with low bending loss in IMOS platform suggest that very compact integrated optical circuits can be fabricated using bends with radii as small as 5 μm.

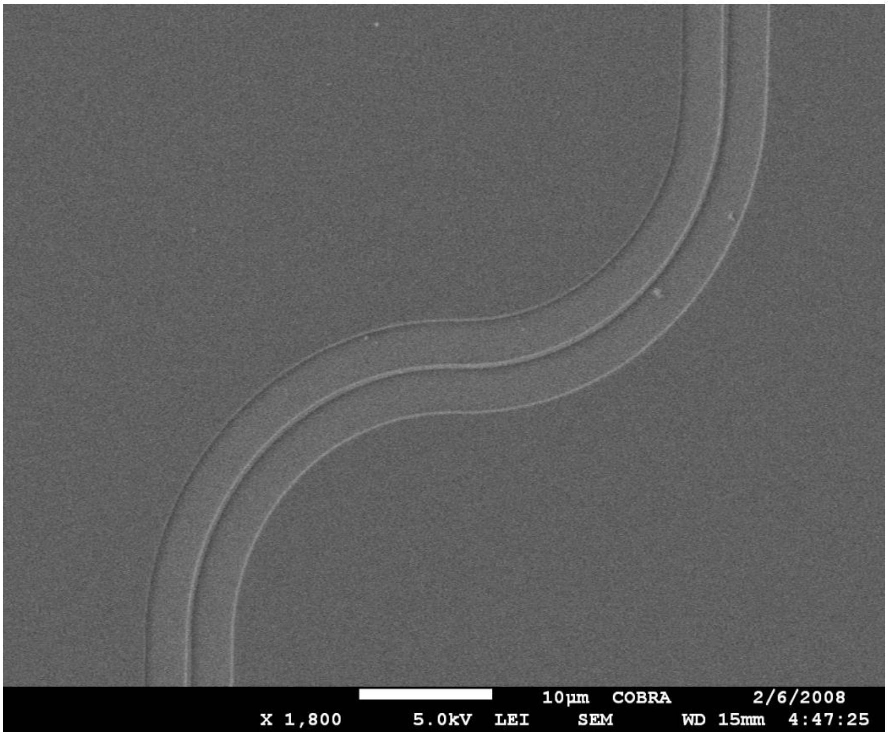

Figure 2.9: SEM picture of an S-bend with a radius of 20 μm.

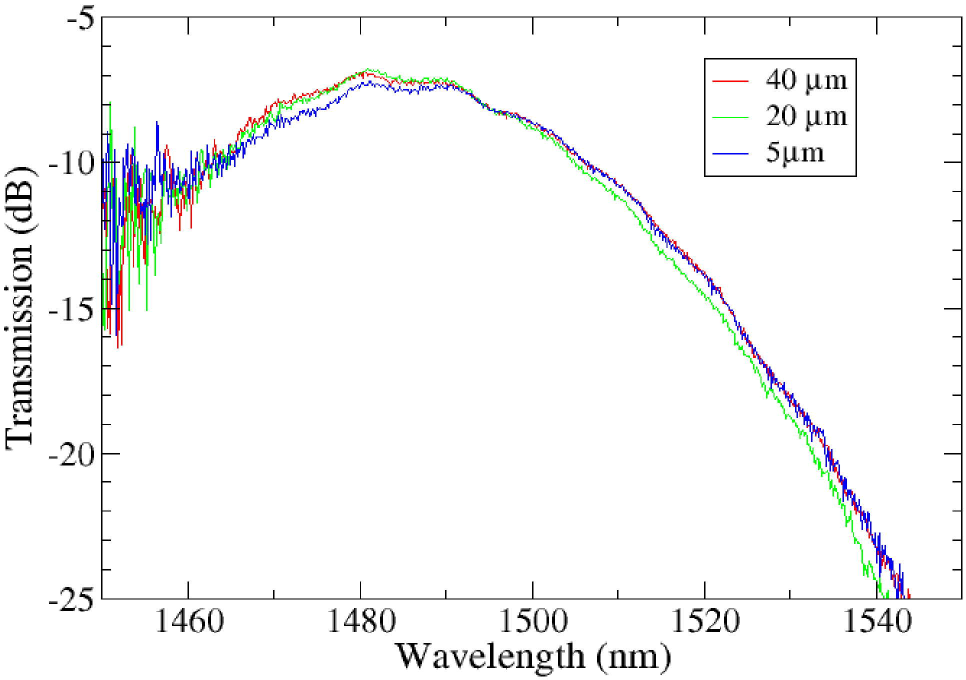

Figure 2.10: Transmission through S-bends of 40 μm, 20 μm, and 5 μm, including two gratings.

2.3.4 Ring resonator

Among the first generation of IMOS passive components, two sets of ring resonator filters are realized. Fig. 2.11 shows a SEM picture of such a ring resonator. It has a radius of 4 μm and a coupling gap of 150 nm. Light is coupled to the ring from a straight waveguide through a directional coupler. The measured transmission spectrum of this ring resonator is shown in Fig. 2.12, revealing a free spectral range (FSR) of 28.2 nm. The resonance occurs at λ =1603.5 nm and has an extinction ratio of 16 dB. The loaded Q-factor, defined as f_0/FWHM with f_0 the central frequency and FWHM the full width half maximum, is 5830.

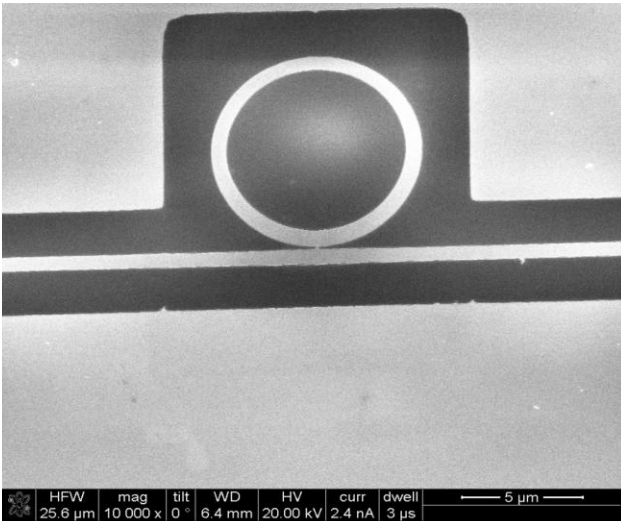

Figure 2.11: SEM photograph of a ring resonator with 4 μm radius.

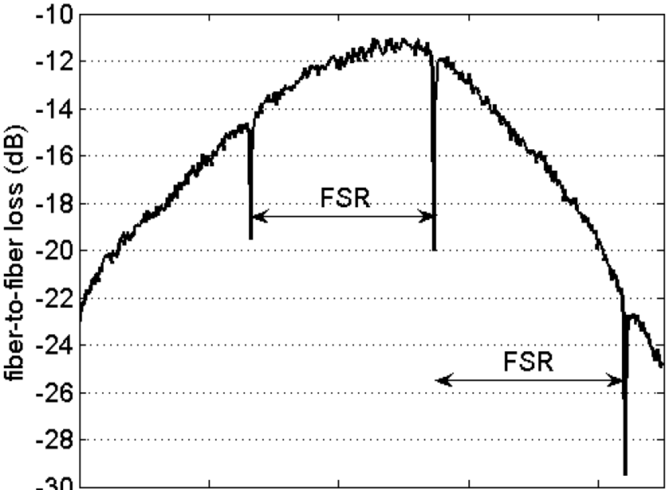

Figure 2.12: Transmission spectrum of the ring resonator with 4 μm radius, including two grating couplers.

In a second run a loaded Q-factor of 15500 has been measured for ring resonator with radius of 7 µm as shown in Fig. 2.13. One resonance peak of the transmission spectrum is shown in Fig 2.14. A fit to the experimental peak shows that the resonant peak wavelength is centred around λ=1530nm. The propagation loss in the ring is found to be 7 dB/cm, which agrees with the upper limit measured for the straight waveguides (see Section 2.3.2). The coupling constant in the directional coupler is low, $3x10^{-3}$, because the coupling region (300nm) is relatively wide compared to the previous ring resonator. This explains the relatively shallow dip of the resonance peak. We believe that by further optimization of the coupling region and the EBL parameters, the size can be even smaller and the performance better.

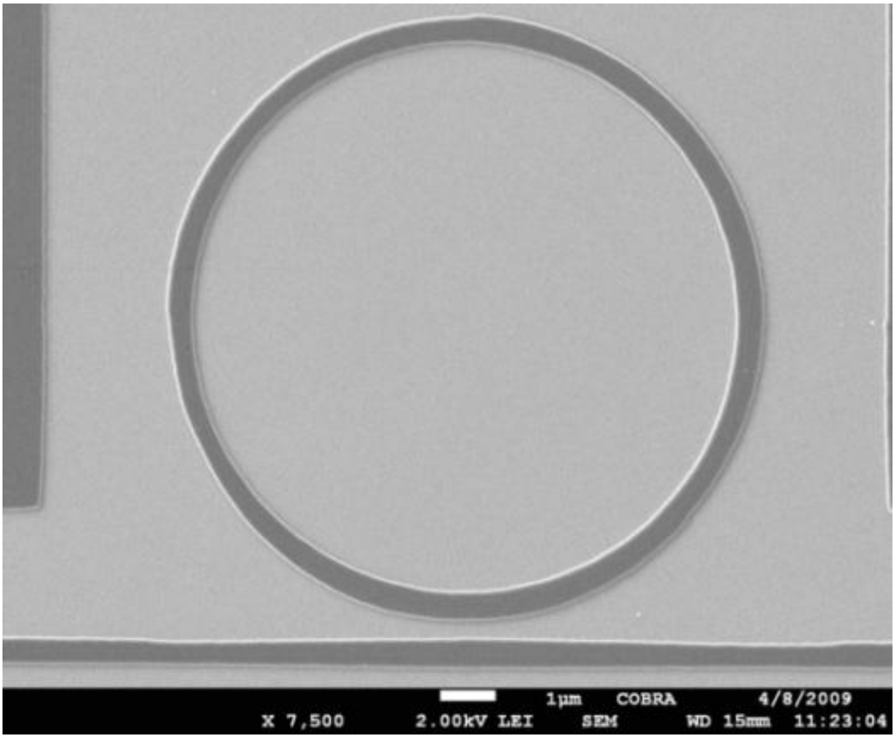

Figure 2.13: SEM photograph of the ring resonator with 7 µm radius.

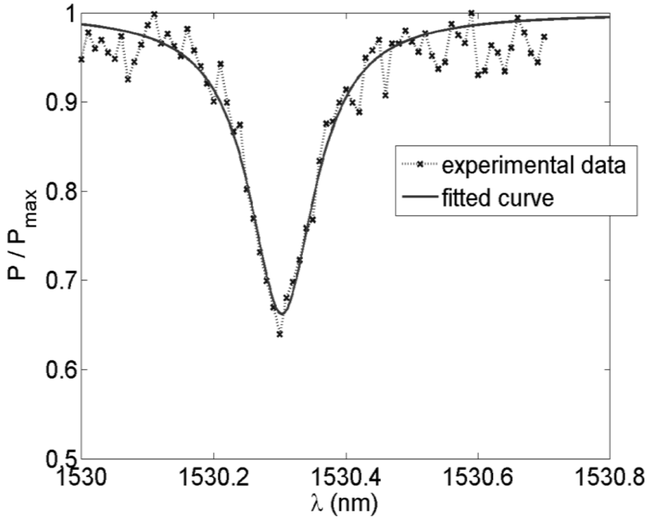

Figure 2.14: Transmission spectrum at a resonance peak of the second generation ring resonator.

2.3.5 Multimode interference

Multimode interference (MMI) couplers are extensively used in PICs for light splitting, combining and as on-chip reflectors [2.14]. The operation of an MMI device is based on the so-called self-imaging principle. Self-imaging is a property of multimode waveguides by which an input field profile is reproduced in single or multiple images at periodic intervals along the propagation direction of the waveguide. MMIs have many advantages, such as a large optical bandwidth, polarization independence, a simple structure, large fabrication tolerance, and small footprint. These advantages make them suitable for realizing various optical devices, such as multiport beam splitters, couplers, and switches [2.15]. This makes it an important basic passive component for PICs.

The 1×2 MMI splitters are the simplest MMI couplers and can be used as optical splitters and combiners in planar PICs. They have a two-dimensional (2D) planar structure, consisting of one input port, an MMI section, and two symmetric output ports. As shown in Fig. 2.15, the first fabricated IMOS MMI has dimensions of only 6.64 x 2.75 x 0.2 μm^3. Transmission measurements on the device are shown in Fig 2.16. The reference (upper line) is a 50 μm long waveguide without MMI. Transmission through the two output branches is very comparable and 3.6 dB lower than the reference. Hence the fabricated MMI coupler operates as a 3dB splitter with a small insertion loss of 0.6 dB [2.16].

Compared with 1x2 MMIs in bulk InP, the size is much smaller and the insertion loss is comparable or even lower. The size and the insertion loss of this 1x2 MMI are comparable with equivalent devices on an SOI platform.

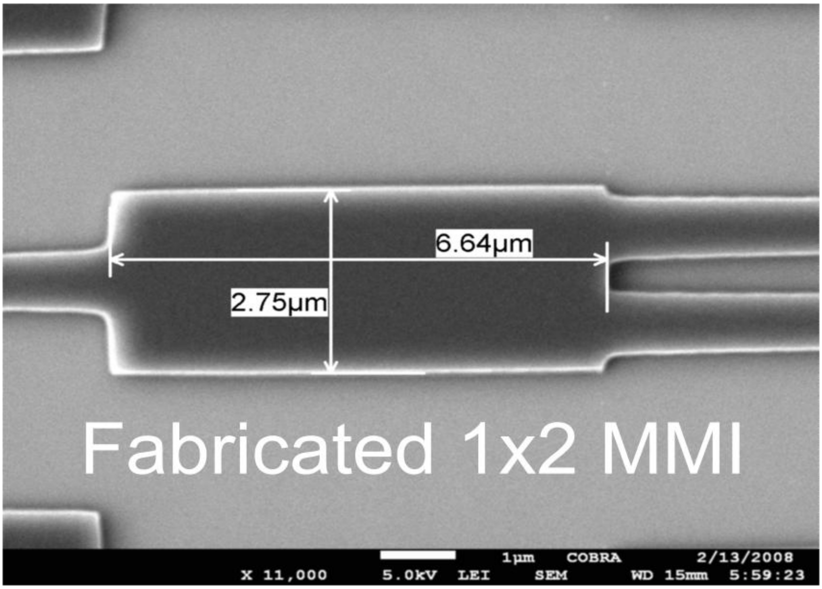

Figure 2.15: SEM image of a fabricated MMI-coupler.

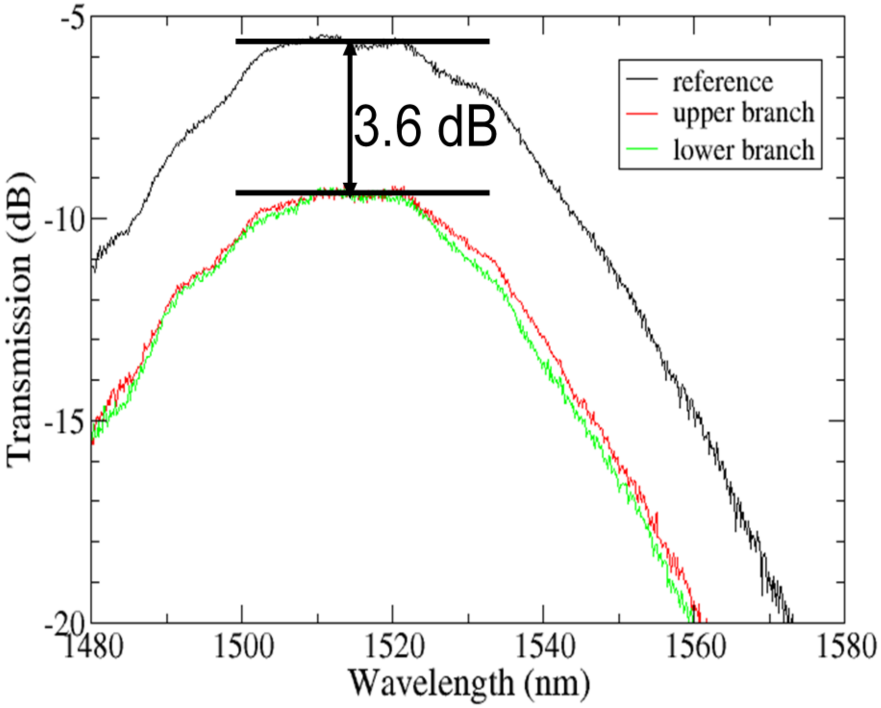

Figure 2.16: Transmission through both output branches and a straight reference waveguide (including grating couplers).

2.4 Conclusion and outlook

In this chapter, results of the first generation of IMOS passive devices are presented. Grating couplers, which are used to couple light in and out of the membrane circuit, give a coupling efficiency as high as 47%. The measured propagation losses of the waveguides are below 10dB/cm. Waveguides with sharp bends show very low bending loss. Furthermore, realized ring resonators show loaded Q-factor values of more than 15,500 together with propagation losses of 7 dB/cm. Last but not the least, ultra small 3-dB MMI splitters are demonstrated, showing an excess loss of only 0.6 dB.

In conclusion, the achievements so far shows that IMOS is a promising platform for photonic integration. Since photonic integrated circuits consist of both passive and active components, in the following chapters, the technology development for a successful active-passive integration towards complete PICs will be presented.

Chapter 3

Active-passive integration by selective area regrowth for IMOS

In this chapter, we present our results on active-passive integration by selective area regrowth[2] *for the IMOS platform. Section 3.1 gives the motivation for this research. In Section 3.2, the design of the active-passive integration is explained. Section 3.3 focuses on the exploration and optimization of the process technology. Sections 3.4 and 3.5 report the characterization of the active-passive butt-joint. In particular, Section 3.4 evaluates the morphology, while 3.5 focuses on the analysis of the optical properties of the submicron active structures. Finally the chapter finishes with conclusions and discussions.*

---

[2] The regrowth is done at Cedova and the author thanks Peter Thijs for his help.

3.1 Introduction

In Chapter 2, it was shown that ultra small passive components, such as waveguides, ring cavities and MMIs, can be made in an InP membrane, with relatively good performance [3.1]. This is because of the high vertical index contrast and the small thickness of the InP-based membrane. However, since photonic integrated circuits consist of both passive and active components, successful active-passive integration is an essential step towards complete PICs. Especially, active-passive integration within submicrometer range will enable the realization of very small lasers in InP-based membranes. This will lead to very low threshold currents and low electrical power consumption. Naturally, this is of great interest for applications like single photon sources and digital photonics, such as all-optical flip-flops based on coupled lasers. Figure 3.1 shows a schematic view of the IMOS PICs based on active passive integration.

In this chapter, the results of submicron active-passive integration for IMOS will be presented. The interfaces between the active and passive areas will be qualified in terms of morphology. Moreover, by using micro photoluminescence (μPL) tools, the photon emission from the sub-micrometer size active areas, containing the InGaAsP quantum wells (QWs), is evaluated to determine the influence of the processing to the QWs.

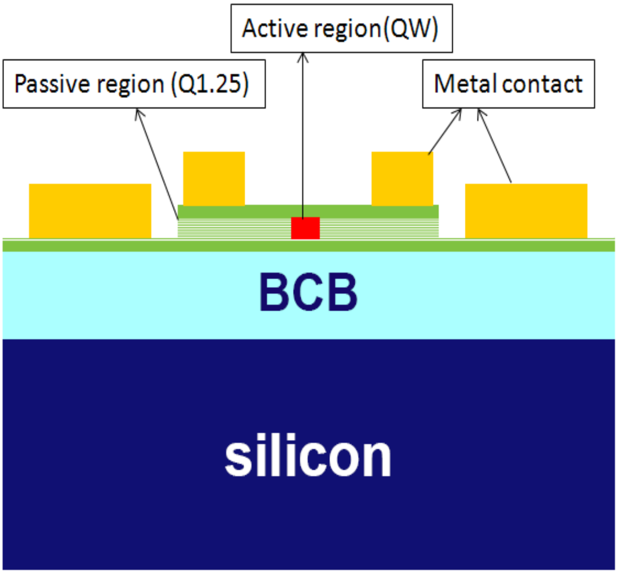

Figure 3.1: Schematic view of the IMOS platform based on active passive integration

3.2 Idea and design

In this thesis, active-passive integration is obtained by using a selective regrowth technique. First an active layer stack is grown, masked and etched to define the active areas. Then the passive layer stack is regrown in the etched areas [3.2].

For a high quality of the active-passive integration, two critical conditions should be satisfied. First, a smooth and flat interface should be realized between the active and passive materials. A rough interface causes scattering loss when light is coupled between the active region and the adjacent passive regions. Especially, voids should be avoided, because they strongly increase the losses and reflections. A good surface flatness is also necessary for processing and bonding of the membranes. Second, since the smallest active regions are of submicron size, the damage to the active quantum well materials due to the processing needs to be minimized, since otherwise the emission is reduced or even stopped. In the design, active regions of different orientations, shapes (hexagons and octagons for instance) and sizes (varying from 250nm to 2.5um) are designed. This is because the regrowth processes used can depend on the shape, size or orientation of the active structures. Furthermore, such variations provide information on the possibilities to make lasers with active regions of different shapes, sizes and orientations.

Table 3.1 Various shapes of structure for active-passive integration.

Shapes	Figure	Size [µm]	Rotation [degree]
Hexagon	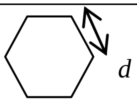	$d \in [0.25,0.5,$ $1.25,1.75,2.25]$	$\Theta = 30^o$
Octagon	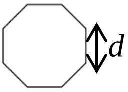	$d \in [0.25,0.5,$ $1.25,1.75,2.25]$	$\Theta = 22.5^o$
Disc	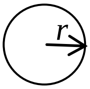	$r \in [0.25,0.75,$ $1.25,1.75,2.25]$	-
Rectangular	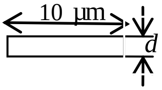	$d \in [0.25,0.75,$ $1.25,1.75,2.25]$	$\Theta \in [30^o, 45^o, 60^o, 90^o]$
Square	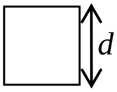	$d \in [0.5,1,$ $1.5, 2, 2.5]$	$\Theta \in [30^o, 45^o, 60^o]$

3.3 Process technology

In this section the process technology is presented. Especially the optimization of the wet etching of the active region, which is a crucial step towards successful active-passive integration, is explained.

3.3.1 Process description

The starting point of the processing is a 200nm InGaAsP layer (Q 1.25) on n-type InP substrate as shown in Fig. 3.2 (a). Multiple quantum wells (QWs) with a composition of InGaAsP and individual thickness of 6 nm are embedded in this Q1.25 layer. These QWs are designed to emit light at 1.55 µm. First of all, the cap layer is removed and a 50nm Si_xN_y is deposited on top by PECVD. Secondly, after the EBL resist (ZEP, positive resist) spinning, the small active regions are defined by EBL. After the resist development and microscope check, 30 nm chromium (Cr) is deposited on top of positive resist and the sample is immersed in acetone for a whole night to perform the lift off process. Then the pattern is transferred to the hard mask by a dry etch of Si_xN_y using reactive ion etching (RIE). After removing the Cr using an O_2 plasma, the quaternary layer is first dry etched using RIE with CH_4:H_2 at an etch rate of 30 nm/min, except for the places where a submicron active medium is required (See Fig. 3.2 (b)).

Next, a citric acid ($C_6H_8O_7$) based chemical wet etch is used to form the required overhang of the Si_xN_y (See Fig. 3.2 (c)). This etching is isotropic and has an etch rate of 7 nm/min. The wet etching time to form this overhang needs to be optimized so that the subsequent regrowth will result in a flat surface around the interface between active and passive regions. This optimization of the wet etching time will be explained more in detail in Section 3.3.2. Fig. 3.3 shows one of the active regions after wet etching, but before regrowth. On top is the 50nm Si_xN_y mask. One can see the overhang and quantum wells clearly. Afterwards regrowth of passive material (Q1.25) leads to a quaternary layer around the local active medium (QWs) (See Fig. 3.2 (d)).

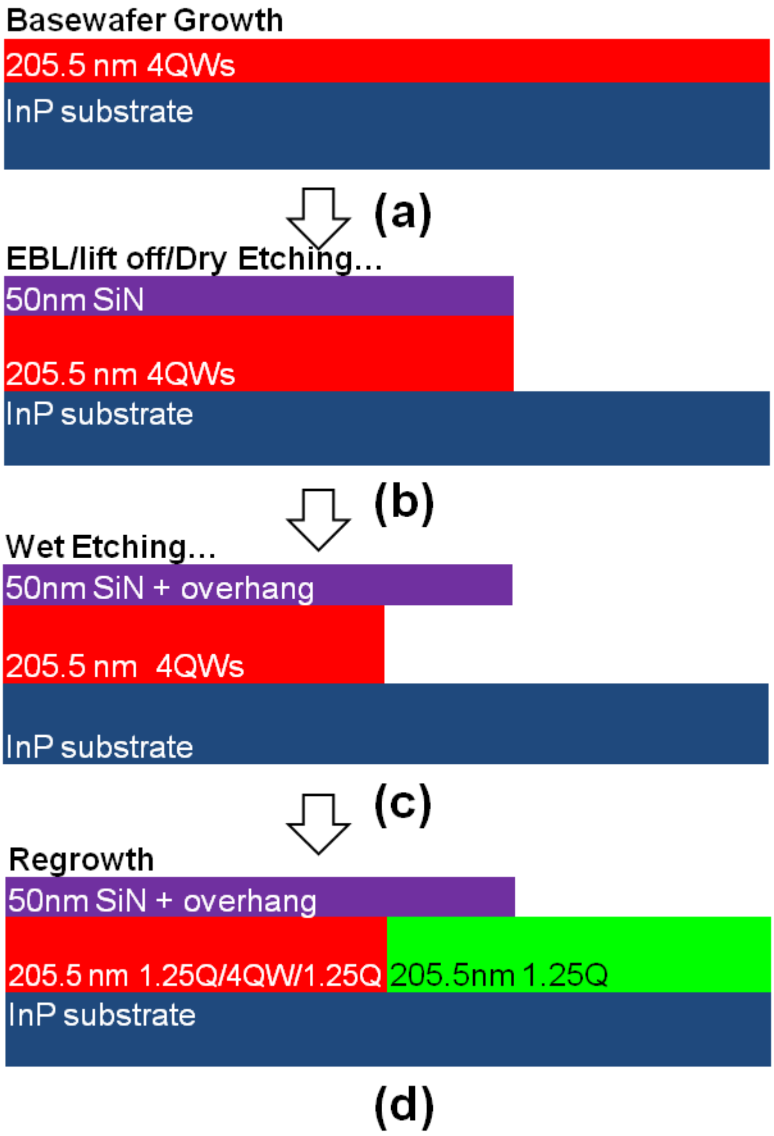

Figure 3.2: Fabrication process flow [3.3].

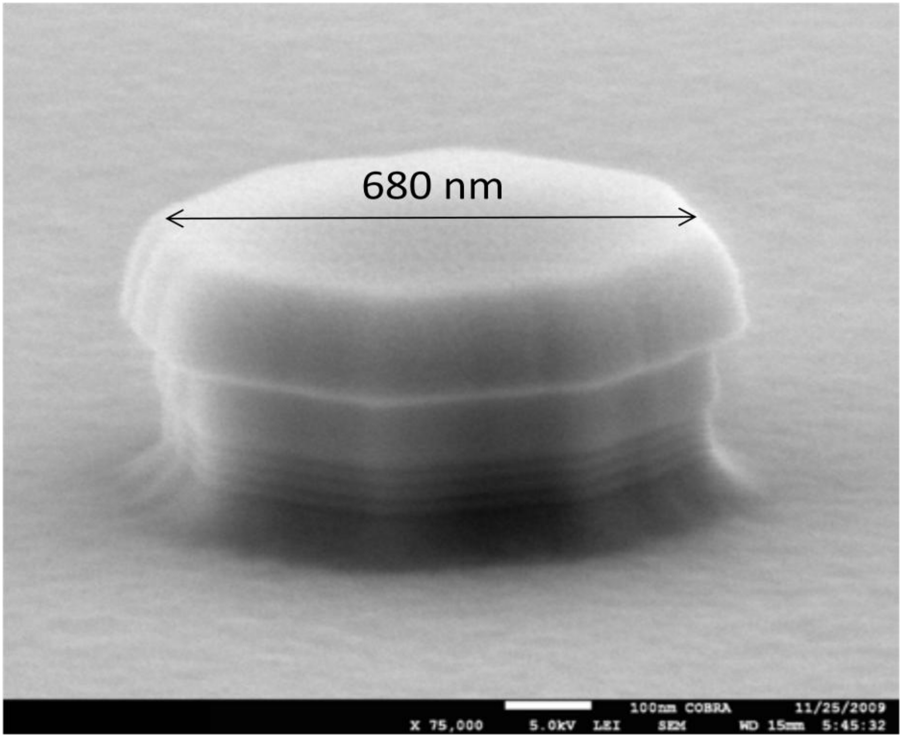

Figure 3.3: A submicron structure etched but before regrowth (Octagon)

3.3.2 Overhang wet etch optimization

Wet etching of the overhang is an essential step to obtain a good active-passive integration. During the regrowth step (Fig 3.2.d), the reactants which precipitate on top of the Si_xN_y mask will diffuse to the side and locally increase the growth rate there. Therefore the thickness around the active-passive interface can increase. In order to achieve a flat surface there, an overhang is created. The size of the overhang, which is controlled by the citric wet etching time, should be optimized in order to exactly store the extra diffused material. Fig. 3.4 shows an active structure which is wet etched too long (10 mins). The Si_xN_y mask is still left on top of the active region in order to make the structure visible. One can see that the overhang is so large that there are gaps around the active passive interface.

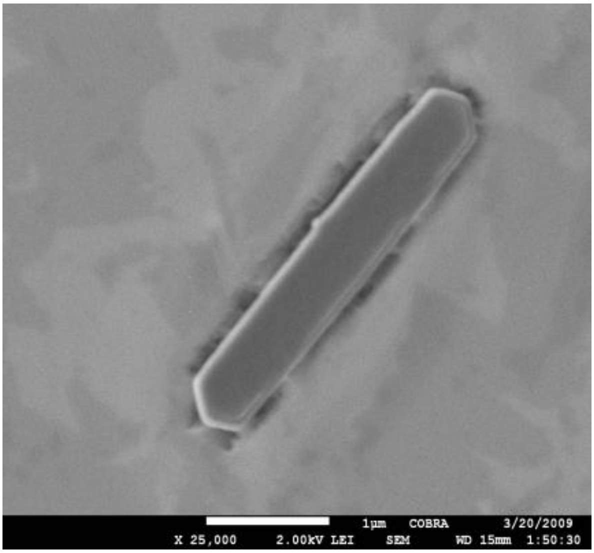

Figure 3.4: One active structure after regrowth (10mins wet etching)

On the other hand, if the wet etching time is too short, the active passive interface is not flat, as can be seen in Fig. 3.5. This structure is wet etched in Citric based solution for 5 minutes. A careful inspection shows a small bump around the active passive interface. Thus, the chemical wet etching time should be in between these two cases in order to get a proper overhang for a flat active passive interface. After several tests, the optimum time for a 200nm membrane InGaAsP layer is found to be 7mins as shown in Fig. 3. 6.

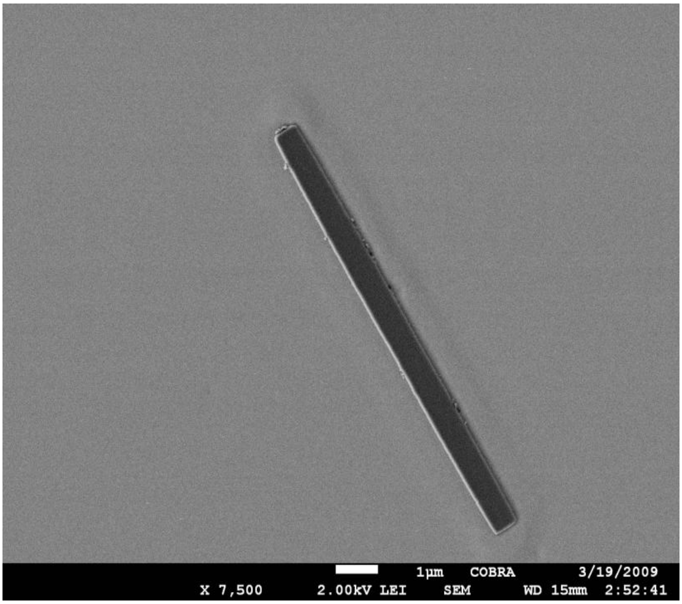

Figure 3.5: One active structure after regrowth (wet etched for 5mins)

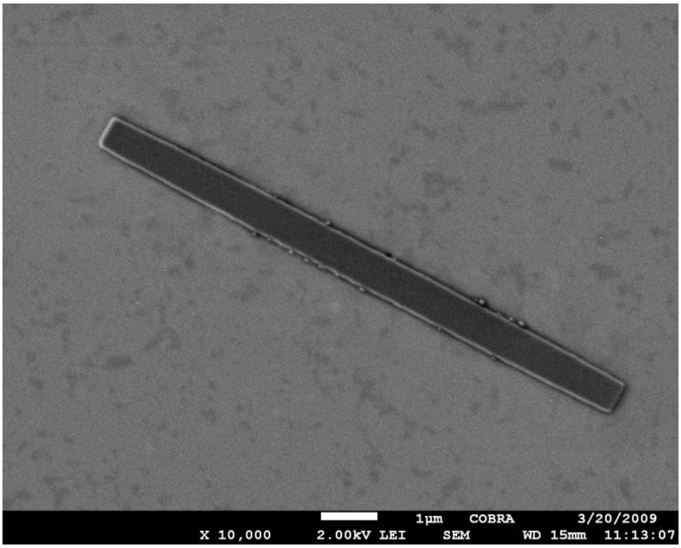

Figure 3.6: One active structure after regrowth (wet etched for 7mins).

3.4 Characterization

The characterization of the active-passive integration focuses on two aspects. First the quality of the interface between active and passive materials is checked using focused ion beam (FIB)[3] etching and SEM inspection. Second micro photoluminescence (μPL) tools are used to evaluate and analyze the emission properties of the remaining area with active submicron quantum well material.

3.4.1 Morphology

In order to evaluate the quality of active passive integration, a cross section view of the active-passive interface is needed. However since the active region sizes are in the submicron range, it is impossible to cut through the ultra small active region by normal cleaving. Therefore FIB etching is used to locally open the submicron active structure and a SEM is used to get a cross section view of the active-passive interface. FIB is a commonly used technique in the semiconductor industry. It can be used for local manipulations (such as etching, deposition and sputtering) of semiconductor materials. FIB systems operate in a similar fashion as a scanning electron microscope (SEM) but rather than a beam of electrons, FIB systems use a focused beam of ions (usually gallium) that can be operated at low beam currents for imaging or high beam currents for site specific sputtering or milling [3.4].

During the FIB etching, a small amount of Pt is first deposited on top of the submicron active structure. Next, the gallium (Ga+) primary ion beam hits the sample surface and sputters away a small amount of material so that a cross section view of the target structure is formed. In Fig. 3.7 and Fig. 3.8 one can see two examples of realized structures with a submicron size. The SiNx mask used for the regrowth is left on the sample, in order to make the

---

[3] The FIB is done together with Dr. Beatriz Barcones Campo and the author thanks her for the help.

active areas visible in the SEM. The line indicates the position where the cross section pictures are made, using FIB etching and SEM. The good quality of the interface and the flatness of the surface can be seen in these cross section pictures.

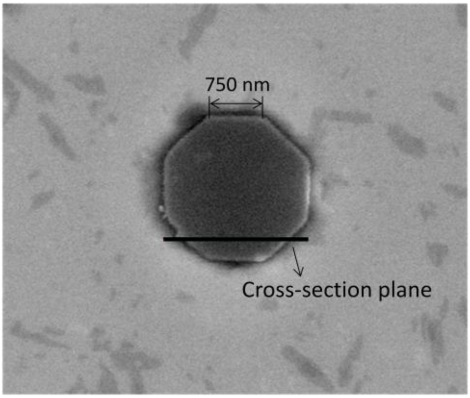

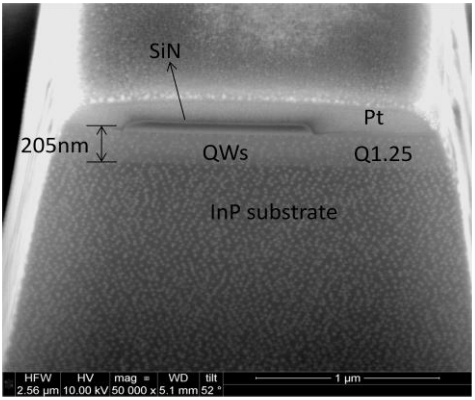

Figure 3.7(a): A submicron structure (Octagon) Figure 3.7(b): Cross section view by FIB

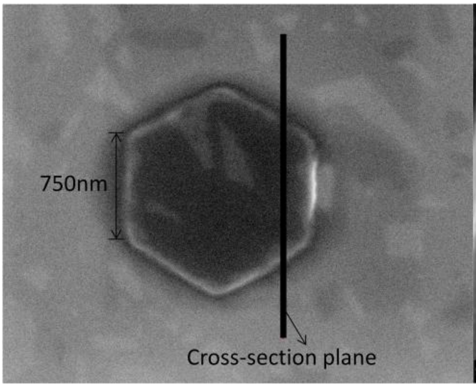

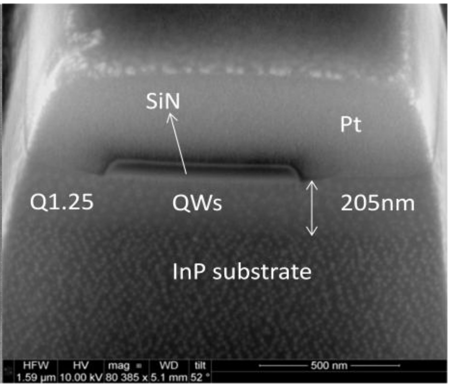

Figure 3.8(a): A submicron structure (Hexagon) Figure 3.8(b): Cross section view by FIB

3.4.2 Micro photoluminescence analysis

Micro photoluminescence (µPL)[4] is used to evaluate the emission of the quantum wells (QWs) in the submicron active region. The motivation is to determine whether the QWs are damaged by the processing.

a) Micro PL setup

For the experimental characterization of the fabricated structures, a room temperature µPL* set-up is used. Figure 3.9 shows the schematic representation of the set-up. The sample is placed on an x-y-z stage where its position is set with a piezoelectric controller. An objective is used for excitation and collection of the luminescence to characterize the structures. A continuous wave laser (λ = 660 nm) is used to excite the realized structures. The exciting beam has a spot size of around 6 µm. The excitation of the QWs and the collection of the PL signal are done with a high numerical aperture (NA) microscope objective (50X or 100X, N.A.=0.5). Finally the signal is spectrally sampled by a grating and detected by a liquid nitrogen cooled InGaAs detector array [3.5].

b) Base wafer and series measurement

The first µPL measurement is done with the base wafer, which is a fully active wafer, before applying any processing. The spectrum is shown in Fig. 3.10. One can see that the peak wavelength is around 1550nm, as designed, with a FWHM of about 70nm.

---

[4] The µPL is done together with Mehmet Dundar and the author thanks Mehmet Dundar for his help in the measurement.

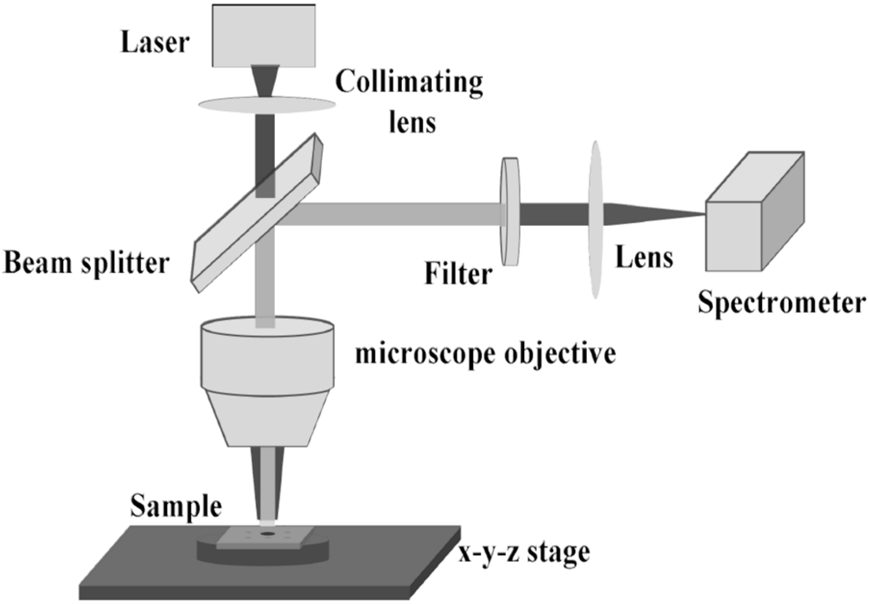

Figure 3.9: Micro PL setup [3.5]

Next a series of measurements is done for the small active regions with regrown passive material around them. In Fig.3.11 and Fig.3.12, two groups of submicron structures (octagon series and hexagon series), with dimensions varying from 250 nm to 2.5 µm in side length are measured. First of all, one can see that the photoluminescence intensity increases with the area of the active region which is expected. Nevertheless in order to get a clear picture of the relation between the photoluminescence intensity and active region area, a quantitive analysis is presented. Here the integrated intensity is defined as the integral of the PL spectrum from 1420nm to 1580nm, as shown in Figure. 3.13. The integrated PL intensity increases linearly with the active area, which implies that the processing did not result in an area of damaged (non-emitting) material at the edges of the active regions.

Second, if the size of the active region decreases, the PL peak wavelength is gradually shifted to shorter wavelengths. This is unexpected and we will go deeper into this aspect later in Section **e)**.

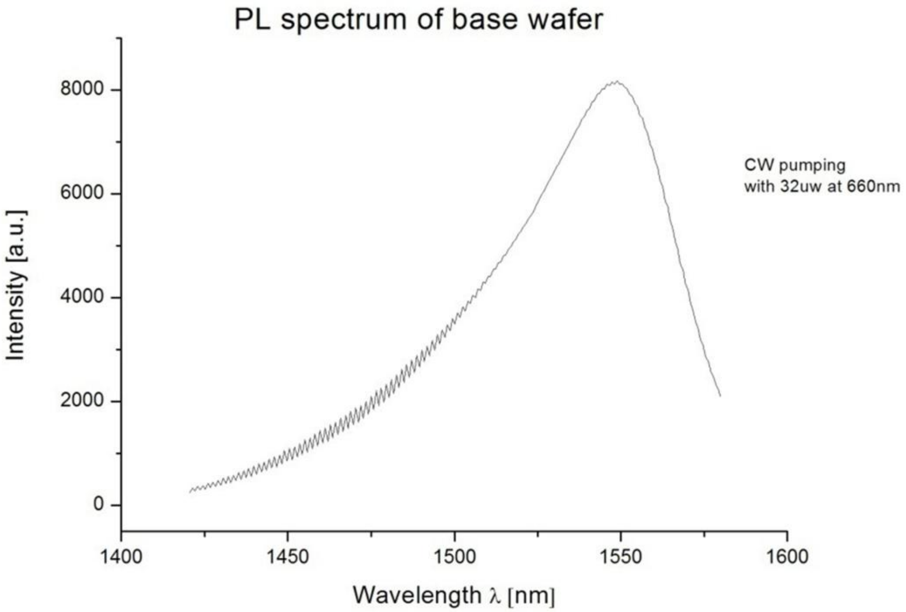

Figure 3.10: Micro PL of the base wafer (4 Quantum wells)

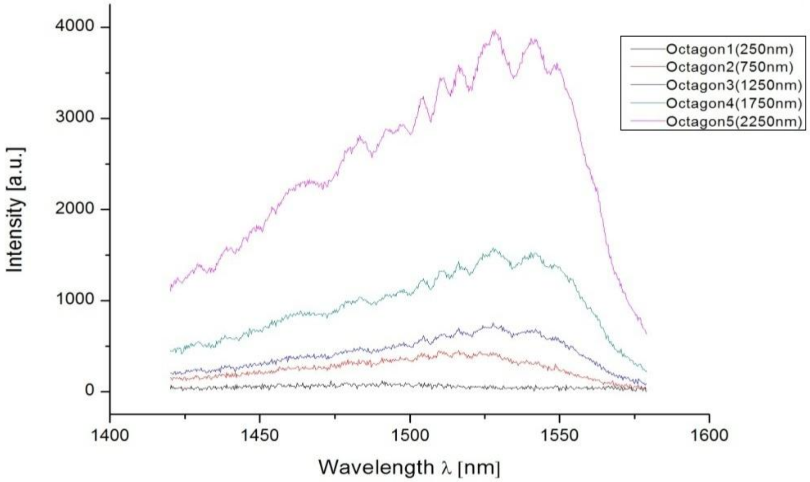

Figure 3.11: Micro PL spectrum of the small active structures (Octagon series)

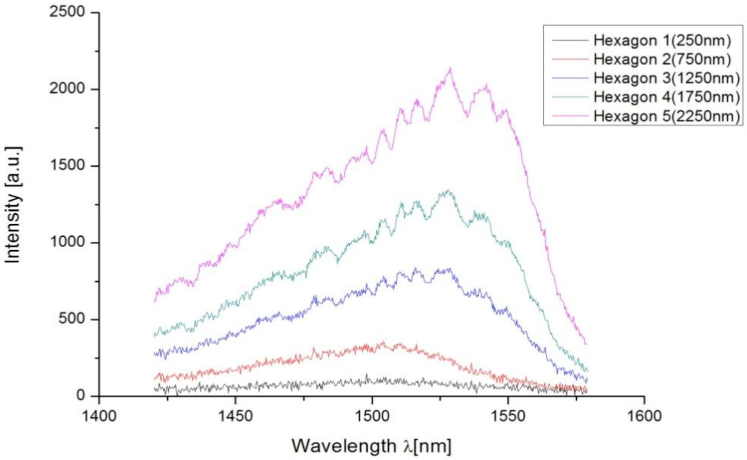

Figure 3.12: Micro PL spectrum of the small active structures (Hexagon series)

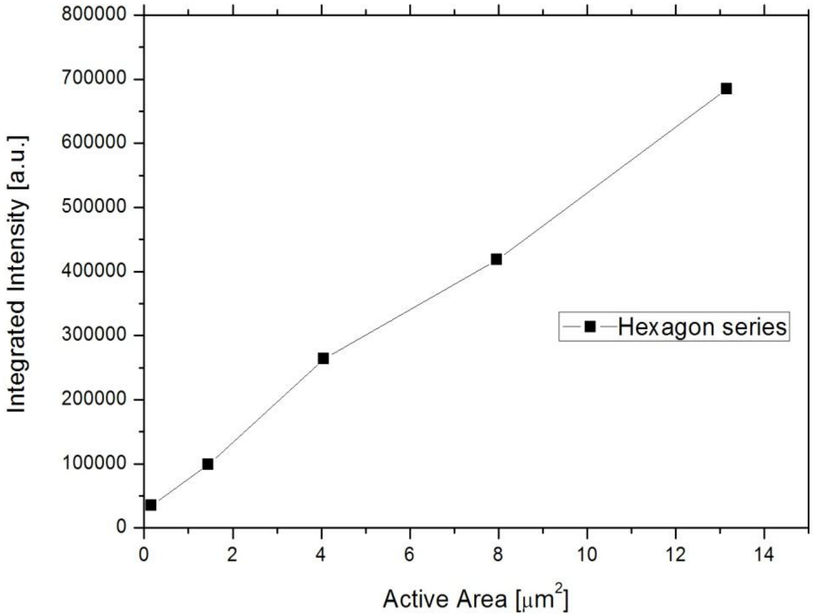

Figure 3.13: PL intensity vs the active area size (Hexagon series)

c) Measurement techniques for submicron structures

In Fig.3.11 and Fig.3.12 the PL spectrum peak from the smallest submicron active area is not so clear as compared to that from the larger active areas. The reason is that for small active areas, the photoluminescence intensity is quite small. Two methods can be used to capture this small signal. The first one is to increase the pumping power. The harder the QWs are pumped, the more light they will emit. Fig.3.14 and Fig.3.15 show the PL spectrum of the smallest active structures (Hexagon and Octagon with a 250nm wide side), when the pumping power is increased.

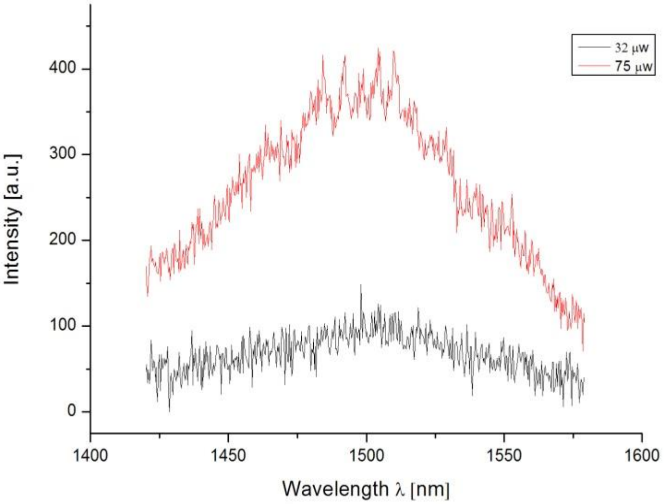

Figure 3.14: Comparison of PL spectrum under different pumping power (Hexagon 250nm)

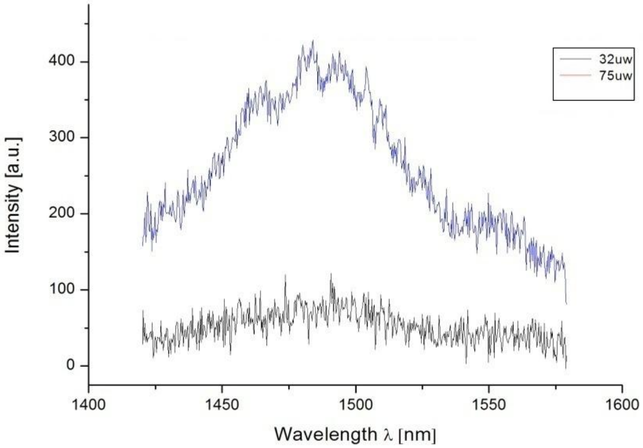

Figure 3.15: Comparison of PL spectrum under different pumping power comparison (Octagon 250nm)

The second measure to capture the small photoluminescence is similar to using an astronomical telescope to capture the weak light from a far distant star: increasing the exposure time to let more photons go into the detector. The difference is obvious as one can see in Fig. 3.16. After the exposure time is increased from 1 second to 3 seconds, the PL peak is getting much clearer.

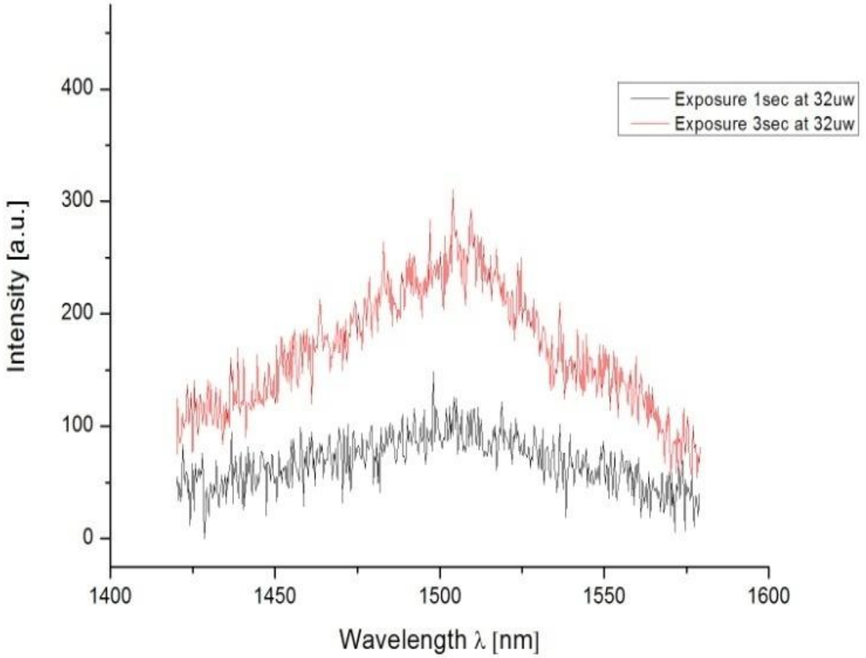

Figure 3.16: Comparison of PL spectrum from different exposure time comparison (Hexagon 250nm)

d) The trap model

In the last section, it is shown that by increasing the pumping power, the integrated output intensity is also increased. While this is expected, it is seen in Fig. 3.14 and Fig. 3.15 that the PL intensity increases more than the pumping power, which is unexpected. In order to get a precise relation between integrated PL intensity and pumping power, more measurements and analysis are done. Fig.3.17 shows the result of a micro PL measurement for an active structure with the octagon shape (side length=2.25um). One can see that the output power goes up when the pumping power is increasing. However, the relation is not linear. It is believed that this is due to the trap energy levels caused by defects and impurities in the QWs. Because of these trap energy levels, when the pumping power is small, the excited carriers are partially filling these trap energy levels, which results in non-radiative recombination (See Figure 3.18). At higher pumping power, these trap energy levels become filled, the additional excited carriers then contribute to the radiative recombination [3.6].

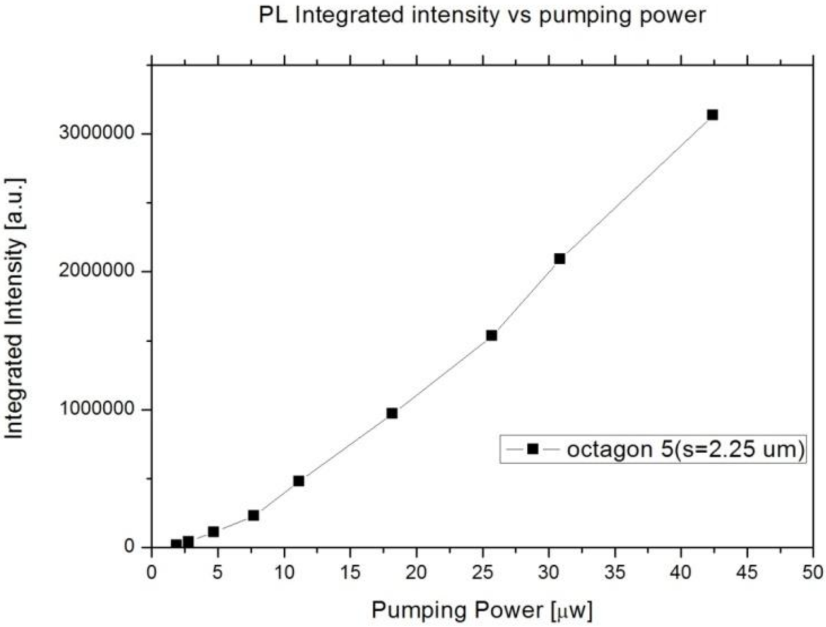

Figure 3.17: PL integrated intensity vs pumping power

In order to study the relation of the input and output light and to understand the physical mechanism, a trap model based on rate equations is used[5]. Fig.3.18 shows a simplified energy band diagram of this model. N_c and N_t are the carrier density of the conduction band and trap band, N_0 represents the number of the energy traps, τ_r, τ_1 and τ_2 are the recombination time constants of each of the three processes considered: a) radiative recombination (τ_r); b) transition from conduction band to trap (τ_1); c) transition from trap to valence band (τ_2).

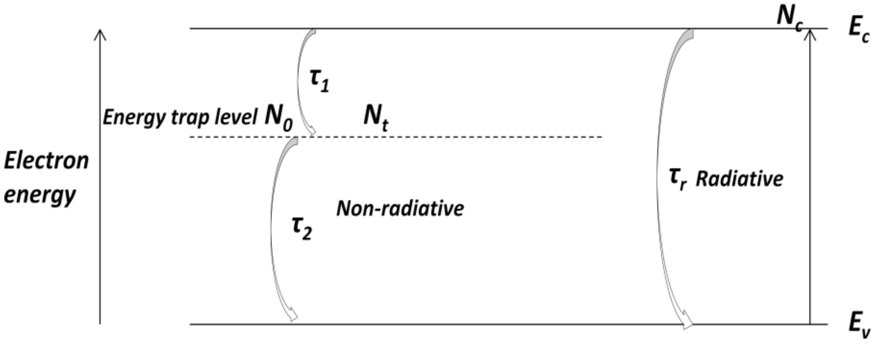

Figure 3.18: The trap model

$$\frac{dN_c}{dt} = c_1 I_{in} - \frac{N_c}{\tau_r} - \frac{N_c\,(N_0 - N_t)}{N_0 \tau_1} \tag{3.1}$$

$$\frac{dN_t}{dt} = \frac{N_c\,(N_0 - N_t)}{N_0 \tau_1} - \frac{N_t}{\tau_2} \tag{3.2}$$

$$I_{out} = c_2 \frac{N_c}{\tau_r} \tag{3.3}$$

In the rate equations, $c_1 I_{in}$ represents the number of carriers that the QWs absorb effectively, $\frac{N_c}{\tau_r}$ represent the number of carriers that give radiative

---

[5] The trap model is developed together with dr. J.J.G.M. van der Tol.

recombination, and $\frac{N_c\,(N_0-N_t)}{N_0\tau_1}$ represent the number of carriers that goes into the energy traps.

For the stationary condition, $\frac{dN_t}{dt}=0, \frac{dN_c}{dt}=0$

First, we assume an ideal case with no energy traps, then $\frac{N_c\,(N_0-N_t)}{N_0\tau_1}=0$

And we have

$$0=c_1 I_{in}-\frac{N_c}{\tau_r} \tag{3.4}$$

Putting eq. 3.4 into eq. 3.3, we obtain

$$I_{out}=c_2\frac{N_c}{\tau_r}=c_1 c_2 I_{in} \tag{3.5}$$

According to this formula the output power should increase linearly with the input pumping power, which is not the case as shown in Fig 3.18.

If we assumed traps we obtain from Equation (3.2)

$$N_t=\frac{\tau_2 N_c N_0}{N_0\tau_1+N_c\tau_2} \tag{3.6}$$

Combination of equation (3.1) and equation (3.2), leads to

$$c_1 I_{in}-\frac{N_c}{\tau_r}-\frac{N_c\,N_0}{N_0\tau_1+N_c\,\tau_2}=0 \tag{3.7}$$

By simplifying the above equation, a quadratic equation in N_c is obtained,

$$\frac{\tau_2}{\tau_r}{N_c}^2+\left(\frac{N_0\tau_1}{\tau_2}+N_0-c_1 I_{in}\tau_2\right)N_c-c_1 I_{in} N_0\tau_1=0 \tag{3.8}$$

Written as a standard quadratic equation

$$A{N_c}^2+BN_c+C=0 \tag{3.9}$$

we have

$$\begin{cases} A = \frac{\tau_2}{\tau_r} \\ B = \left(N_0 \frac{\tau_1}{\tau_2} + N_0 - c_1 I_{in} \tau_2\right) \\ C = -c_1 I_{in} \tau_1 N_0 \end{cases} \tag{3.10}$$

Since the PL output power is proportional to N_c as shown in eq. 3. 4, the solution of eq. 3.7 can be used to fit the measurement data. The fit is very good for the base wafer as well as for the processed samples, as shown in Figs. 3.19 , 3.20 and 3. 21, for different types of regrown structures.

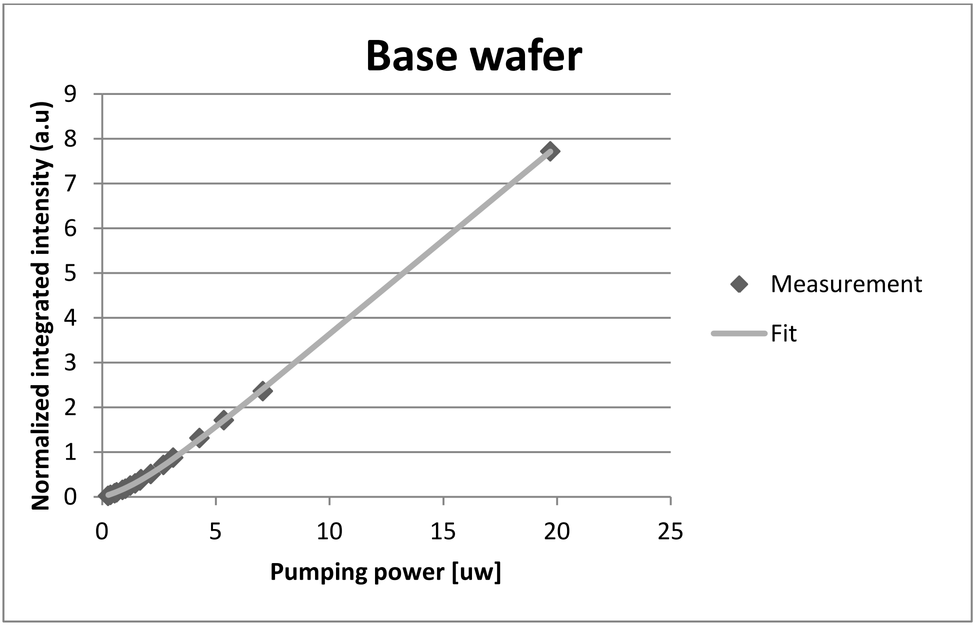

Figure 3.19: Trap model fitting for the base wafer

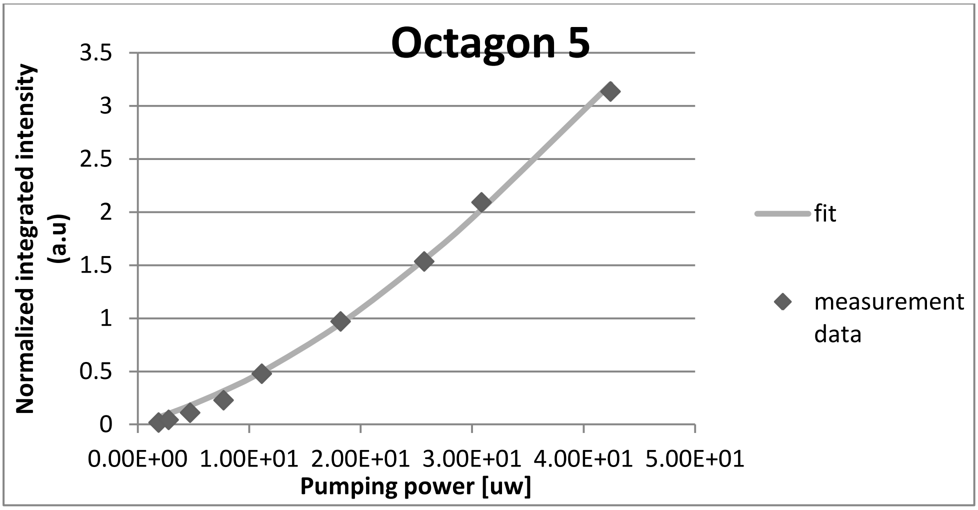

Figure 3.20: Trap model fitting for the processed structure-octagon 5

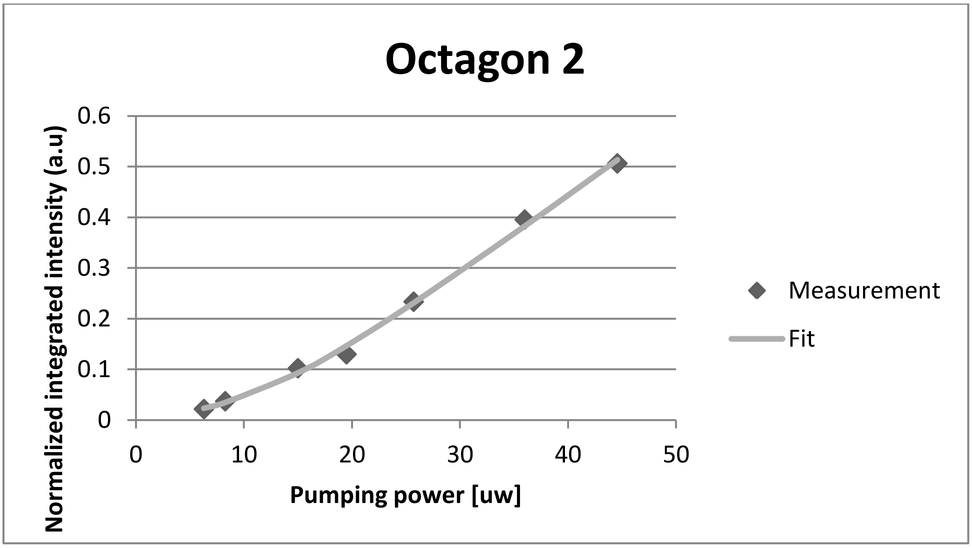

Figure 3.21: Trap model fitting for the processed structure-octagon 2

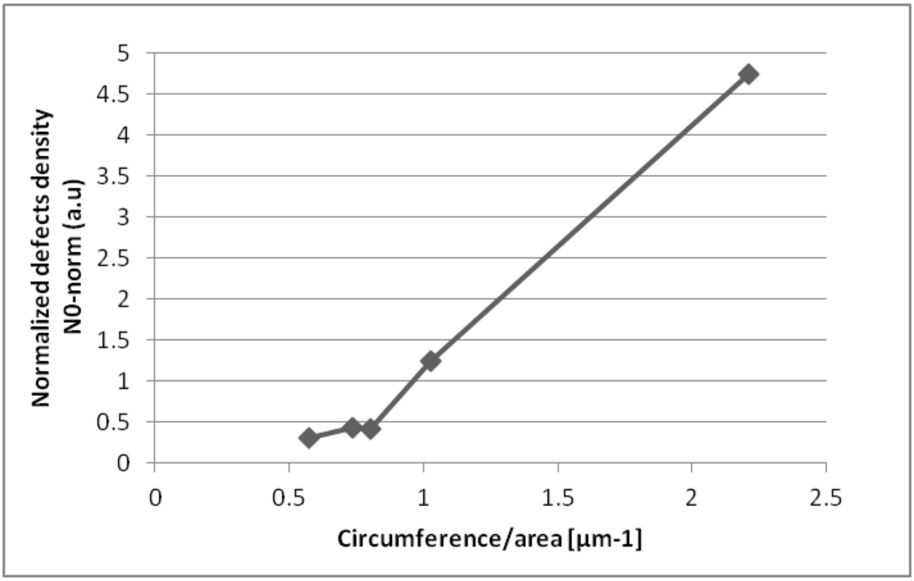

Figure 3.22: Normalized defect density vs circumference/area

Further, a relation between normalized defect density and area of the QWs can be found from this model, as shown in Fig 3.22. As one can see, the defect density is decreasing with increasing active region area, which means that smaller active structures have higher defect density. This is expected since the total number of defects increases linearly with the side-length of the structure, while the area of the active region is increasing quadratic with the side-length. Therefore after division by the active region area, the defect density is inversely proportional to the size of the active area. Here it should be mentioned that the normalized defect density ($N_{0\_norm} = N_0 / c_1 \tau_2$) is used, where c_1 is a constant and τ_2 the transition from trap to valence band.

It should be mentioned here that the trap model assumes one type of trap, while in reality different types can occur. This implies that the information from the fitting refers to an average effective trap. Therefore the results from the base wafer (where traps will be mainly caused by impurities) cannot be directly compared with those of the processed samples, where processing induced defects are dominant.

e) The blue shift

In Fig. 3.23 it is seen that as the size of the active region decreases, the PL peak wavelength is gradually shifted to shorter wavelengths. For example the base wafer has a peak wavelength of around 1550nm. For the smallest submicron octagon shaped active region, the peak wavelength is shifted to around 1500nm. It is found that for different shapes of the active structures, the same effect occurs, as one can see in Fig.3.24 for the hexagon series.

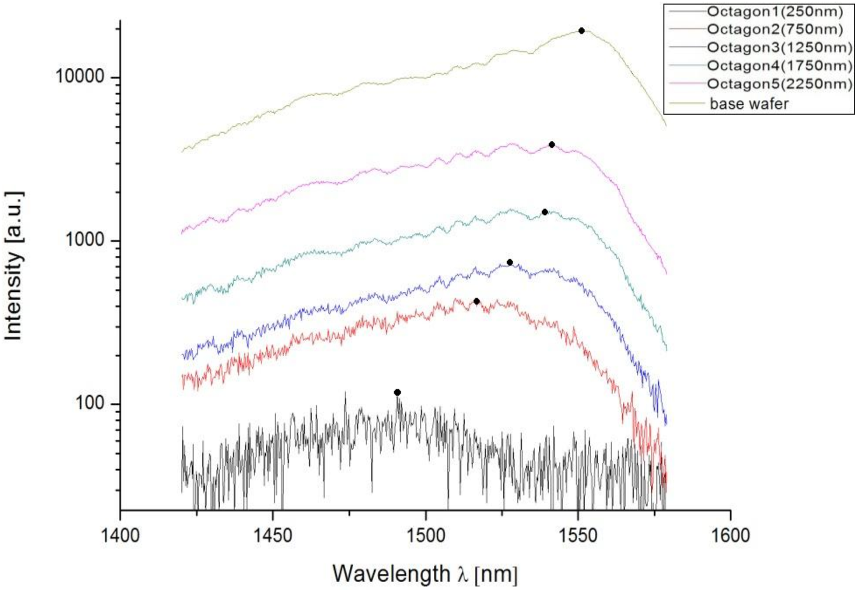

Figure 3.23: PL spectrum of the Octagon series (log scale) and the black dots represent the spectrum peaks.

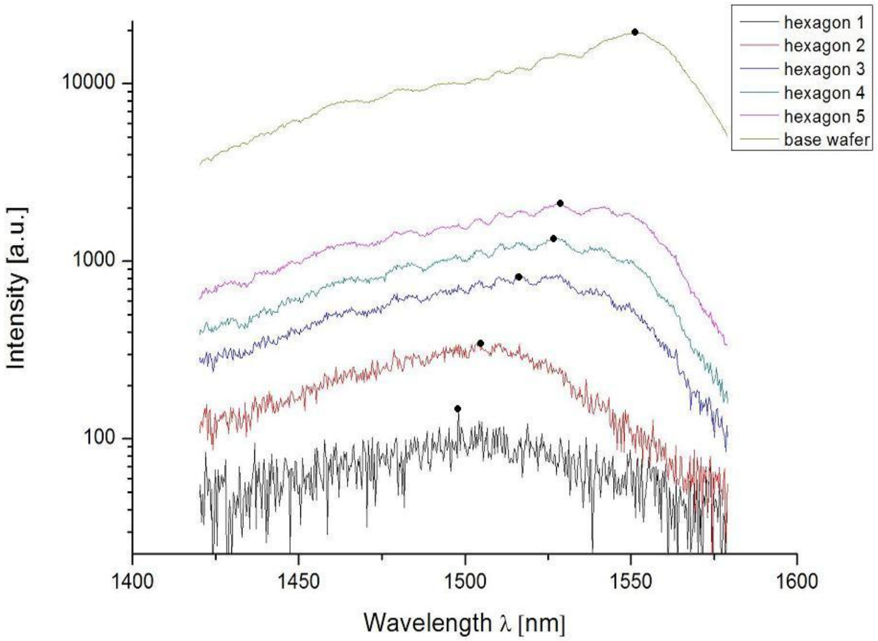

Figure 3.24: PL spectrum of the hexagon series (log scale) and the black dot represent the spectrum peak.

It is believed that this blue shift is due to the quantum well intermixing effect (QWI). QWI involves the inter-diffusion of atoms across the well barrier interfaces and is a well-known technique to modify the band gap of QWs [3.7]. However in our case, it happens unintentionally. During the fabrication process, InP reactive Ion etching is used to etch the active regions (see Section 3.3.1). It is known that defects will be formed on the sidewalls during this dry etching process. In the regrowth process, which uses high temperatures (up to 600 ℃), these defects will diffuse into the active region and cause intermixing of the QWs [3.8]. Consequently the energy levels of the QWs are changed. For smaller active regions, the defect density is higher as derived from Section d) and thus causes a larger blue shift in the spectrum. This is consistent with the trap model analysis which is explained in the last section.

To verify this hypothesis, several tests have been done. Fig. 3.25 shows the PL spectrum from a group of active regions that are dry etched, but not yet regrown. One can see that the peak wavelength is around 1540nm, which implies only a small blue shift (maximally 10 nm). The dry etching does create some defects on the side walls of the active region. However, without the high temperature of the regrowth process, these defects cannot diffuse through the QWs. Therefore the QWI effect is limited. Consequently, there is only a very small blue shift in the micro PL spectrum.

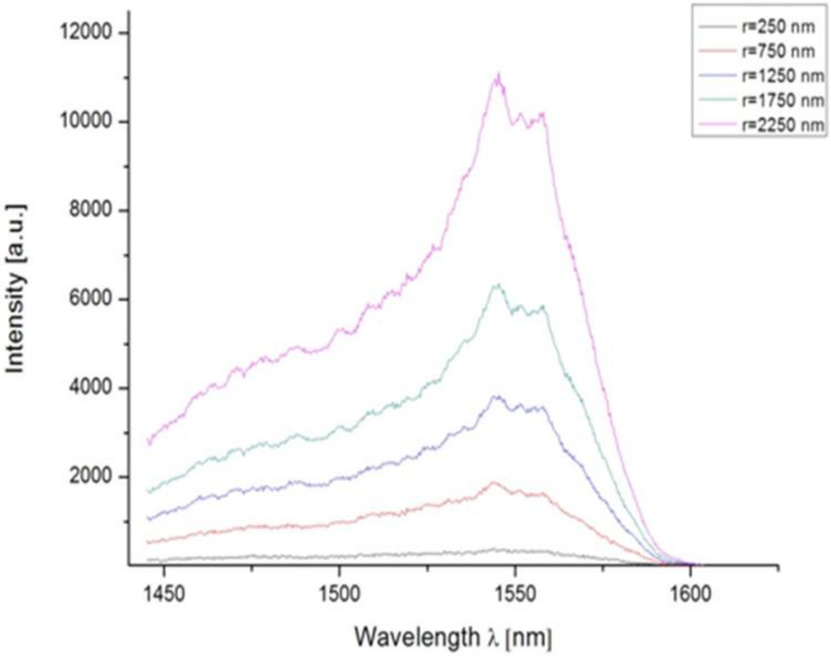

Figure 3.25: PL spectrum of the active structures without regrowth.

The question arises if there are any methods to prevent or at least reduce this unintentional QW intermixing effect. If the sidewall defects are created by dry etching, then chemical wet etching in a citric acid-based solution, which is used to form the overhang (see Section 3.3.1 for more details), can also remove these sidewall defects while forming the overhang. Therefore less defects can diffuse into the QWs during the regrowth step at high temperature and the QW intermixing effect is greatly reduced. To prove this hypothesis, a new set of tests are done and the result are shown in Fig. 3.26. This figure shows the PL spectrum of structures with different wet etching times. One structure is wet etched for 5mins and the other one for 10mins. One can see that the 5mins structure has a blue shift of 25nm compared with the base wafer, while the 10mins wet etched structure shows no detectable blue shift. Thus it is confirmed that defects are effectively removed with wet etching.

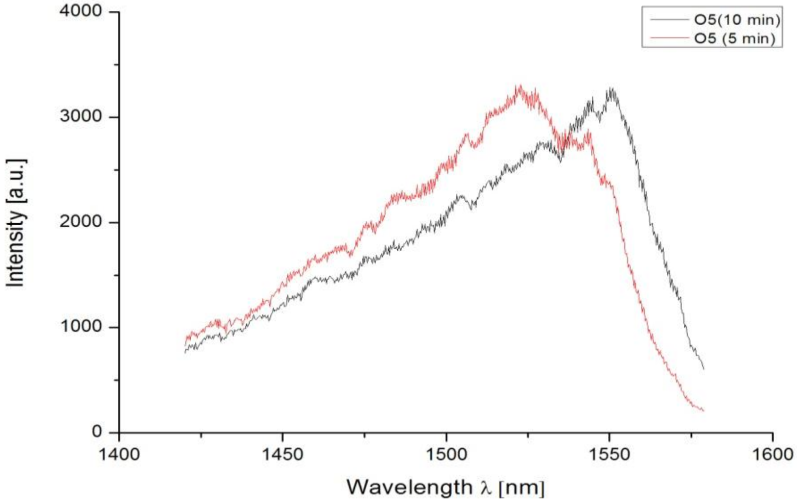

Figure 3.26: PL spectrum comparison of different chemical wet etching time (Octagon)

There is a limitation to use longer wet etching times. The chemical wet etching is used to create an overhang for the active passive integration. If the etching time is too long, the overhang will become too large, resulting in a bad surface morphology (see Section 3.3.2). Therefore a moderately longer wet etching time (7mins more for instance) seems best for removing sidewall defects and meanwhile keeping a good morphology for the active-passive interfaces. Moreover, compensation for the wavelength shift can also be made in the QWs design.

3.5 Conclusion and discussions

In this chapter the results of the submicron active passive integration on an InGaAsP material system are presented. This is an essential step in the realization of active PICs on the IMOS platform. The interfaces between the active and passive areas show a good quality in terms of morphology for active regions of different sizes. Furthermore it is found that there are no differences on morphology between the various shapes and orientations. This indicates that the processing and the regrowth do not depend significantly on the crystallographic directions of the material.

By using micro photoluminescence measurements, it is found out that the QWs within the sub-micrometer size active area, are able to emit light. However, defects are introduced, especially by dry etching the active materials. To investigate the relation between the defect density and the process, a theoretical trap model is investigated. The results predicted by this model fit well with the experimental data and it is found that the defect density is higher for smaller active structure.

Further a blue shift of the μPL spectrum is observed and we believe that this is due to the QW intermixing effect which is also caused by the defects. This blue shift also increases for smaller active structures which is consistent with the results from the trap model analysis, indicating that defect density is inversely proportional with the active region area. The possible degradation caused by the defects can influence the performance of the devices negatively, especially for submicron active regions. However, these defects can be removed, at least partially, by extra chemical wet etching (Citric acid) to reduce the degradation of the QWs.

Chapter 4

Dielectric aperture by AlInAs oxidation for IMOS

Electrical pumping of lasers is of key importance for practical application. In COBRA, we have developed a method using a current blocking AlInAs oxide layer around the active region in order to achieve efficient carrier injection into the active region. In this Chapter, the results of the current blocking by the dielectric oxidized AlInAs aperture are presented. Section 4.1 gives the motivation. In Section 4.2 the epitaxial growth and the experimental setup are introduced. Section 4.3 focuses on the process development and optimization. The results of characterization are shown in Section 4.4. First the morphology is checked by FIB and SEM. Next electrical measurements are done to verify that a high resistance is achieved after the oxidation of AlInAs. The Chapter ends with conclusions and discussions in Section 4.5.

4.1 Motivation

A main problem of photonic-crystal nanocavity lasers is that they are intrinsically difficult to pump electrically, because it is challenging to inject carriers through the membrane into the small PhC cavity in an efficient manner [4.1]. A large part of the injected carriers can be lost by leaking away along the path to the active region or by contributing to non-radiative recombination. For this reason, most of the demonstrations so far relied on impractical optical pumping [4.2]. Only a few groups have realized electrical injection into the PhC cavity[4.3]. For example in KAIST, lasing has been demonstrated in a photonic crystal nano-cavity by directing the current to the cavity region using a vertical p-i-n junction and running a current through a post as shown in Fig 4.1 [4.4]. The post works both as the path for electrical current injection and for heat sinking. This is a very smart technique. However, the post limits the quality factor of the cavity, restricts the choice of cavity design and requires a complicated fabrication procedure. In addition, a high threshold current of 260 uA was observed, which indicates the existence of a large leaking current. Recently another electrically pumped PhC laser is reported by Matsuo in NTT. In their work a buried QWs is used for the active region. For the electrical injection, Zn diffusion and Si ion implantation are used respectively for p- and n-type doping into an i-InP layer. However, the threshold current of the realized structure is still quite large which is due to leakage current into the substrate and sacrificial layers[4.5].

In order to efficiently inject carriers into the cavity, Al-containing oxides are used as a dielectric aperture for optical and current confinement. This technique has been used for vertical cavity surface emitting lasers (VCSELs) for a few decades and has enabled ultra-low threshold currents and high-output power VCSELs [4.6, 4.7]. Aluminum containing layers (AlAs) on GaAs are used for this and this material can be readily oxidized and then change from semiconductor into dielectric. This results in a current blocking layer. By controlling the oxidation openings in this layer, a dielectric aperture can be formed. However, achieving epitaxial growth of AlAs on InP is very difficult because of the large lattice mismatch [4.8]. Therefore an AlInAs layer, which can be grown lattice-matched to InP, is used for application of selective oxidation in the IMOS active devices. In combination with the submicron selective area re-growth technique [4.9], described in Chapter 3, we want to use the AlInAs oxide as a dielectric isolating layer in the IMOS active devices, such as lasers and amplifiers. Figure 4.2 shows a schematic view of the electrically pumped PhC laser in IMOS. The carriers will be injected through the metal electrodes. Due to the high electrical resistance of the AlInAs oxide layer, carriers are forced into the active region through the dielectric aperture and recombine inside the cavity. Since in this way, the leaking current can be avoided, the pumping efficiency can be increased and thus the threshold current and electrical power consumption should be reduced [4.10].

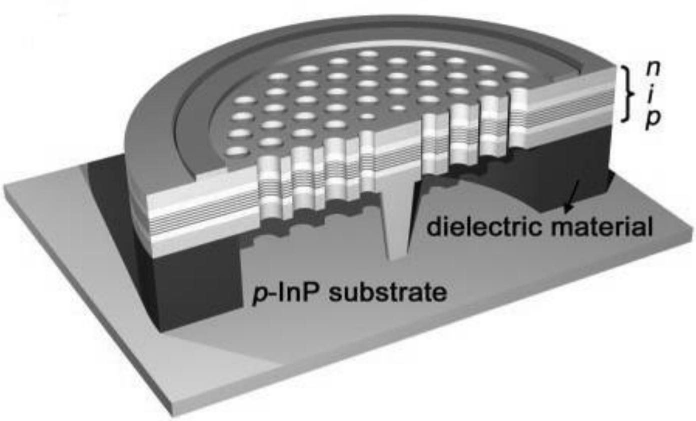

Figure 4.1: A schematic view of the electrically Injected PhC laser reported by KAIST [4.4]

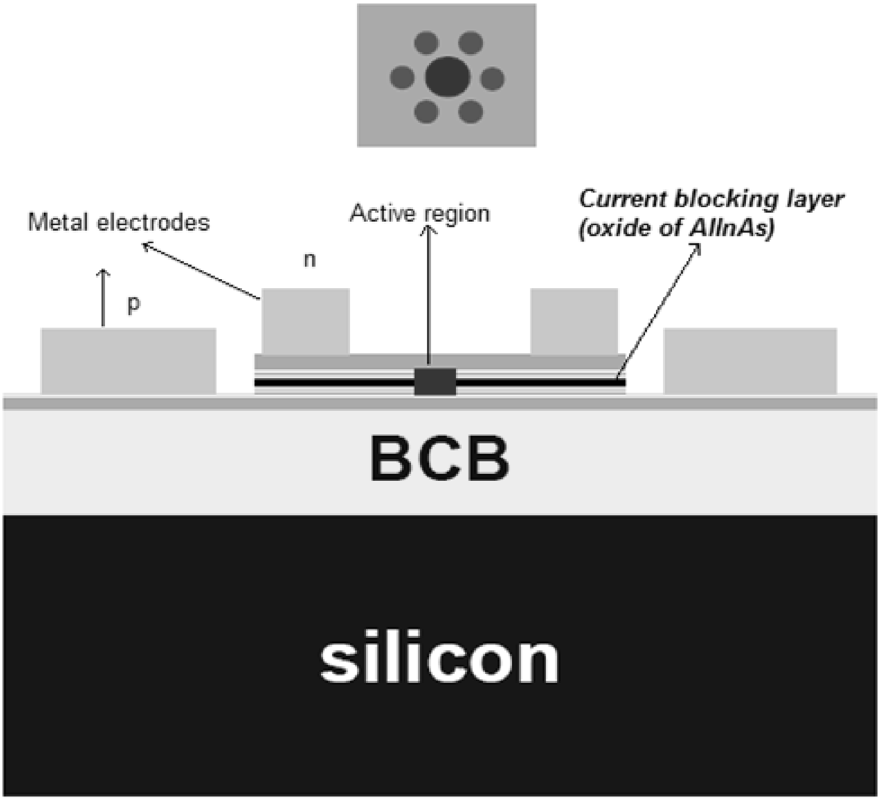

Figure. 4.2: Schematic view of an electrically pumped photonic crystal laser in IMOS

4.2 Design and experiment preparation

A series of experiments were performed to test the concept of the dielectric aperture. The wafers with a pin diode layer stack for the AlInAs oxidation experiment are grown by the former PHILIPS Photonics Lab. The setup to perform the AlInAs oxidation is built up in the NanoLab@TU/e clean room.

4.2.1 Wafer epitaxy

Fig. 4.3 shows the layer stack of the wafer grown[6] for the AlInAs oxidation test. On top is a 60nm InP cap layer. A 225 nm thick *p*-doped InGaAs layer is included for the p-side metal contact. Beneath this layer are a 50 nm thick *p*-doped InGaAsP (Q1.25), a 35 nm intrinsic InP layer and, most importantly, a 100 nm $Al_{0.48}In_{0.52}As$ layer, latticed matched to InP. The whole layer stack is epitaxially grown on a n-doped InP substrate. This layer stack is suitable for the realization of p-i-n diodes.

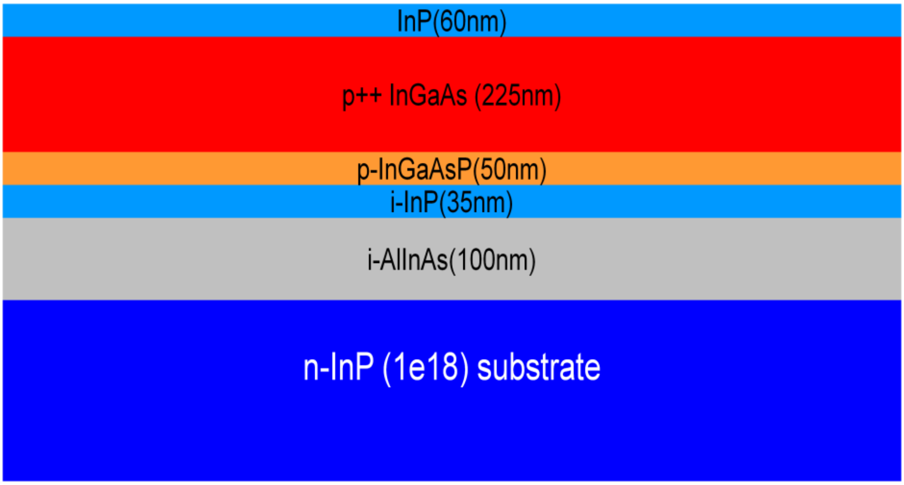

Figure 4.3: Layer stack of the wafer grown for the AlInAs oxidation test

4.2.2 Oxidation setup

The AlInAs oxidation setup is shown in Figure 4.4. The AlInAs oxidation is carried out in a horizontal quartz tube placed in a furnace. This furnace can be heated up to 1000 ℃. It is fed by nitrogen gas, which passes through a water bubbler maintained at 95 ℃ [4.11].

---

[6] The wafer for oxidation test is grown by Philips and the author thanks Peter Thijs for his help.

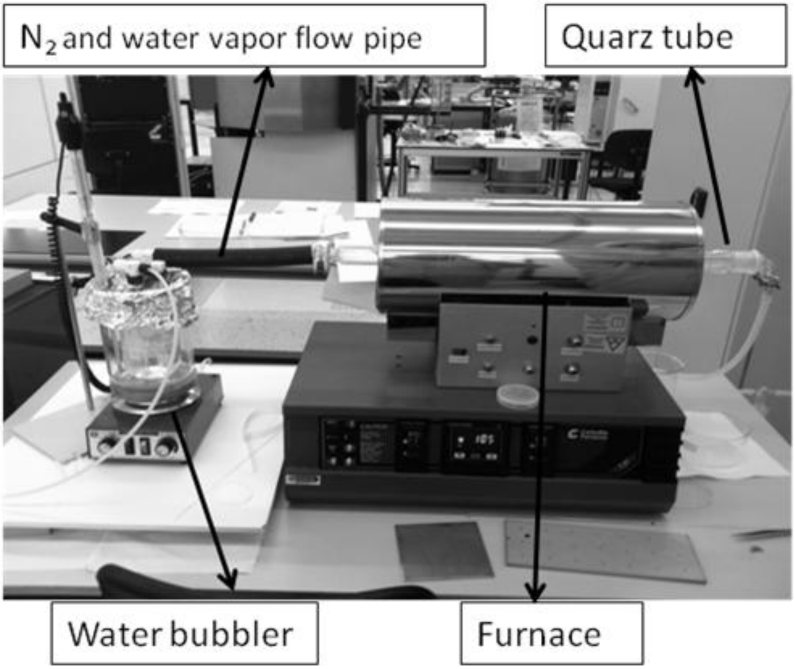

Figure 4.4: AlInAs wet oxidation setup[7] in the cleanroom.

4.3 Process exploration and optimization

For the IMOS platform, AlInAs oxidation is a new technique. This means that process development and optimization are necessary. It is essential to determine the relation between the oxidation conditions, temperature and time, and the oxidation results. This section will specifically focus on these issues.

Furthermore after process optimization, diodes are made to determine the electrical isolation properties of the AlInAs oxide. Structures with and

---

[7] The setup is built up together with Barry Smalbrugge and the author appreciate all his help.

without AlInAs oxidation will be measured, compared and analyzed using I-V measurements. In the next section, we will report on this.

4.3.1 Process description

For the AlInAs oxidation experiment, the realization of the diodes is done according to the process flow as shown in Figure 4.5. During the fabrication process, three optical lithography steps are used. After the cap layer removal and 50 nm SixNy deposition with PECVD, the first optical lithography (with positive photoresist HPR504) is used to define stripes. Next, a bromine-methanol (Br-methanol) solution is used to wet etch the stripes and form the mesas (see Fig.4.5.b). As shown in Fig. 4.5.c, after the removal of Si_xN_y, the AlInAs oxidation is performed at high temperatures (450 ℃-500 ℃) for a certain time, for instance from 30 minutes to 5 hours, depending on the oxidation depth that is required.

After a deposition of 50 nm of Si_xN_y, the second lithography (again with positive photoresist HPR504) is used to open the top surface of p-doped InGaAs for the *p* contact. The last optical lithography (with a negative photoresist AZ4533) is for the metal (Ti 60nm,Pt 75nm, Au 200nm), which is deposited using lift off to realize the electrical contacting of the individual devices. Finally metal n-contacts (Ti 60nm,Pt 75nm, Au 200nm) are deposited on the back side and the whole process is finished with a standard annealing step (325℃ for 30 sec) for the metal contact (see Fig.4.5.d). After finishing this processing, the samples are ready for characterization through an I-V measurement.

a) Base wafer

b) Optical Lithography_1,Br etching…

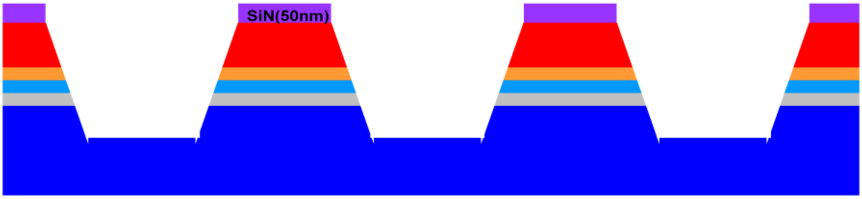

c) AlInAs oxidation

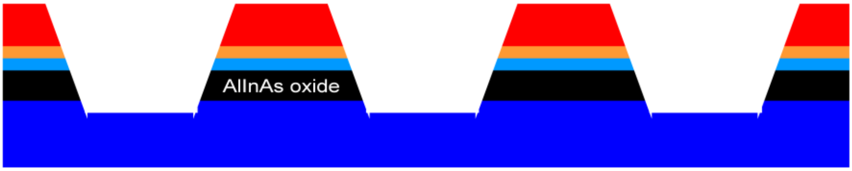

d) Isolation, Metallization and ready for electrical measurement

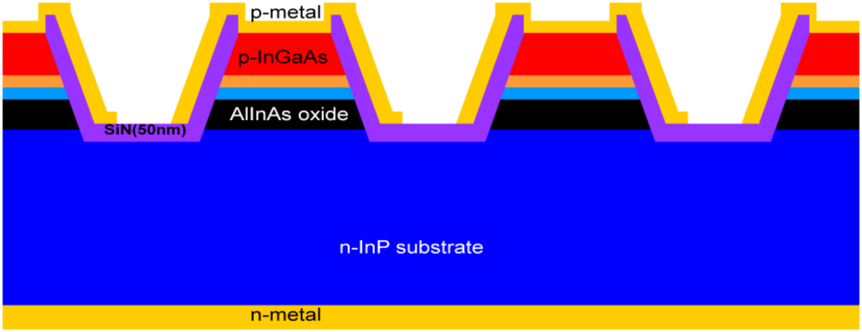

Figure 4.5: Key process flow for AlInAs oxidation

4.3.2 Lateral oxidation process development

The first oxidation test is done with a relatively low temperature (450 ℃), since too high temperature (more than 500 ℃) could cause the phosphorous desorption of the InP material (details will be explained in Section 4.3.2.c).

a) Strain effects of AlInAs oxidation

The oxidation is done immediately after the Br/methanol wet etching. Usually Br/Methanol wet etching gives the same slope through all materials [4.12]. Here, as shown in Fig. 4.6, apparently there are two slopes for the sidewalls: One above the AlInAs layer and one beneath it. This might be caused by a stronger etching of AlInAs than on the other semiconductor material. The first oxidation is done for 2 hours at 450 ℃ with Si_xN_y hard mask on top of the stripes. Afterwards, the sample is cleaved and Fig. 4.6 shows a cross section of the oxidized sample. The oxidized AlInAs is clearly visible as a dark line.

However, there is also a problem: The oxidized layer of AlInAs is delaminated from the InP substrate. This delamination indicates that there is a large strain. In order to find the source of this strain, various tests have been executed. The Si_xN_y hard mask on top could be a source of strain, since it is deposited at an elevated temperature in the PECVD. As the thermal expansion of Si_xN_y is quite different from that of the semiconductor materials, this leads to strain at room temperature. To investigate this, the Si_xN_y of the cleaved sample is removed. Fig. 4.7 shows the sample after the removal of Si_xN_y. There is a clear difference between Fig. 4.6 and Fig. 4.7. In Fig. 4.6. the edge of the upper layer is pulled up, resulting in a larger gap on the left edge than on the right. In Fig. 4.7, after Si_xN_y is removed, the delaminating gap is almost homogenous. This indicates that the strain is from the top and that the source of the strain is taken away after Si_xN_y is removed. Thus, Si_xN_y is a source of strain which can contribute to the delamination of the oxidized AlInAs.

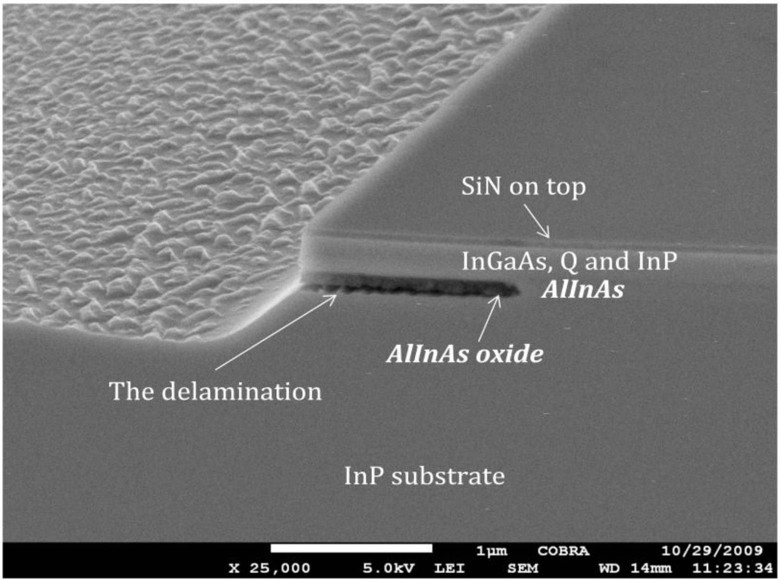

Figure 4.6: Oxidized sample with Si_xN_y mask still present (450 ℃ for 2 hours), the edge is formed by Br wet etching.

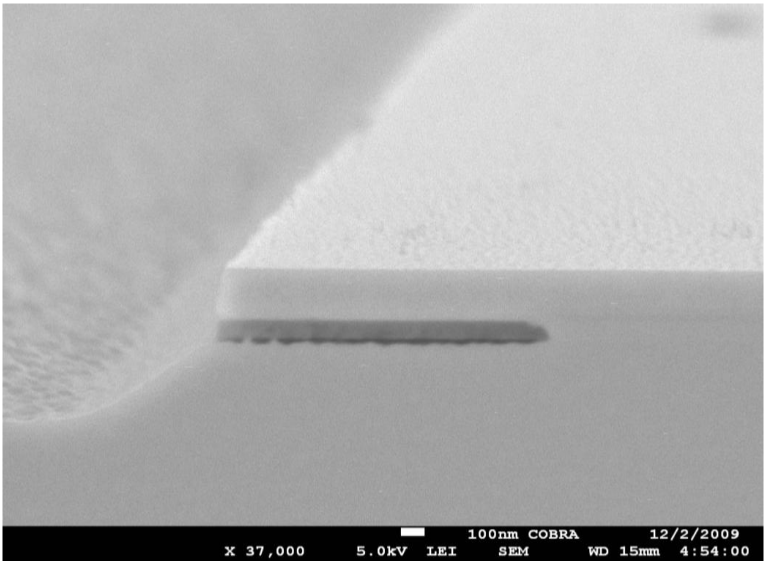

Figure 4.7: Oxidized sample with the Si_xN_y mask removed

Therefore in the 2nd run, the AlInAs oxidation is done after the Si_xN_y mask has been removed. Fig. 4.8 shows a cleaved sample from the 2nd run. As one can see, a strongly reduced delamination of the oxidized AlInAs layer from the InP substrate is observed, except for a few small voids. Since oxidation changes the composition of the AlInAs layer this layer is no longer lattice matched to InP anymore. Therefore there is a strain to be expected. Furthermore cleaving involves certain extra stress which could result in some voids locally. In order to support this hypothesis, one of the oxidized samples is etched by FIB which involves no stress and the cross section view is shown in Fig. 4.9. A good quality of oxidization of the AlInAs is obtained without delamination or local voids. Afterwards, also other FIB-cuts of the oxidized sample showed no voids. Therefore oxidized AlInAs layer should not be exposed to strain, since it then loses its stability. So far it is not yet possible to predict the effect of the oxidation related strain for use in a membrane.

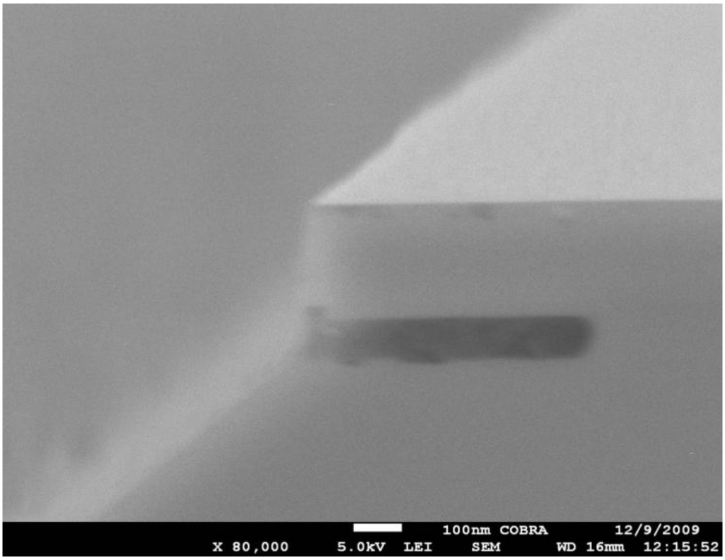

Figure 4.8: The 2nd Run of AlInAs oxidation without Si_xN_y mask.

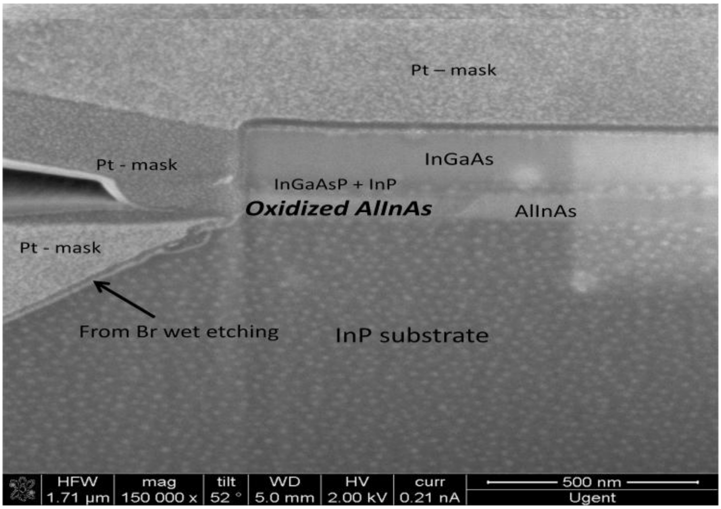

Figure 4.9: SEM picture of AlInAs oxide from Focused Ion Beam etching[8].

b) Oxidation conditions

AlInAs oxidation can be influenced by a few factors. Oxidation temperature and time have the largest influence on the oxidation process [4.13,4.14], they are used to control the oxidation depth.

As an example, Figs. 4.10 and 4.11 give a comparison of the influence of the oxidation temperature. In Fig. 4.10 the sample is oxidized at a relatively low temperature (450 ℃) for 2 hours and an oxidation depth of 680 nm is obtained. The oxidation rate of this sample is relatively low (0.062 $\mu m/min^{1/2}$), because of the relatively low oxidation temperature. For the sample shown in Fig. 4.11, a higher oxidation temperature (500 ℃) is used and one can see that even for an oxidation time of 75 minutes, an oxidation depth of 3.618 um is obtained which corresponds to a high oxidation rate of 0.418 $\mu m/min^{1/2}$. Since the wet oxidation of AlInAs is basically a diffusion process, the depth of the oxide formation as a function of oxidation time is

---

[8] This FIB is done by professor. dr. Gunther Roelkens and the author thanks him for the help.

best described by a square-root function and the temperature dependence follows an exponential curve (see Equation 4.1),

$$d = ce^{\frac{T}{T_0}}\sqrt{t} \tag{4.1}$$

where ***d*** is the oxidation depth, ***t*** is the oxidation time, ***T*** is the oxidation temperature and ***c*** is a constant.

If taking the experimental data (T_1=450℃, t_1=120min, d_1=0.68μm; T_2=500℃, t_2=75min, d_2=3.618μm) into eq.4.1, we get

$$e^{\frac{\Delta T}{T_0}} = 6.74 \tag{4.2}$$

where $\Delta T = T_1 - T_2 = 50K$ (4.3)

Then $T_0 = 26.2$K (4.4)

From Eq. 4.1, we can derive the expression for the constant ***c***

$$c = d/e^{\frac{T}{T_0}}\sqrt{t} \tag{4.5}$$

After putting $\boldsymbol{T_0}$ =26.2K, $\boldsymbol{T_1}$=723.15 K (corresponding to 450℃), $\boldsymbol{t_1}$=120min and $\boldsymbol{d_1}$=0.68μm into Eq. 4.3, we get

$$\boldsymbol{c}=6.4*10^{-14}\ \mu\text{m/min}^{1/2} \tag{4.6}$$

This result is confirmed also by using the other group data for 500℃ (T_2=500℃, t_2=75min, d_2=3.618μm). Therefore, we can write Eq.4.1 as:

$$d = ce^{\frac{T}{T_0}}\sqrt{t} \tag{4.7}$$

Where $\boldsymbol{T_0}$ =26.2K and ***c***= $6.4*10^{-14}$ μm/min$^{1/2}$.

This explains why a small temperature increase of 50 ℃ can lead to almost 3 µm oxidation depth increase, even for a short oxidation time. It should be mentioned Fig. 4.10 and Fig. 4.11 are both cleaved cross sections and therefore some voids are visible.

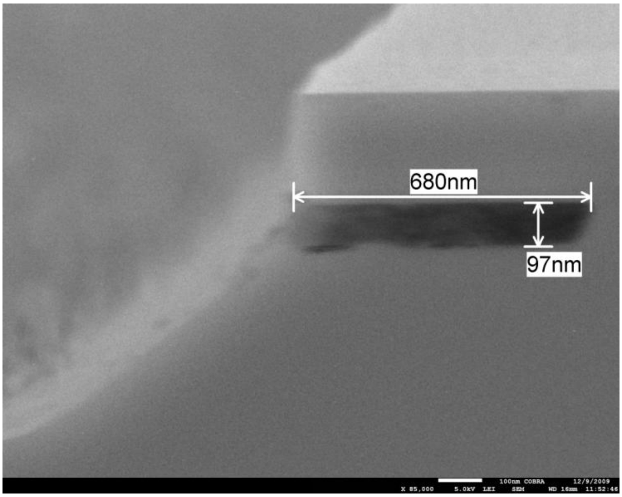

Figure 4.10: Sample oxidized at 450 ℃ for 2hours.

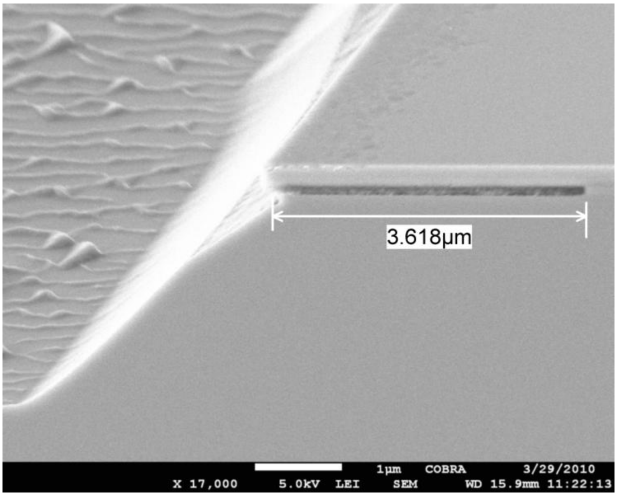

Figure 4.11: Sample oxidized at 500 ℃ for 75min.

c) Surface morphology

Although the oxidation is controllable, as discussed in the previous section, it is important to mention that the surface morphology is affected by high temperatures and long oxidation times. This degradation presents a stumbling block in the fabrication of devices utilizing these oxides. With InP-based devices, the samples experience heavy phosphorus loss in the exposed InP regions at high temperatures and thus become pitted [4.15].

Moreover it is also found that oxidation time plays a role. Figs. 4.12 and 4.13 show two samples oxidized at 500 ℃. The sample in Fig. 4.12 is oxidized for 40mins, while the sample in Fig. 4.13 is oxidized for 5 hours. The latter sample clearly experiences heavy phosphorus desorption, resulting in a pitted surface as can be seen from Fig 4.13.

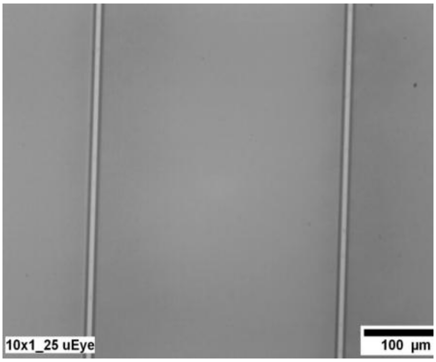

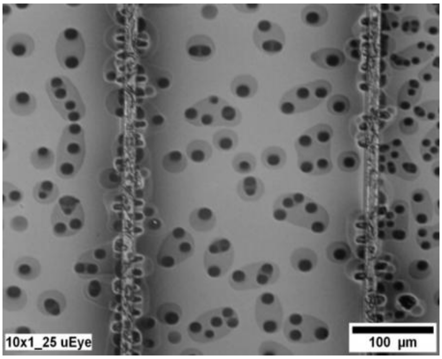

Figure. 4.12: Oxidation at 500 ℃ for 40mins. Figure. 4.13 Sample oxidized at 500 ℃ for 5 hours.

Therefore, to use AlInAs oxidation in the IMOS platform, a choice of the oxidation parameters should be performed based on the application. If there is a strict requirement for the surface quality, then a low oxidation temperature (e.g. 450 ℃) and a short oxidation time is recommended. Consequently, the oxidation depth will be also small. On the other hand, if a fast oxidation and a large oxidation depth are required, then a high temperature or long oxidation can be chosen.

4.4 Characterization

The final test of the AlInAs oxidation is done with a current-voltage (I-V) measurement. The aim is to check whether this small thickness of AlInAs oxide can give a sufficient electrical resistance to realize the desired current blocking function.

4.4.1 Diode structure

Fig. 4.5d shows a schematic view of the devices which are used to measure the electrical resistance of the AlInAs oxide. Stripes of the same length (8 mm), but different widths (from 2 μm to 10 μm) have been defined and etched. Metal contacts are put on both sides. A relatively high oxidation temperature (500 ℃) is used in order to obtain a high oxidation rate (0.42um/min$^{1/2}$). This is beneficial to have the narrowest stripes with a completely oxidized (AlInAs) layer.

4.4.2 Resistance measurement

The U-I measurement results are shown in Figure.4.15 and Figure.4.16. Figure.4.15 shows the U-I curve for an un-oxidized strip with a width of 5 um and a length of 8 mm. The differential resistance at high voltage (>0.6 Vols) is around 25 Ω, corresponding to a resistivity of 10 Ω·m.

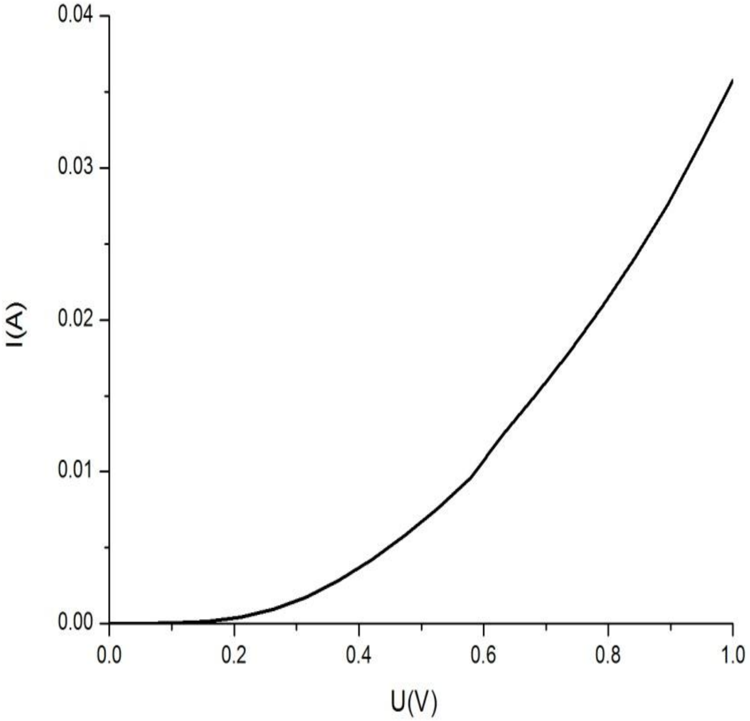

Figure 4.15: U-I measurement of a un-oxidized sample, ridges with 5 µm width.

Fig. 4.16. shows the U-I curve of a completely oxidized sample, where the stripe is 8 mm long and 3.2 µm wide. As one can see, up to 3 Volts only 50 µA current is measured, which corresponds to an electrical resistance of at least 60 kΩ. After correcting for the dimensions, a resistivity of $1.53*10^4$ Ω·m is obtained. Compared with the resistance of the un-oxidized sample, the oxidation of AlInAs brought an increase of the electrical resistivity by more than 3 orders of magnitude. This clearly shows that oxidation of AlInAs can provide sufficient electrical resistance for effective current blocking.

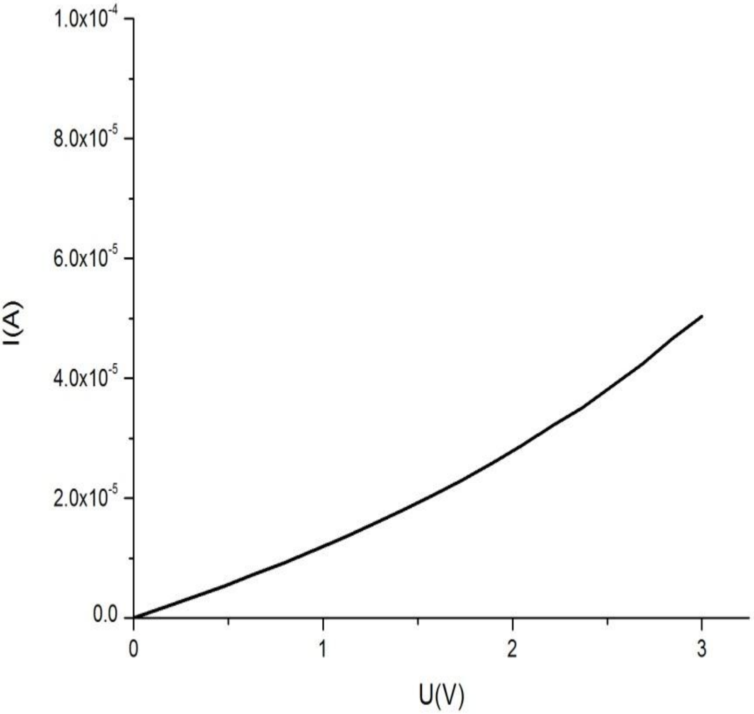

Figure 4.16: U-I measurement of a complete oxidized (AlInAs) sample.

4.5 Conclusions

In this chapter the feasibility of using AlInAs oxidation for current confinement and blocking in the IMOS platform is explored. Various tests have been executed for the process development and optimization. The influence of temperature and time on the oxidation rate and surface morphology are investigated. It is found that high oxidation temperatures and long oxidation times will increase the oxidation depth dramatically, but can also degrade the surface quality because of the phosphorus loss.

The characterization of this technique focuses on two aspects. The first one is morphology evaluation. After process optimization, especially after removing the Si_xN_y mask before oxidation, a good morphology is obtained and no delamination of materials is observed in the FIB morphology evaluation. Secondly, an electrical analysis is made to check the increase of the electrical resistance brought by oxidation of the AlInAs layer. It is found that the electrical resistance is increased by more than 3 orders of magnitude by the oxidation of a 100 nm thick AlInAs layer. The high electrical resistance brought by the AlInAs oxidation makes this technique very promising for current blocking in the IMOS platform. However, it should be mentioned that AlInAs oxidation also causes strain in the layers. Since oxidation changes the composition of the AlInAs layer, this layer is no longer lattice matched to InP. Thus an oxidized AlInAs layer should not be exposed to stress, since it then loses its stability. So far it is not yet possible to predict the effect of the oxidation related strain for use in a laser.

Chapter 5

Design and simulation of a photonic crystal laser cavity on IMOS

As mentioned in Chapter 1, future microprocessors will operate with unprecedented high bit-rates that electrical interconnect networks alone cannot support. To solve this problem, it is predicted that a photonic membrane on top of the complementary metal oxide semiconductor (CMOS) circuit can provide the high speed on-chip data transport. Photonic Crystal (PhC) lasers, with their ultra-high Q-factor and very small mode volume, is potentially a good candidate to achieve on-chip optical interconnects. Because they can be driven by a very small threshold current and consume small amount of operating energy. Meanwhile, a receivable amount of output power is also feasible [5.0]. In Chapter 3 and 4, it is shown that we are able to realize active-passive integration within a submicron range and obtain a high electrical resistance by a thin oxidized AlInAs layer. The success of these two techniques makes it possible to make a direct electrically pumped PhC membrane laser in the IMOS platform. Before practically making a laser, theoretical and numerical investigations and *calculations are essential. Therefore Chapter 5 focuses on the design and simulation of a photonic crystal cavity on the IMOS platform. Section 5.1 first gives an introduction and background of PhC crystal lasers. In Section 5.2 the simulation environment is briefly introduced. The laser cavity design is shown in Section 5.3. Section 5.4 focuses on the optical simulation of the chosen PhC cavity. Since we want to make an electrically pumped photonic crystal laser, Section 5.5 focuses on the electric calculations to optimize the layer stack for the photonic crystal laser. This chapter ends with conclusions and discussions in Section 5.6.*

5.1 Photonic crystal

As known in solid-state physics, the band structure of a crystal describes those ranges of energy that an electron is “forbidden" or “allowed" to have. Photonic crystals (PhCs) are similar periodic structures, which affect the motion of photons in a similar way like the periodicity of a semiconductor crystal affects the motion of electrons. Because of the periodic modification of the refractive index of the material, band gaps may exist. This means that photons with certain frequency within the band gaps are forbidden to propagate [5.1]. The concept of a Photonic Crystal was introduced by Yablonovitch and John in 1987 independently. Yablonovitch focused on the control of spontaneous emission of the emitters when they are placed in photonic crystals [5.2]. John focused on the localization of the light by using the photonic crystal [5.3].

The periodicity in the refractive index can occur in all three dimensions and therefore PhCs can be classified into one dimensional (1D), two dimensional (2D) and three dimensional (3D) PhCs, as shown in Fig. 5.1. 1-D PhCs have band gaps in one direction and actually the structure was known long before the PhC concept was invented. The Distributed Bragg Reflector (DBR), which was investigated and used for several decades is actually a standard 1-D PhC. Various applications of the DBR have been realized, among them the best known are vertical cavity surface emitting lasers (VCSEL) for instance. 2-D PhCs have band gaps for propagation in a plane and 3D PhCs can have band gaps in all directions. The first fabricated 3D photonic crystal was successfully demonstrated with a complete photonic band-gap by Yablonovitch’s team [5.4]. However, to fabricate a small scale 3D photonic crystal is still a challenging task. A 2-D photonic crystal slab (membrane) has appeared as a promising route to overcome the fabrication limitation of its 3-D counterparts, because it is easier to fabricate and analyze. Various 2-D photonic crystal devices such as lasers [5.5], splitters [5.6] and high Q microcavities [5.7,5.8] have been demonstrated experimentally.

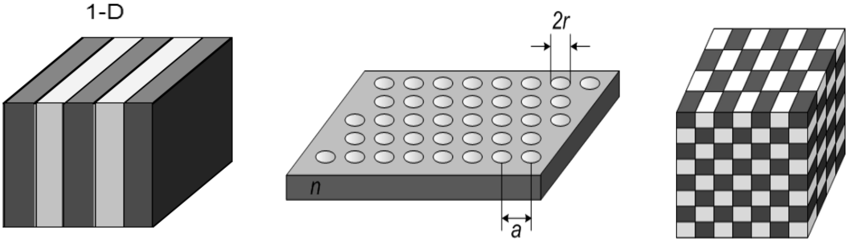

Figure 5.1: Schematic pictures of PhCs in (a) one dimension, (b) two dimensions and (c) three dimensions [5.1].

The propagation properties of light in PhCs are governed by Maxwell's equations which are

$$\nabla \cdot \mathbf{B} = 0 \tag{5.1}$$

$$\nabla \cdot \mathbf{D} = \rho \tag{5.2}$$

$$\nabla \times \mathbf{E} + \frac{\partial \mathbf{B}}{\partial t} = 0 \tag{5.3}$$

$$\nabla \times \mathbf{H} - \frac{\partial \mathbf{D}}{\partial t} = \mathbf{J} \tag{5.4}$$

In these equations, D and B are the displacement and magnetic induction, E and H are the electric and magnetic fields, ρ and J are the free charge and current densities. With the assumptions of small electric fields in a homogenous, low-loss medium with a non-dispersive dielectric constant ε, a magnetic permeability μ close to 1, no free charges and currents, and harmonically varying fields, the four equations can be incorporated into one,

$$\nabla \times \left(\frac{1}{\epsilon(\mathbf{r})} \nabla \times \mathbf{H}(\mathbf{r}) \right) = \left(\frac{\omega}{c} \right)^2 \mathbf{H}(\mathbf{r}) \tag{5.5}$$

Here r is the position vector, c is the speed of light in vacuum. Eq. 5.5 is the master equation. If we identify the left side of the master equation as an operator $\hat{\Theta}$ acting on H(r) to make it look like a traditional Eigen value problem, then the master equation is often written as

$$\hat{\Theta}\mathbf{H}(\mathbf{r}) = \left(\frac{\omega}{c} \right)^2 \mathbf{H}(\mathbf{r}) \tag{5.6}$$

While the quantum mechanical solid state equivalent is given by

$$\hat{H}\Psi = E\Psi, \text{ with } \hat{H} = -\frac{\hbar}{2m}\nabla^2 + V(\mathbf{r}) \tag{5.7}$$

Here ψ is the electron wave function, E is the energy, ħ is Plank's constant divided by 2**π**, m is the electron mass and V(r) is the potential.

For periodic structures like PhC,

$$\epsilon(\mathbf{r}) = \epsilon(\mathbf{r} + \mathbf{R}) \tag{5.8}$$

where R is a lattice vector (lattice constant for PhC), according to the Bloch's theorem the Eigen function is written as

$$\mathbf{H_k}(\mathbf{r}) = e^{\mathbf{ikr}}\mathbf{u_k}(\mathbf{r}) \tag{5.9}$$

In which $u_k(r)$ is a periodic function on the lattice: $u_k(r) = u_k(r + R)$ for all lattice vectors R. Because one key factor of Bloch states is that the Bloch state with wave vector k_r and $k_r + mk'$ are identical, where k_r is the wave vector in the irreducible Brillouin zone, m is any integer and k' is a reciprocal lattice vector, the master equation can be rewritten in the terms of the Bloch fields u_k:

$$\hat{\Theta}_{\mathbf{k}} \mathbf{u}_{\mathbf{k}} = \left(\frac{\omega}{c}\right)^2 \mathbf{u}_{\mathbf{k}} \tag{5.10}$$

$$\hat{\Theta}_{\mathbf{k}} = (i\mathbf{k} + \nabla) \times \frac{1}{\epsilon(\mathbf{r})}(i\mathbf{k} + \nabla) \tag{5.11}$$

The information contained in these functions is called the band structure of the photonic crystal. For each k a discrete set of eigenvalues $\omega_n(k)$ exist, where n is the band number. The frequency of each band $\omega_n(k)$ will vary continuously as k varies. For instance, the band structure of a 200nm PhC InGaAsP slab (n = 3.37) with air holes is displayed in Fig. 5.2. For this structure, there exists a band gap (from 1.35 µm to 1.65 µm) for the TE mode.

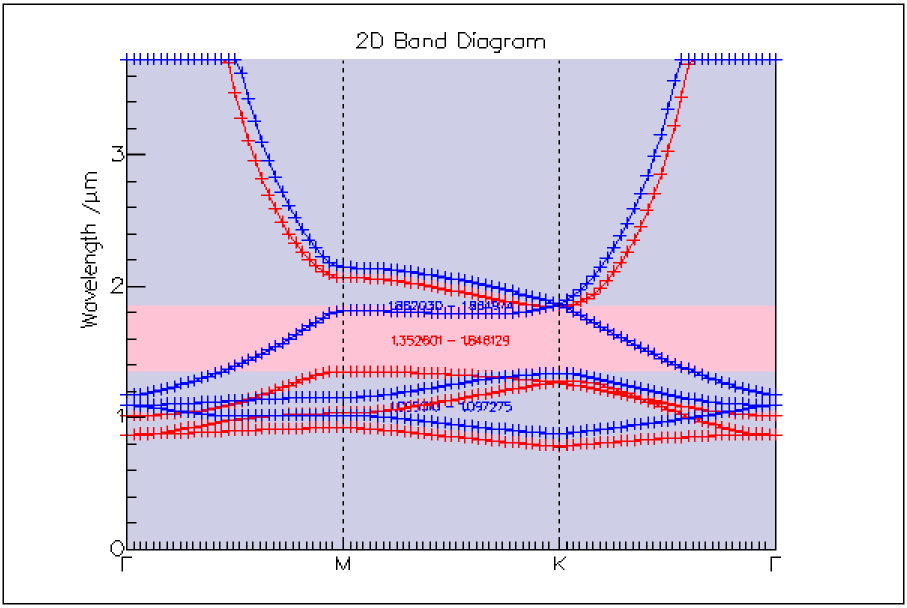

Figure 5.2: Band structure of 2D PhC InGaAsP (n = 3.37) 200nm slab with triangular lattice of air holes. The red curve shows the TE band and the blue curve shows the TM band. The thickness of the slab is 0.4a. The diameter of the hole is 0.7a.

Although various types of PhC laser have been shown by different groups, most of them still rely on optical pumping, rather than electrical pumping which is much more practical. The principal hurdle of making an electrically pumped photonic-crystal nanocavity laser is that it is challenging to inject carriers through the membrane to the active region in an efficient manner. Still, electrically pumped PhC membrane lasers have been realized in KAIST [5.9]. However, the performance of this device clearly needs improvement. In their structure, lasing has been demonstrated in a photonic-crystal nanocavity by directing the current to the cavity region using a vertical p-i-n junction and a current post, as shown in Figure.5.3. However, the current post limits the quality factor of the cavity, restricts the choice of cavity design, and requires a complicated fabrication procedure.

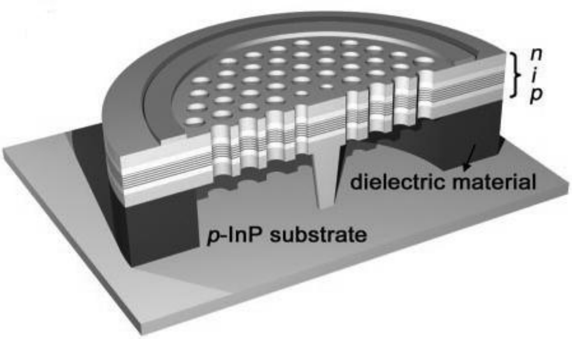

Figure 5.3: a schematic view of the electrically injected PhC laser made by KAIST [5.9].

In COBRA, we aim at making a directly electrical pumped PhC laser in the IMOS platform. Together with the techniques of submicron active-passive integration and AlInAs oxidation developed previously, it is expected to make electrically injected PhC lasers with high pumping efficiency and small threshold current as well as low electrical power consumption. This chapter describes the design and simulations of one type of photonic crystal cavity. We believe that this type of cavity is a promising candidate for the electrically pumped photonic crystal laser in IMOS. In the next section the simulation tool used for studying the PhC cavity is introduced and the subsequent section describes the cavity model chosen.

5.2 Simulation Environment

The finite difference time domain (FDTD) method is used to perform the cavity simulations. The FDTD method, which uses a computational grid with a certain spacing, is a powerful numerical algorithm for directly solving Maxwell's equations in each time interval. It can be used to investigate the interaction of light fields with virtually arbitrary structures. FDTD is a very accurate numerical method, since there is no approximation adopted, except the discretization and limitation of the space and time domains [5.10]. However, for the same reason, it is also quite memory and time consuming, especially for three-dimensional (3D) cases. The FDTD method is included in the software package “Lumerical” and it can perform 1D and 2D as well as 3D calculations. Compared with its 2D counterpart, 3D simulations are more accurate. The disadvantage of the latter is that it is time and memory consuming. In our simulations, using a server with a large memory, 3D calculations are performed for the designed photonic crystal cavity.

In the simulations, perfectly-matched layers (PML) are used to avoid parasitic reflections from the boundaries of the calculation window. A structure can be excited with a pulse or with a continuous wave signal, either with a Gaussian beam profile or as a certain waveguide mode. To get the frequency response of a device, a pulse excitation is used. The bandwidth of the calculation is determined by the inverse of the time duration of the pulse. The field at a certain wavelength can be found by excitation with a continuous wave signal [5.11].

5.3 PhC cavity model design

There is a variety of PhC cavity types. In our case a 1-line defected waveguide (W1 like) cavity is chosen as shown in Fig.5.3. In the previous studies done at NTT, this type of cavity has shown a high quality factor [5.12,5.13] and has a good tolerance to manufacturing errors. However in their work this cavity is used for a PhC laser in a suspended membrane in air which is however difficult to integrate into PICs. In the IMOS platform, the whole III-V membrane is bonded via BCB on Si which is mechanically much more stable for large photonic integrated circuits. A second difference is the use of a dielectric aperture, formed by AlInAs oxidation (Chapter 4), in order to obtain the direct electrically pumped photonic crystal laser.

A 2-D model of the designed PhC cavity is shown in Fig.5.4, a light source (TE polarized) is placed in the middle of the cavity. The dark region represents the active material, which contains embedded InGaAsP QWs with

Q 1.2 as the barrier layers. The key feature of this cavity is an extremely small buried active region located in a straight W1 line-defect PhC waveguide in a Q (1.2) membrane. In-plane optical confinement is realized both by the photonic crystal band gap and the refractive index difference between the active region and the passive part as shown in Figure 5.5. As in all 2D PhC slabs, the vertical optical confinement is provided by the total internal reflections between the membrane layer and BCB and air.

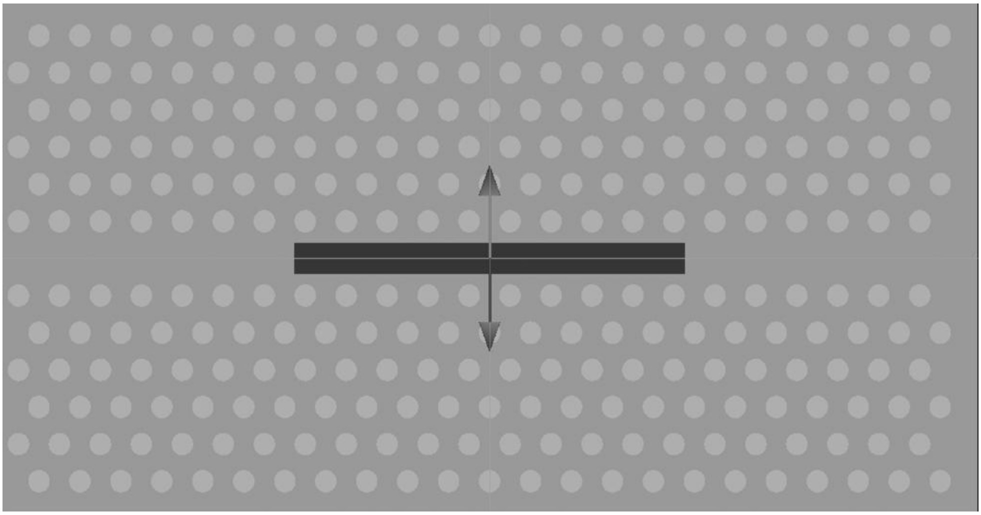

Figure 5.4: W1 photonic crystal cavity model. The arrow represents the TE polarized excitation source.

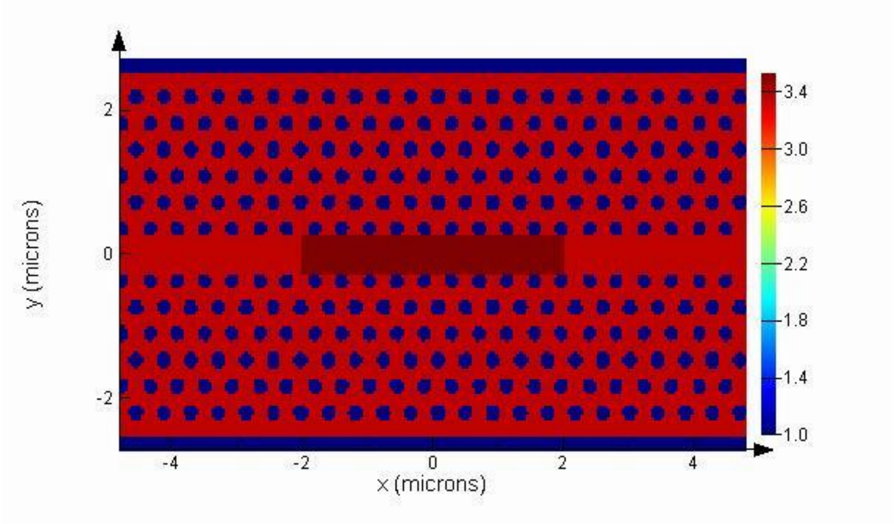

Figure 5.5: Refractive index map of the “W1” like photonic crystal cavity model.

5.4 Optical simulations for PhC Cavity

This section focuses on the optical simulations of the PhC cavity model. The simulations concentrate on optimizing the Q-factor as explained in Section 5.4.1. The optimization is divided into 3 parts. In Section 5.5.2, calculations for a simplified model are first started. Because this model can be used as a reference model to compare with when more physical factors are added later on. Next, in Section 5.5.3, an extended PhC model with more physical factors such as doping and oxidation included. Finally since fabrication is never perfect, the tolerance of the cavity to fabrication imperfections is checked and evaluated.

5.4.1 Quality factor

In physics and electrical engineering the quality factor (Q factor) is the most used parameter to describe the performance of a resonator. Higher Q indicates a lower rate of energy loss relative to the stored energy of the resonator. This means that the oscillations die out slower. Resonators with high quality factors have low damping so that they can ring longer [5.14].

The most common definition of the Q factor is shown in Fig. 5.6 and Eq. 5.12.

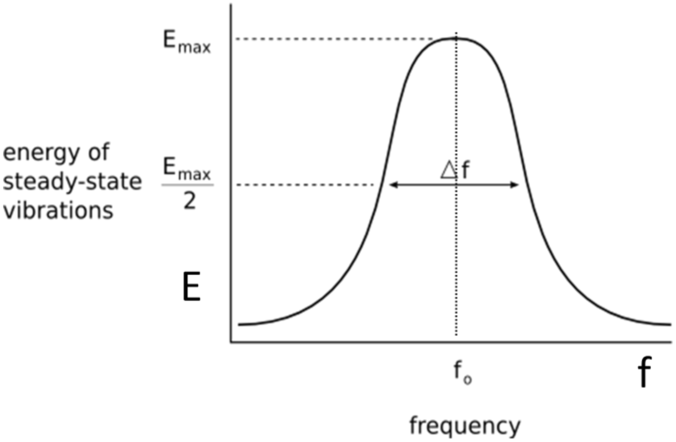

Figure 5.6: Definition of Q factor for a steady-state oscillation. Here f_o is the resonant frequency Δf is the FWHM of the resonance peak.

$$Q = f_0/\Delta f \tag{5.12}$$

For lasers, a high Q factor means lower damping which indicates lower optical loss and therefore less gain needed to lase. For electrically pumped devices, this means a smaller threshold current. Therefore in the PhC cavity modeling, the performance of the PhC cavity is mainly based on Q factor evaluation. In the next two sections, the cavity will be studied, first in a simplified model since it is convenient to start with. Next, a more realistic but complicated extended model will be simulated in order to check the influence of the physical factors such as doping, BCB bonding, etc. After that the effect of the obtained Q-factor for the electrically pumped lasers will be calculated.

5.4.2 Simplified 3-D model

Figure 5.7 shows the simplified 3D model of the PhC cavity. The whole membrane is assume to be a single un-doped Q (1.2) layer with a refractive index of 3.37 except for a small active region, which has a dimension (4*0.4*0.21 μm^3) and refractive index of 3.53 as shown previously in Fig 5.5. For the PhC cavity, the lattice constant a is 420 nm and the hole diameter d is 220 nm based on the band gap calculations. The membrane thickness is 210nm, which is consistent with the membrane thickness for passive devices shown in Chapter 2. Beneath the membrane layer is the BCB bonding layer with a refractive index of 1.5. A light source (TE polarized) is placed in the middle of the cavity to excite the field. Here it should be mentioned that the Si substrate is not included. There are two reasons for this. First, due to the high refractive index contrast of the IMOS platform, light is sufficiently confined in the thin membrane layer. Therefore with a thick BCB bonding layer (1 μm at least), it is found that there is almost no difference by adding the Si substrate into the model. Secondly, since 3-D FDTD simulation is known to be a memory and time consuming process, by removing the thick Si substrate, simulations can be performed much more efficiently and meanwhile still give valid results.

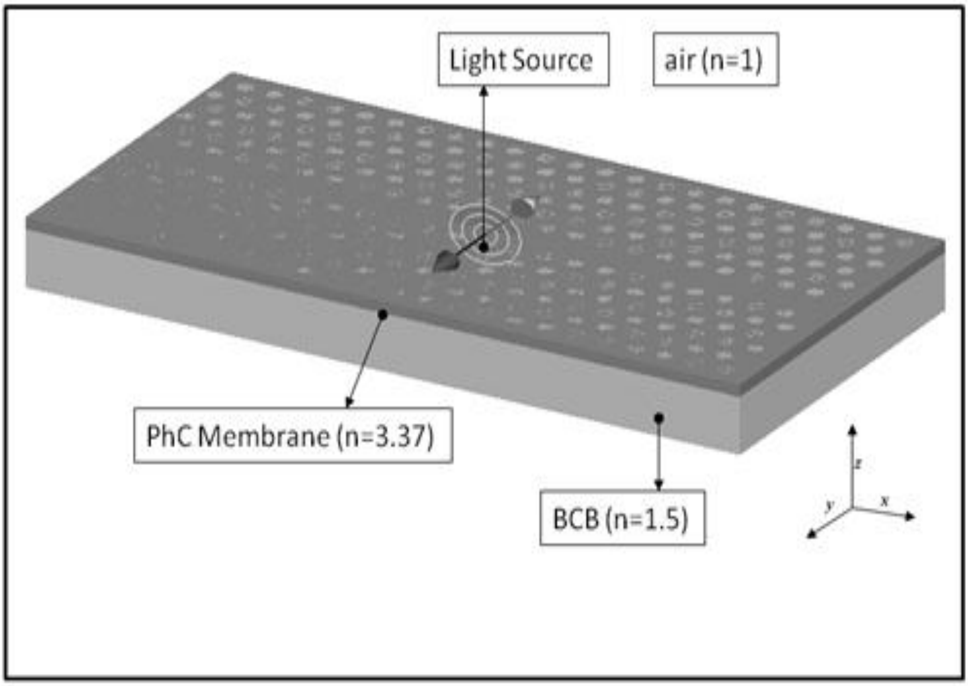

Figure 5.7: A schematic view of the simplified PhC model.

The main simulation results are shown in Figures 5.8 and 5.9. Fig. 5.8 shows the main resonant mode with a quality factor of 17000 at 190.3THz (corresponding to a wavelength of 1576 nm). To investigate more of the main resonant mode, the field profile is shown in Fig. 5.9. One can see that the mode has a symmetric profile and in the x-y plane the mode profile overlaps well with the active region. This will make the best use of the optical gain produced by the multiple QWs, which is crucial for laser emission.

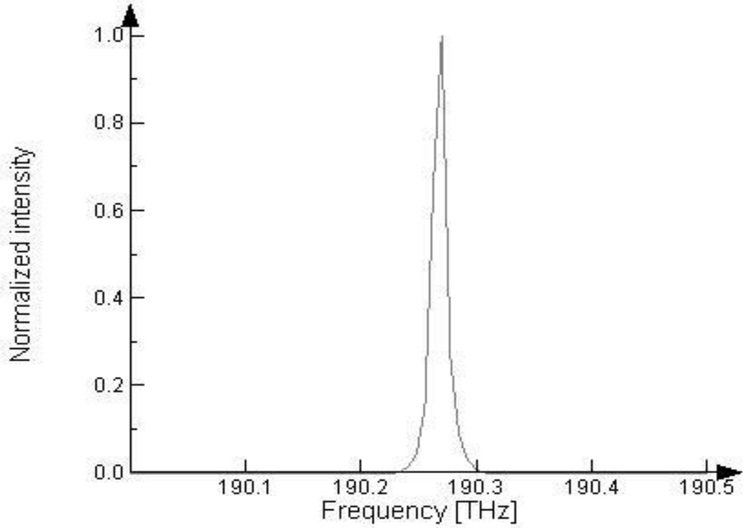

Figure 5.8: Resonant spectrum of the simplified model.

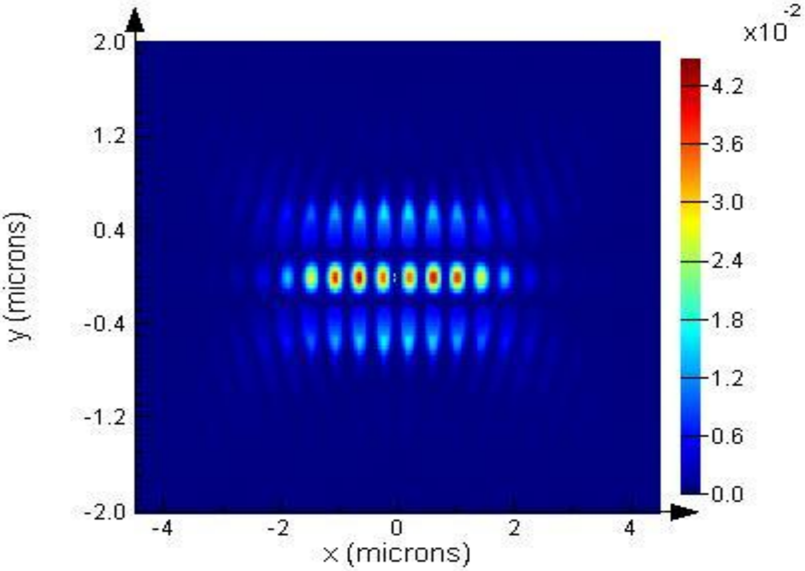

Figure 5.9: Mode field profile of the main resonant mode

5.4.3 Extended model

In the previous section, the simulations of a simplified PhC cavity model were shown. However, for an electrically pumped photonic crystal laser in IMOS, the real situation is more complex. A number of physical factors resulting from doping, AlInAs oxidation and BCB bonding, can influence the performance of the photonic crystal cavity. Therefore, in this section, we include these physical factors into the model and evaluate their impact on the performance of the photonic crystal cavity, especially the Q factor.

a) Real layer stack

In the simplified model, the whole membrane is assumed to be a single Q (1.2) layer. However, for active devices with electrical pumping, more layers are necessary, for instance the ***p*** and ***n*** doped layers for conducting the laser current. Moreover, in our case in order to obtain the current confinement functions, an extra layer of AlInAs oxide is also introduced. Therefore the real layer stack, as shown in table 5.1 is thicker and more complex.

Table 5.1 Real layer stack for electrically pumped photonic crystal laser

Layer number	Material	Thickness [nm]	Refractive index	Function
1	n-Q (1.2)	30	n=3.37	n-doped layer
2	n-InP	10	n=3.17	Etching stop layer
3	Q(1.2)	5	n=3.37	Barrier
4	4 InGaAsP QWs	61.5	n=3.53	Active layer
5	Q (1.2)	5	n=3.37	Barrier
6	AlInAs	100	n=3.2	For current confinement
6	AlInAs oxide	100	n=2.4	For current confinement
7	p-Q (1.2)	60	n=3.37	p-doped layer

The simulation result shows a Q factor of 914 (@ 1494 nm) is obtained. Compared with the simplified model, the Q factor is reduced a lot and the resonant mode is shifted to a shorter wavelength. This is mainly due to AlInAs oxidation. Because once AlInAs gets oxidized, the composition of the material also changes. Consequently, the refractive index changes as well. For the oxidation technique used in this thesis, the main oxides formed are Al_2O_3 and In_2O_3 [5.15], which both have a lower refractive (n=2.4) than AlInAs (n=3.2). Since the AlInAs layer is within the membrane, this decrease of refractive index will also decrease the effective index of the whole membrane. Therefore the vertical refractive index contrast of the whole membrane is reduced and with less vertical confinement, the quality factor of the PhC cavity decreases consequently. The lower effective index also explains the shift of the resonance to lower wavelengths.

b) BCB bonding

In the present process scheme for IMOS, the InP-based material wafer is first processed, after which the sample will be bonded on a Si wafer by BCB bonding. The problem for the photonic crystals is that during the bonding procedure the holes will be filled with BCB. Since BCB has a different refractive index (n=1.54) than air (n=1), it is necessary to check how the resonant mode responds to such a change. Moreover in order to increase the Q factor, an extra layer of BCB can be spun on top of the photonic crystal to make the refractive index profile of PhC membrane structure symmetric. In this way, the coupling from symmetric mode to anti-symmetric mode is less and it is expected that the Q factor can be increased furthermore. The simulation results are shown in Fig.5.10. The Q factor increases rapidly to 3507 and moreover the resonant wavelength λ_r shifts to1556nm.

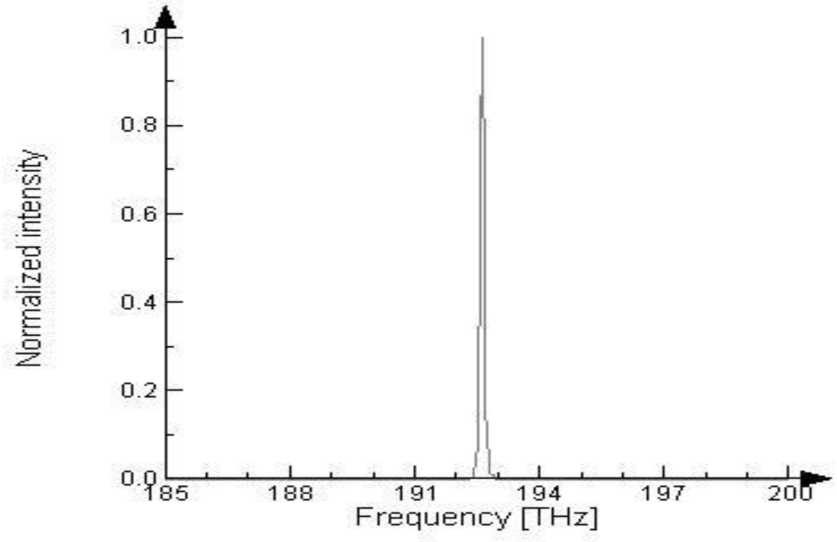

Figure 5.10: Resonance spectrum of extended PhC cavity model with BCB on both sides.

c) Doping

As is well known, doping, especially p-type, will cause optical loss. However, for electrically pumped opto-electronic devices doping is inevitable. Therefore the effect of doping on the resonant mode, especially the Q factor, needs to be investigated.

In the simulation, the effect of doping is implemented by including an imaginary part of the refractive index. The relation between optical loss α [dB/cm] and the imaginary part of refractive index n" is given by eq.5.13

$$n'' = \frac{\boldsymbol{\lambda_0}}{4\pi} * 0.0023\alpha \tag{5.13}$$

Where $\boldsymbol{\lambda_0}$ is the wavelength.

Absorption due to n-type doping, which is mainly caused by intra-band absorption of free carriers, is estimated by eq. 5.14 [5.16] for a wavelength of 1550 nm, with n the dopant concentration in [cm^{-3}]

$$\alpha_n = \frac{4.43 * 10^{-19} * n}{0.342 - 0.0172 \log n} \tag{5.14}$$

The loss due to p-type doping is higher than for n-type doping. The absorption for p-type material is given by eq.5.15, for a wavelength of 1550nm, with p the dopant concentration in [cm^{-3}]

$$\alpha_p = 9.9 * 10^{-17} p \tag{5.15}$$

The simulation result shows a corresponding Q factor of 2599 with the resonant wavelength λ_r at 1555 nm. The optical loss caused by doping decreases the quality factor by about 20%.

5.4.4 Tolerance check

Manufacturing errors are inevitable during the fabrication process. Therefore it is necessary to check whether the cavity is robust enough to tolerate the common manufacturing imperfections. Manufacturing errors can have various causes. For our case, two important types of manufacturing errors are considered: Active region misalignment and deviations in PhC key parameters such as lattice constant and hole size.

a) Active region misalignment

The first possible manufacturing error simulated is the misalignment of the active region with respect to the photonic crystal hole array. This type of fabrication error is possible, because during the fabrication process the active region and the PhC hole array are defined in separate EBL lithography steps. The active region is first defined for the active passive integration. Afterwards the photonic crystal hole array is defined (See Section 6.3). Although alignment markers are used, there is still a possibility that the active region is not perfectly located in the centre of the line defect photonic crystal waveguide. Therefore it is necessary to simulate whether the PhC cavity operation is robust against such misalignment. In the simulation, the active region is misaligned up to 100 nm with respect to the PhC hole array as shown in Fig. 5.11.

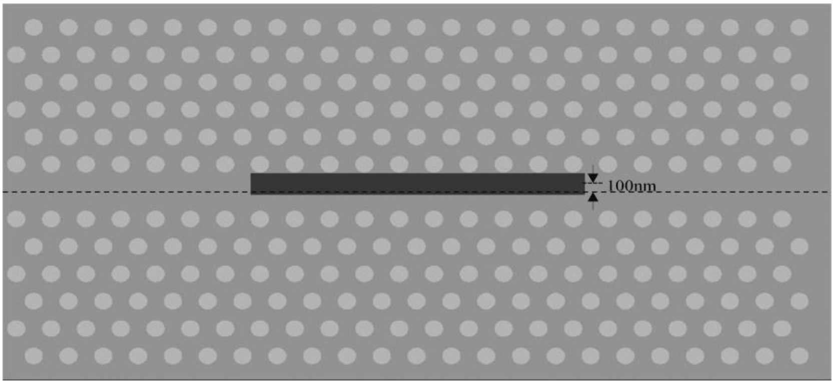

Figure 5.11: Misalignment of active region (100nm upwards)

The simulated resonance spectrum is shown in Fig. 5.12. The Q factor calculated for the “misaligned” cavity is 2623 @1555nm, presenting a drop of 25% with respect to the reference value (Q=3507@1556nm). This small decrease is still acceptable and moreover in the mask design, several types of cavity models will be designed to compensate such misalignment in advance (See Chapter 6).

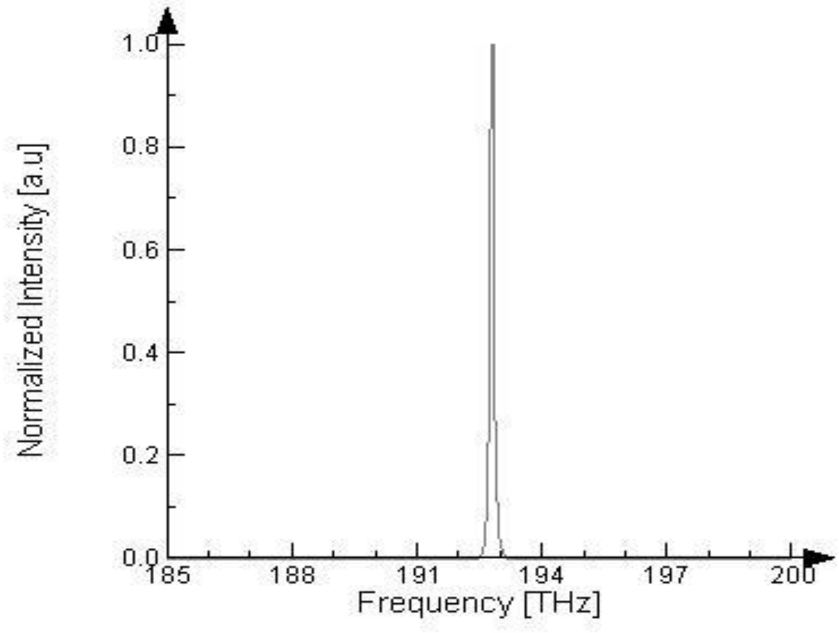

Figure 5.12: Resonant mode for misaligned PhC cavity (100nm upwards)

b) PhC Key parameters tolerance check

The second group of typical fabrication tolerance errors relate to one of the key parameters of photonic crystals: the PhC hole size. During the fabrication process, the PhC holes are defined and etched by various process such as EBL and RIE. We will check how the resonant mode, especially the Q factor and the resonance wavelength, will be influenced by the variation of hole radius of the PhC array.

Fig. 5.13 shows the result of a series of simulations based on the variation of the PhC hole radius. One can see that the resonant peak wavelength is shifting gradually to shorter wavelength as the hole radius increases. This is again because of the change in effective index of membrane, which decreases as the hole size increases.

Furthermore, one can see that the highest Q factor (Q=5074) is given by the radius ***r***=130nm. However the resonant wavelength in that case is around 1508nm, a bit shifted away from 1550nm,where the gain peak of the QWs centered. For the previous model, ***r***=110nm, the Q factor is a bit smaller (Q=3507), but the resonant wavelength is just around 1550 (λ_r=1556nm). Therefore based on these simulation results, in the final mask design, a group of radii (***r***=110nm,120nm,130nm) is chosen, which include both the highest Q factor, the best match with the QW-gain profile, and a compromise in between.

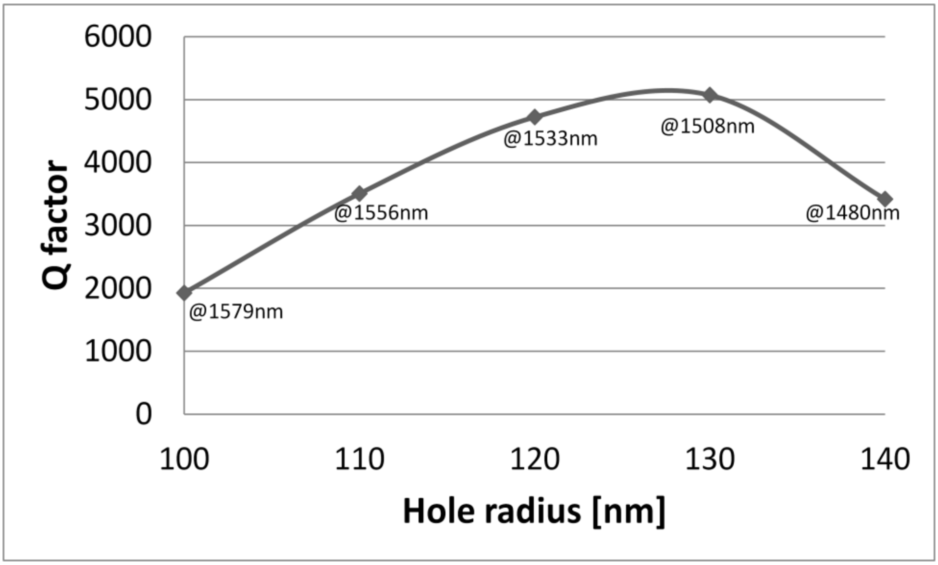

Figure 5.13: The relation between Q factor stability and PhC hole size

In this section, we have shown how the PhC cavity performance is influenced by the possible manufacturing imperfections. It can be seen that the designed photonic crystal cavity is sufficiently tolerant against these deviations. In the experiments a variation of key parameters of the PhC cavity, like PhC hole size is used in the final mask design to compensate for the possible critical dimension loss (CDL).

5.5 Gain from electrical pumping

In the previous sections, optical simulations of a W1 like photonic crystal cavity are presented, which show a good performance in terms of Q factor. However, since in our case an electrically pumped photonic crystal laser is pursued, electrical simulations[9] are also essential. They can predict the properties of the photonic crystal laser, like threshold gain and threshold current. Moreover, based on the band gap simulations of semiconductor material, we can evaluate how to effectively inject carriers into the active region.

5.5.1 Electric simulations

For the electric simulation, the software "Nextnano" is used. It is a simulator for calculating the realistic electronic structure of heterostructure quantum devices under bias. This software allows one to solve the Schrödinger-Poisson equation for arbitrarily shaped heterostructure device geometries [5.17].

a) Starting layer stack

The first layer stack is shown in Table 5.2. The active material consists of 4 InGaAsP QWs with emission around 1550 nm. The n-type doped material is n-InGaAsP (Q1.2) with n-InP as an etch stop layer used during the wet etching to form the overhang (See Chapter 3). The p- type contact layer consists of 60 nm p-Q1.2 and 100 nm highly doped p-InGaAs.

---

[9] These electrical simulations are done by dr. Dominik Heiss and the author thanks him for the help.

Table 5.2 First layer stack for the electrically pumped photonic crystal laser.

Layer number	Material	Thickness [nm]	Doping [cm^{-3}]	Function
1	n-InGaAsP(1.2)	30	n=5e18	n-doped layer
2	n-InP	10	n=5e18	Etching stop layer
3	InGaAsP(1.2)	5	n.i.d.	Barrier
4	4 InGaAsP QWs+3 InGaAsP(1.2)	61.5	n.i.d.	Active
5	InGaAsP(1.2)	5	n.i.d.	Barrier
6	p-InGaAsP 1.2	60	p=2e18	p-doped layer
7	p-InGaAs	100	p=2e19	for p-metallization

Next the current-gain relation is calculated. As one can see in Fig.5.14, the current density needed for decent gain levels is quite high. This is mostly due to electrons leaking out of the active region as seen in Fig.5.15. For lasers, this means there is a high level of leakage current, which will decrease the pumping efficiency.

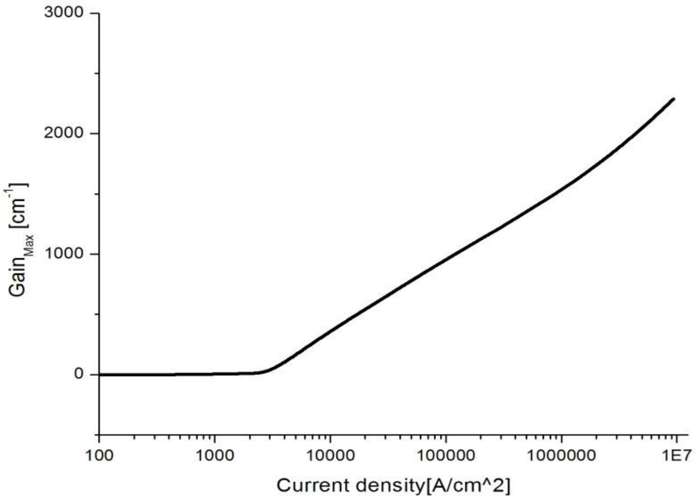

Figure 5.14: Max Gain vs Current density relation.

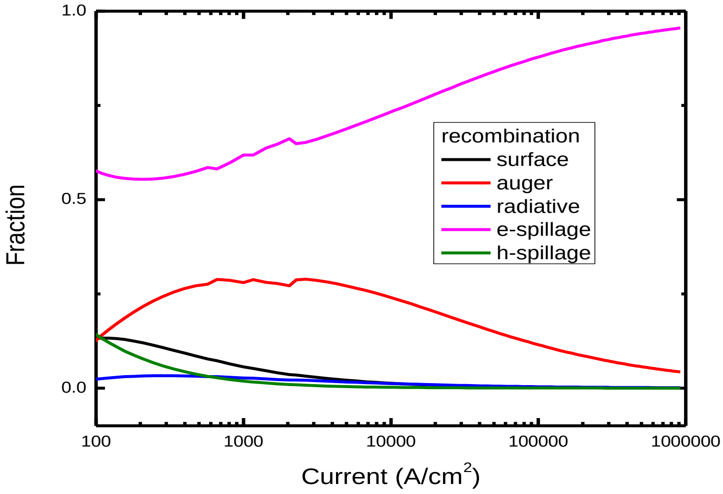

Figure 5.15: Different recombination process for the injected carriers.

b) The optimized layer stack

In order to reduce the number of electrons that are spilled out of the active region, a higher band gap material, for instance InP can be used in the cladding to build up a barrier. This makes it difficult for electrons to tunnel through. In this way, more electrons will be confined within the QWs. Table 5.5 shows an improved layer stack in which 20 nm of the p-doped Q(1.2) layer is replaced by p-InP.

Table 5.3 The improved layer stack, including an extra InP barrier

Layer number	Material	Thickness [nm]	Doping [cm^{-3}]	Function
1	n-InGaAsP(1.2)	30	n=5e18	n-doped layer
2	n-InP	10	n=5e18	Etching stop layer
3	InGaAsP(1.2)	5	n.i.d.	Barrier
4	4 InGaAsP QWs+3 InGaAsP(1.2) barrier layer	61.5=4 x 6 QWs +3x12.5 Q(1.2)	n.i.d.	Active
5	InGaAsP(1.2)	5	n.i.d.	Barrier
6	**p-InP**	**20**	**p=2e18**	**To reduce electron spillage**
7	p-InGaAsP (1.2)	45	p=2e18	p-doped layer
8	p-InGaAs	100	p=2e18	for p-metallization
9	p-InP	5	p=2e18	Cap layer

Fig.5.16 and Fig.5.17 shows the band structure of both layer stack under forward bias 1.5V. The red circle in Fig. 5.17 indicates the larger band gap introduced by the extra InP layer. The analysis results in Fig. 5.18 show the various recombination mechanisms for the injected carriers. Compared with Fig. 5.15, one can see that with the increase of the current density, the e-spillage, which are the number of electrons that spill out of the active region, are greatly reduced as the current increases. In this way, more electrons can be confined inside the active region (QWs) and contribute to the generation

of the optical gain. This is seen Fig.5.19, which compares current-gain relations of the two layer stacks. As one can see, the influence of reducing e-spillage is obvious. By introducing the 20nm high band gap material p-InP layer, a reduction of nearly 1 order of magnitude is obtained in current to achieve the same amount of gain. The influence of the layer stack's change to the laser performance will be shown and discussed in the next section.

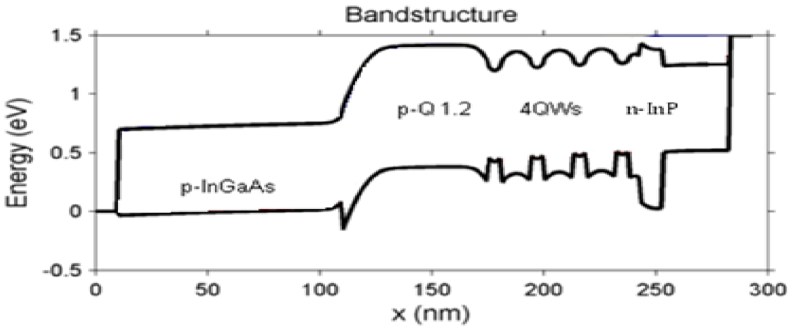

Figure 5.16: Band structure of the original layer stack under forward bias 1.5 V.

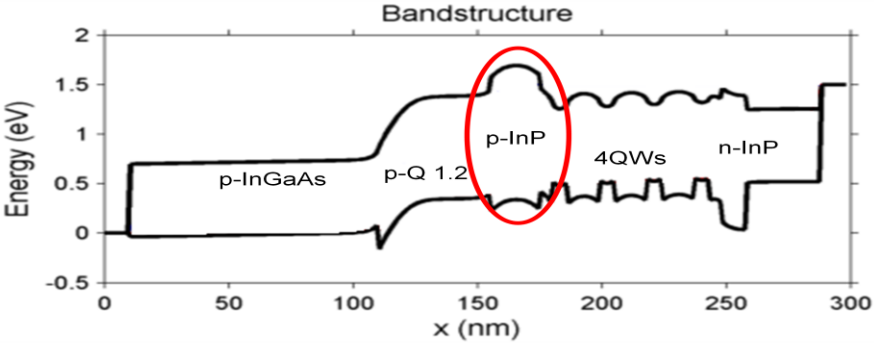

Figure 5.17: Band structure of the improved layer stack under forward bias 1.5 V.

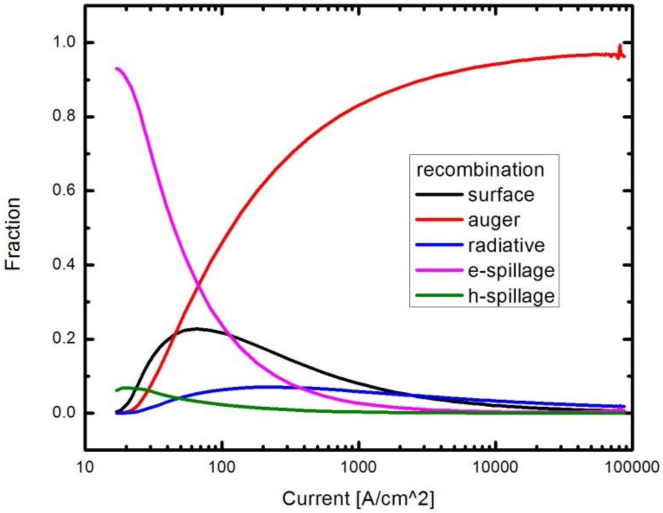

Figure 5.18: Carriers distribution of improved layer stack

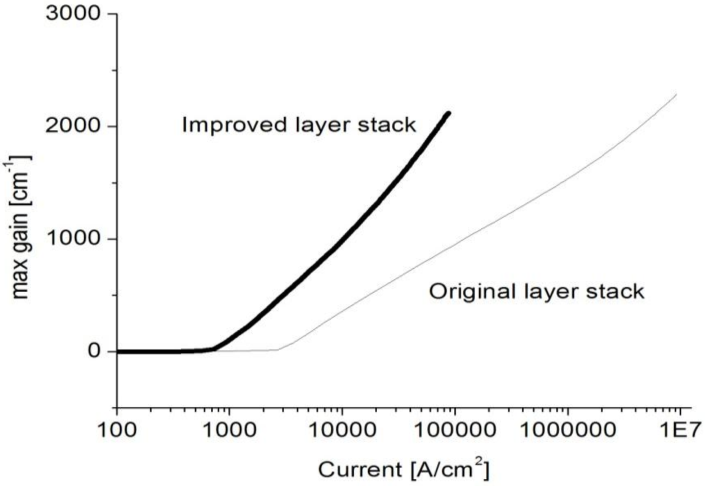

Figure 5.19: Comparison of current-gain relationship of the two layer stack.

5.5.2 Threshold gain and current calculation

In the previous section, it was shown that by introducing a 20nm high band gap material (InP) layer, a reduction of nearly one order of magnitude in current for the same gain can be obtained. However, to evaluate the properties of a laser simulation, the threshold gain and threshold current should be determined. Furthermore, since 20 nm of p-Q(1.2) is replaced by p-InP, it is necessary to check the influence of this change on the optical properties of the photonic crystal cavity. Therefore in this section, first we will start from the Q factors to calculate the threshold gain and threshold current of the designed photonic crystal cavity. Next, a comparison of the two layer stacks will be made to show quantitively how much improvement is obtained by using the optimized layer stack.

The relation between the Q factor and the threshold gain is given by Eq.5.16.

$$\Gamma v_g \, g_{th} = \frac{\omega}{Q} \tag{5.16}$$

Here Γ is the confinement factor, which is defined by the ratio of the light intensity of the lasing mode within the active region to the total intensity over the whole space [5.18]. v_g is the group velocity, g_{th} is the threshold gain, ω is the angular frequency. Since

$$v_g = \frac{\lambda f}{n_g} \tag{5.17}$$

and $\omega = 2\pi f$, then we can get the following expression for the threshold gain:

$$g_{th} = \frac{2\pi n_g}{\Gamma Q \lambda} \tag{5.18}$$

Here since the mode is mostly confined in the Q(1.2), in order to make an estimation of the required threshold gain and current, the refractive index (n=3.37) of Q(1.2) is used to represent group the index n_g. Then we can have a simplified expression for the threshold gain as shown by Eq.5.19.

$$g_{th} = \frac{2\pi n_{Q(1.2)}}{\Gamma Q \lambda} \tag{5.19}$$

Tables 5.4 show the calculated threshold gain and current based on Eq. 5.13. The results are given for the various photonic hole radii (R=130nm,120nm 110nm) used. As one can see, with the optimized layer stack, the estimated threshold current is reduced dramatically. This means that carriers can be injected into the active region in a much more efficient manner. The side effect is that the Q factor is reduced a little bit and the resonant peak wavelength also have a small blue shift. This is mainly due to the effective index change because of the replacement of 20nm higher index Q1.2 material by lower index InP material.

Table 5.4 Threshold gain and current calculate for R=110 nm, a= 420 nm

Model type	Q	λ_r [nm]	Γ	g_{th} [cm^{-1}]	I_{th}[mA)]
Original	2600	1555	5.19%	1009	1.56
Improved	2462	1548	5.38%	1033	0.13

5.6 Conclusion and discussions

In this chapter a “W1 like” photonic crystal cavity is designed and simulated both optically and electrically. In the first part, a simplified model with optical simulations shows that this cavity gives good performance in terms of quality factor and a good overlap between the resonant mode and active materials. Next, the effects from doping, AlInAs oxidation and BCB layers are implemented into the simulations. These factors do have a strong influence on the PhC cavity’s performance, especially on the Q factor and the resonant wavelength. Furthermore, since fabrication is never perfect, the effect of a number of errors is analyzed to check the PhC cavity's tolerance against manufacturing imperfections. Simulations show that this type of cavity is robust against common fabrication imperfections such as misalignment and CDL.

As a next step electrical simulation is performed. It is found that, an improved layer stack in which 20 nm of p-Q1.2 is replaced with p-InP gives a reduction of nearly an order of magnitude in current for the same amount of gain. Compared with the original layer stack, a much lower threshold current is required for the improved layer stack. This is due to the increased barrier height on the p-side of the cladding brought by the 20 nm p-InP. In this way more electrons can be confined inside the active region (QWs) and contribute to the generation of optical gain. And consequently the required threshold current is reduced dramatically. This makes it feasible to achieve an electrically pumped PhC laser in IMOS.

Chapter 6

Fabrication of a IMOS PhC Laser

In the previous chapter, the designed IMOS PhC cavity shows good performance in simulations. In this chapter, the fabrication of this first IMOS active device is described. Section 6.1 explains the considerations and principles for the mask design. Section 6.2 is the key part of this chapter which explains the fabrication process of the first IMOS active device. Finally the chapter finishes with conclusions and discussions in Section 6.3.

The realization of an electrically pumped membrane laser based on the selective area regrowth technique requires a complex fabrication process. As mentioned in Chapter 1, selective area regrowth provides freedom to the designer to optimize different materials for different functions. However, the downside of this approach is that multiple extra growth steps are required on processed surfaces. This makes it difficult to obtain a highly reproducible regrowth quality in each processing run and therefore it might cause a serious yield problem. The complete process takes at least 300 steps, including 3 regrowth steps and 10 E-beam lithography[10] steps. The most important and critical steps will be described in the following sections.

6.1 Mask design

Although the laser cavity has been designed in the previous Chapter, there are still many possible issues that should be considered before starting the fabrication process. This section will focus on these considerations and on the principles of the mask design. Due to practical limitations of the fabrication facilities, manufacturing imperfections are inevitable. To accommodate these, parameter variations will be included in the design to compensate in advance for these deviations.

For the laser fabrication, possible errors could result from misalignment and critical dimension loss (CDL). As CDL is known before hand, it can be compensated by width adjustment. Since 10 EBL steps are to be used for the lithography, many of which need a high alignment accuracy, E-beam alignment marks (See Fig.6.1) are used. Even though the alignment marks offer quite good alignment accuracy (a few tens of nanometers), some misalignment is still possible. Therefore a variation of some key parameters of the designed PhC is used, indicated in Table 6.1. It should be mentioned that the variation range of these PhC cavities are based on the PhC simulation in Chapter 5 (See Section 5.4.3). Table 6.2 shows the parameter

---

[10] The EBL is done together with Eric Jan Geluk and the author appreciate all his help.

set used for the different blocks of the mask layout. A few test structures, e.g PhC cavities without active region for measuring the loss of the photonic crystal waveguide, are also included. Moreover, since the realization of the electrically pumped PhC lasers is a challenging task, optically pumped PhC lasers are also included in the test structures. These can be used as a back-up solution in case the electrical pumping fails. The complete mask layer out is shown in Fig.2.

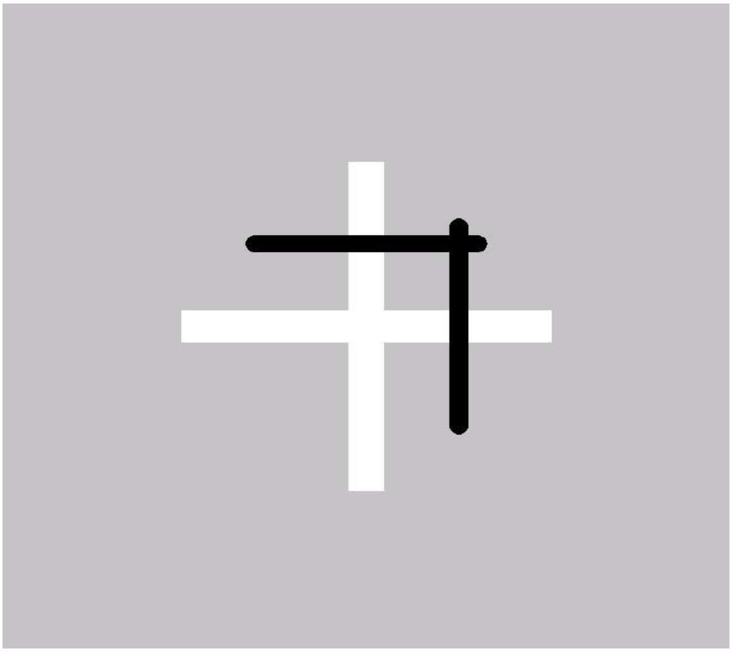

Figure 6.1: E-beam lithography alignment marker. The black lines are the automatic scans to locate the center of the marker [6.1].

Table 6.1 Variation of the PhC design parameters

(The bold style indicates the optimal values from the simulation)

Variables	Definition	Value [nm]
r	PhC Hole radii	$r \in [110, \mathbf{120}, \mathbf{130}, 140]$
a	PhC Lattice constant	$a \in [415, \mathbf{420}]$
w	Active region width	$w \in [200, \mathbf{300}, \mathbf{500}, 2000]$
O	Vertical compensation offset of the active region	$o \in [-100, -50, \mathbf{0}, 50, 100]$

The complete mask layer out is shown in Fig.2. Table 6.2 shows the parameter set used for the different blocks of the mask layout. A few test structures, e.g PhC cavities without active region for measuring the loss of the photonic crystal waveguide, are also included. Moreover, since the realization of the electrically pumped PhC lasers is a challenging task, optically pumped PhC lasers are also included in the test structures. These can be used as a back-up solution in case the electrical pumping fails.

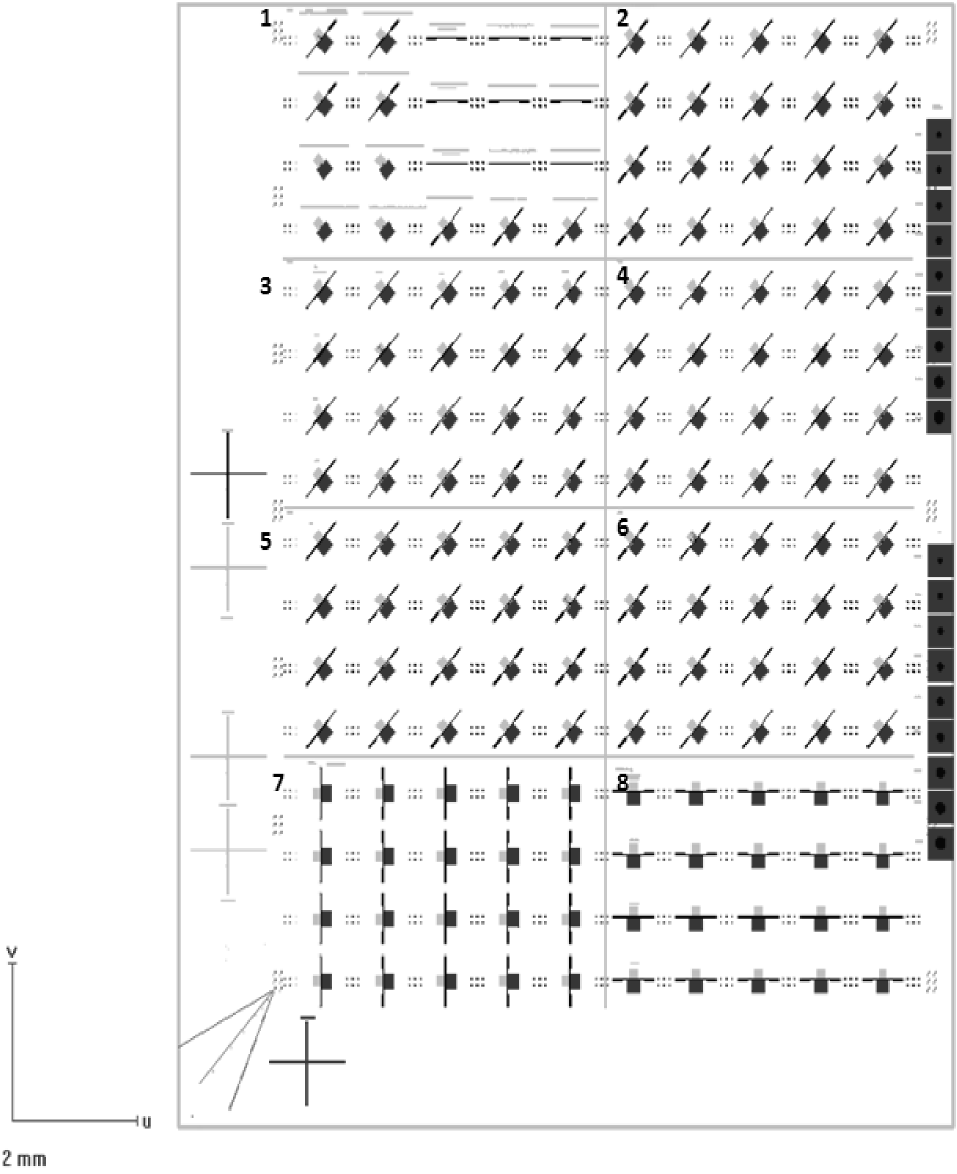

Figure 6.2: An overview of the mask layer out[11].

---

[11] The author thanks Dr. Yang Yang for his help in the mask design.

Table 6.2 Parameter for 8 blocks of the mask layer out

Block	r [nm]	a [nm]	Rotation	Other Features
1	140	415	45° &0 °	Test structures
2	140	420	45°	
3	130	415	45°	
4	130	420	45°	
5	120	415	45°	
6	120	420	45°	
7	110	415	90°	
8	110	420	0°	

6.2 Process description

In Chapter 2 the fabrication procedure of the IMOS passive components is described. The fabrication of the active devices is much more complex. Quite a few additional steps (lithography, etching, metallization) are required. In the following sections, we will explain the necessity, design and implementation of the critical steps. As mentioned in the previous section, the total process flow for making the electrically pumped PhC laser consists of more than 300 steps. Table 6.3 gives a overview of the critical fabrication steps.

First the starting material, the base wafer, will be introduced. Afterwards alignment marks will be defined in EBL-1 and later deeply etched. Next in EBL-2, using the alignment marks, the active region with QWs is defined and later etched as described in Chapter 3. Next, in the regrowth 1&2, respectively the regrowth of the passive material Q (1.25) and the AlInAs layer is done. After regrowth 1&2, the AlInAs-layer on top of the active region will be etched away in step EBL-3 with chemical wet etching (1HCL:4 H_3PO_4)). Finally the last three layers (p-InP, p-Q 1.2 and p-InGaAs) are regrown.

If the regrowth goes well, EBL-4 will be performed to remove the p-InGaAs-layer partially. This is done because this layer is only required in the parts where the p-metal contact will be, but it will cause high optical loss in the waveguide region. Afterwards, the photonic crystal cavity, the waveguides, the tapers and oxidation grooves will be defined in EBL-5 and realized with dry etching. After this dry etching step, the lateral oxidation of AlInAs will be performed to create an electrical isolation layer. EBL-6 is used for the grating coupler definition, which needs a different etching depth as compared to the photonic crystal cavity and the waveguides.

EBL-7 and the following metallization with a lift off process are used for p-metal contact formation (Ti: 60 nm, Pt: 75 nm, Au: 200 nm). Next the InP sample will be bonded on a Si wafer using a BCB bonding process*. After the BCB bonding, the InP substrate will be removed with selective wet etching (see Chapter 2). Then EBL-8 defines the n-metal contact, which is also realized with a lift off process. Since the sample is bonded upside down, the previously deposited p-contact is now on the bottom of the membrane. Therefore extra steps (EBL-9 and dry etching) are needed to open this p-contact. Finally EBL-10 defines a trench around the n-contact region which is dry etched by an InP RIE. This is done in order to prevent a short circuit between n-doped and p-doped part through the non-oxidized part of the AlInAs-layer.

Table 6.3 Overview of critical steps for the fabrication of an electrically pumped PhC laser on IMOS

Critical step	Function
EBL-1	Alignment marks definition
EBL-2	Active regions definition
Regrowth-1&2	Passive part (Q 1.25) and AlInAs
EBL-3	AlInAs removal on top of the active region
Regrowth-3,4&5	p-InP, p-Q 1.2 and p-InGaAs for p metallization
EBL-4	InGaAs removal except the p-metal contact part
EBL-5	Photonic crystal cavity and waveguide definition
AlInAs oxidation	Current confinement function
EBL-6	Grating coupler definition
EBL-7	p-contact metallization
BCB bonding	Sample bonded on Si wafer
EBL-8	n-contact metallization
EBL-9	Opening to the p-contact
EBL-10	n-trench formation to prevent short circuit

6.2.1 Base wafer

The base wafer contains the layer stack as shown in Fig.6.3. Four InGaAsP QWs are designed in order to provide a high optical gain. The layer stack is grown on an InP substrate. Two sacrificial layers (500nm InGaAs and 300nm InP) are used for selective removal of the InP substrate after the bonding step (see Section 2.2.1). On top of the sacrificial layers, 30 nm of n-type Q(1.25) is grown for the n-type metallization. The InGaAsP QWs, with Q(1.25) barrier layers are grown next. It should be mentioned that in between the QWs, also thin (6nm) Q(1.25) barrier layers are grown. The whole epitaxy is finished with an InP cap layer for protection.

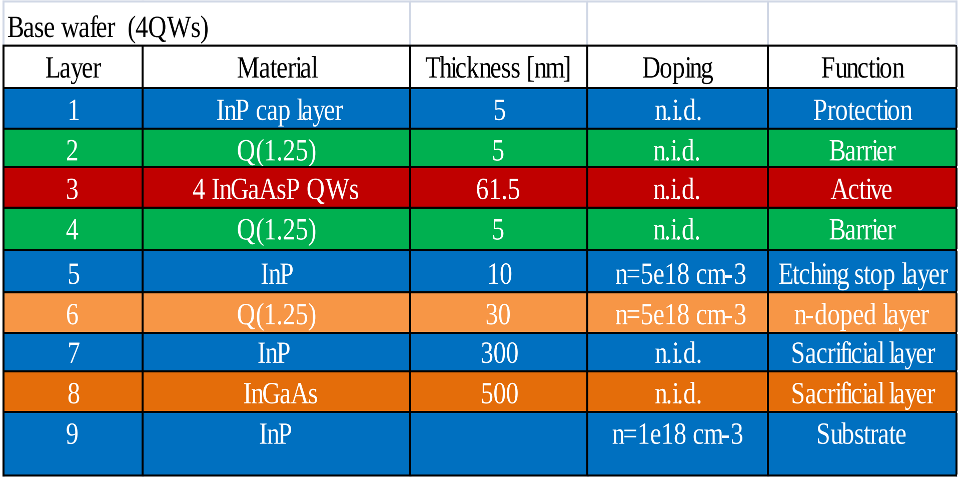

Base wafer (4QWs)				
Layer	Material	Thickness [nm]	Doping	Function
1	InP cap layer	5	n.i.d.	Protection
2	Q(1.25)	5	n.i.d.	Barrier
3	4 InGaAsP QWs	61.5	n.i.d.	Active
4	Q(1.25)	5	n.i.d.	Barrier
5	InP	10	n=5e18 cm-3	Etching stop layer
6	Q(1.25)	30	n=5e18 cm-3	n-doped layer
7	InP	300	n.i.d.	Sacrificial layer
8	InGaAs	500	n.i.d.	Sacrificial layer
9	InP		n=1e18 cm-3	Substrate

Figure 6.3: The base wafer layer stacks.

6.2.2 Alignment mark

The first EBL defines the alignment marks. These marks will be deeply etched by dry etching (RIE). The depth has to be at least 800nm to provide sufficient contrast in the EBL, so that they can be used for following EBL steps. Fig.6.4 shows a SEM picture of one of the alignment marks.

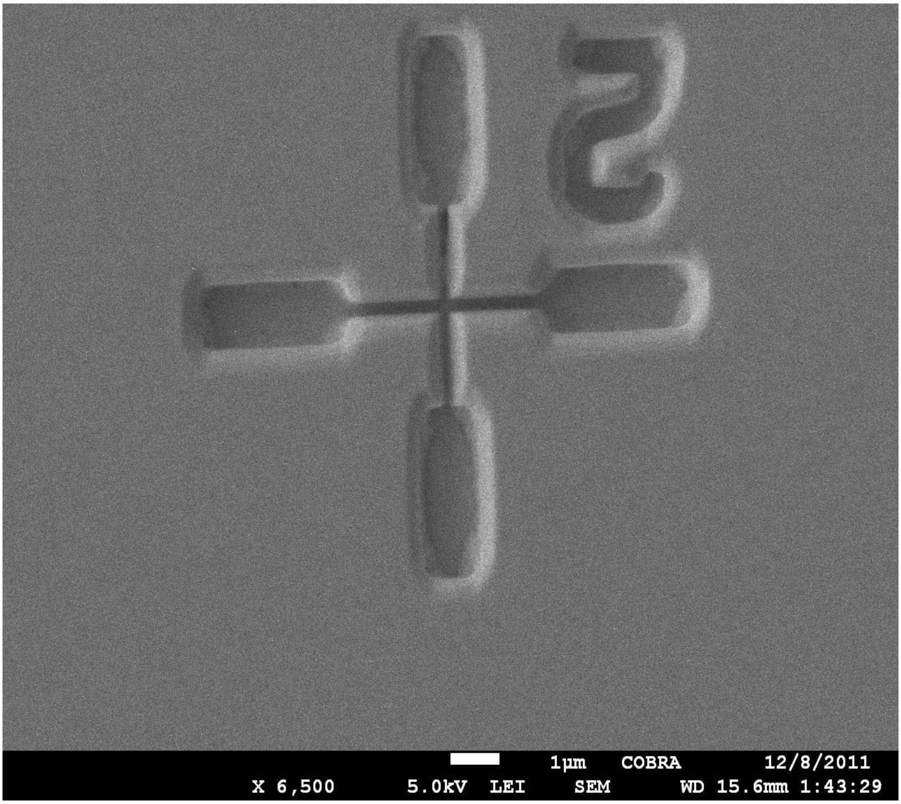

Figure 6.4: One of the etched alignment marks.

6.2.3 Active region definition and regrowth steps

In Chapter 3, sub-micron active-passive integration is already demonstrated. However, in order to make an electrically pumped active device on IMOS, extra regrowth[12] steps are required for the p-doped layer, the p-contact layer and the current blocking layer.

Fig.6.5 and Fig.6.6 give a detailed overview of the regrowth plan. The process flow for the regrowth of passive Q(1.25) material is shown in Fig.6.5. This is similar to the process described in Chapter 3. The only

---

[12] The regrowth is done in cooperation with Smartphotonics

difference is a smaller regrowth layer thickness (72 nm). The regrowth steps shown in Fig. 6.6 are new and include the additional regrowth steps for the p-doped layer, the contact layer and the current blocking layer. The AlInAs-layer will be firstly grown on top of the active/passive layers (Fig.6.6(a)). As described in Chapter 4, this layer will later be oxidized to function as a current blocking layer. Next, as indicated in Fig.6.6(b), the AlInAs-layer on top of the active region will be etched away. This is to avoid the current blocking inside the active region. Next the final three layers (p-InP, p-Q(1.2) and p-InGaAs) are regrown. The motivation for the design of these layers is given in Section 5.5.1. Further processing will then continue if the regrowth quality is good.

Elaborate tests were done first on the regrowth of the AlInAs-layer and of the p-doped layers on the partially etched AlInAs-layer. From this the most promising procedures and structures were obtained. The best results are achieved if the rectangular active region is placed under 45^o with the main crystal orientation (see Fig.1). The reason seems to be that in this orientation V-groove and dovetail shapes from the wet etching are avoided, and almost vertical sidewalls are obtained. This is apparently beneficial for subsequent regrowth steps.

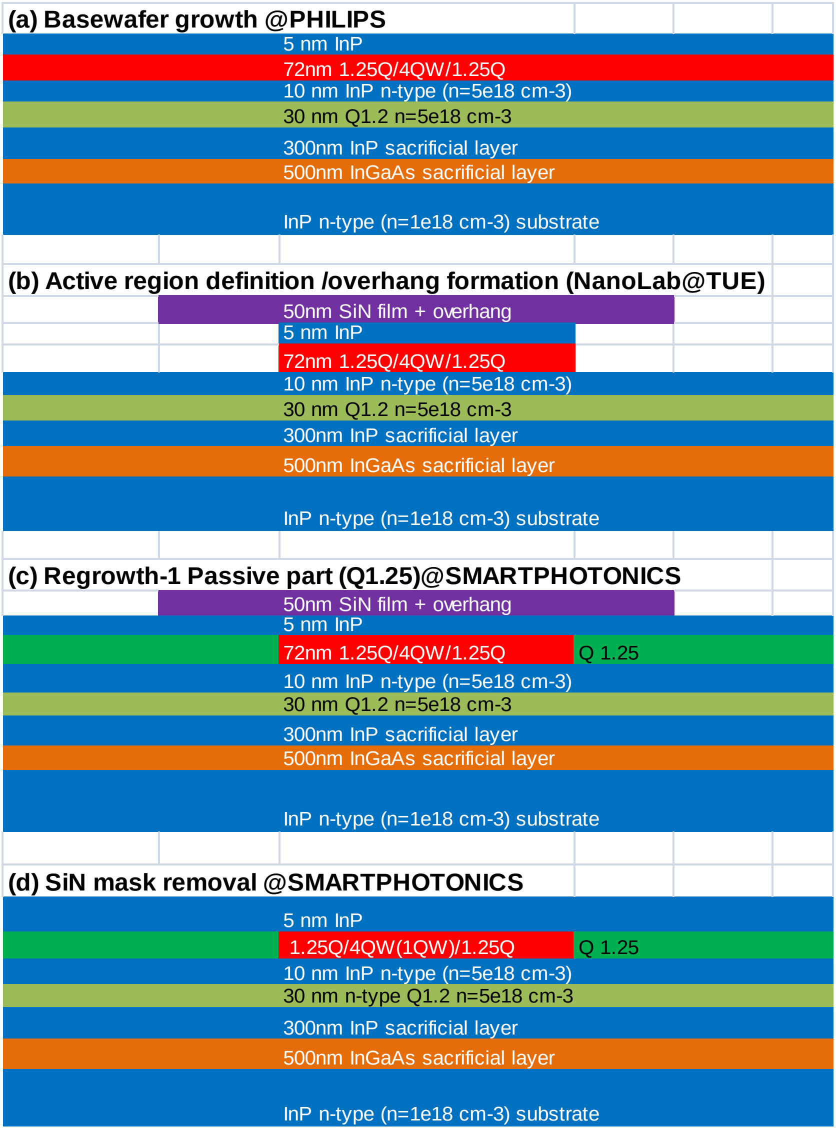

Figure 6.5: The definition of the active region and the regrowth of passive Q(1.25) material.

(a) Regrowth-2 AlInAs @SMARTPHOTONICS

	5 nm InP	
	100 nm AlInAs	
	5 nm InP	
	72nm 1.25Q/4QW/1.25Q	Q 1.25
	10 nm InP n-type (n=5e18 cm-3)	
	30 nm Q1.2 n=5e18 cm-3	
	300nm InP sacrificial layer	
	500nm InGaAs sacrificial layer	
	InP n-type (n=1e18 cm-3) substrate	

(b) Each away AlInAs in the active region (NanoLab@TUE)

5 nm InP		
100 nm AlInAs		
5 nm InP		
	1.25Q/4QW(1QW)/1.25Q	Q 1.25
	10 nm InP n-type (n=5e18 cm-3)	
	30 nm Q1.2 n=5e18 cm-3	
	300nm InP sacrificial layer	
	500nm InGaAs sacrificial layer	
	InP n-type (n=1e18 cm-3) substrate	

(c) Regrowth-3 p-InP/p-1.2Q/p-InGaAs/@SMARTPHOTONICS

5nm InP cap		
100nm p-InGaAs p=2e19 cm-3	5nm InP cap	
40 nm Q1.2 (p=2e18 cm-3)	100nm p-InGaAs	
20 nm p- InP(2e18 cm-3)	40nm Q1.2 p=2e18 cm-3	
100 nm AlInAs	20 nm p-InP(2e18 cm-3)	
5 nm InP		
	72nm 1.25Q/4QW/1.25Q	Q 1.25
	10 nm InP n-type (n=5e18 cm-3)	
	30 nm Q1.2 n=5e18 cm-3	
	300nm InP sacrificial layer	
	500nm InGaAs sacrificial layer	
	InP n-type (n=e18 cm-3) substrate	

Figure 6.6: The regrowth of the AlInAs, p-InP, p-Q(1.25) and p-InGaAs layers. It should be mentioned in these 2-D Excel tables the p-doped layer in the active region and the passive region seems to be disconnected. In reality, of course they are connected.

Fig. 6.7 shows a sample with a good regrowth quality after the first two regrowth steps (Q(1.25) for the passive layer and AlInAs for current blocking). There are still some defects (see Fig.6.7), in general the surface quality is acceptable.

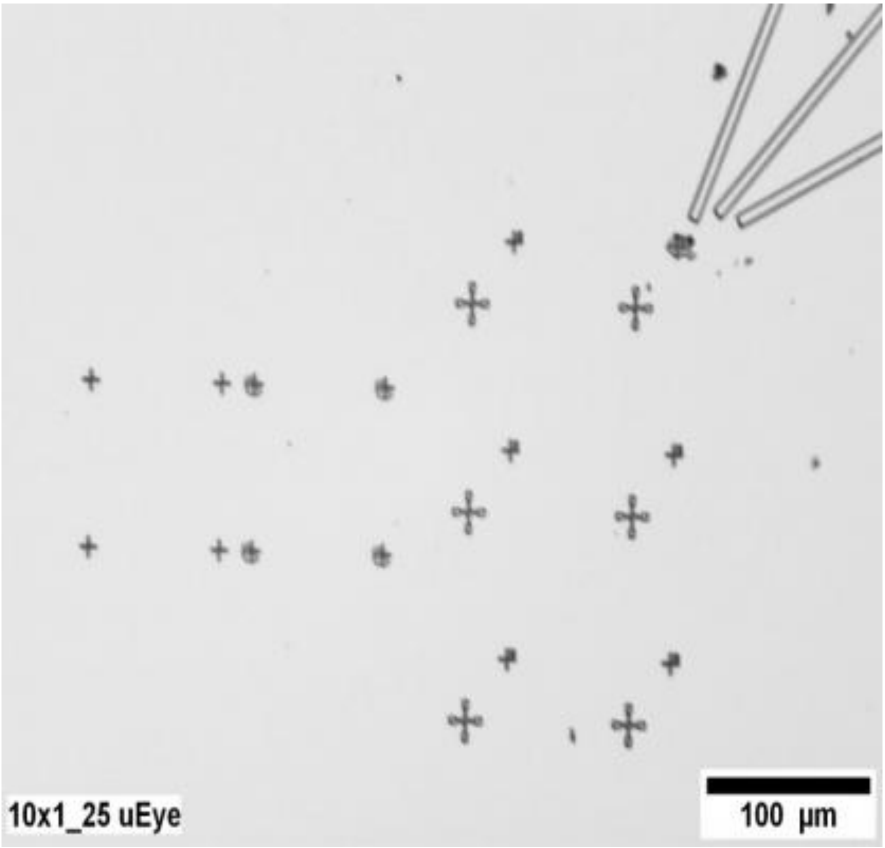

Figure 6.7: Microscope pictures of the sample surface after the regrowth of Q(1.25) and AlInAs. Alignment marks are clearly visible. The defect density is low

After the regrowth 1&2, the AlInAs-layer on top of the active region will be etched away with chemical wet etching (1 HCL: 4 H_3PO_4) as explained in the previous section. Next the sample will undergo the final regrowth step to obtain the p-InP, p-Q(1.25) and p- InGaAs layers. It is found out that after this final regrowth the upper part of the sample (60%) is good (see Fig.6.8). However, for the lower part of the sample (40%), there are much more defects and the surface quality is worse (see Fig.6.9). The bad part of the sample will be cleave off and used as test samples for the rest of the process.

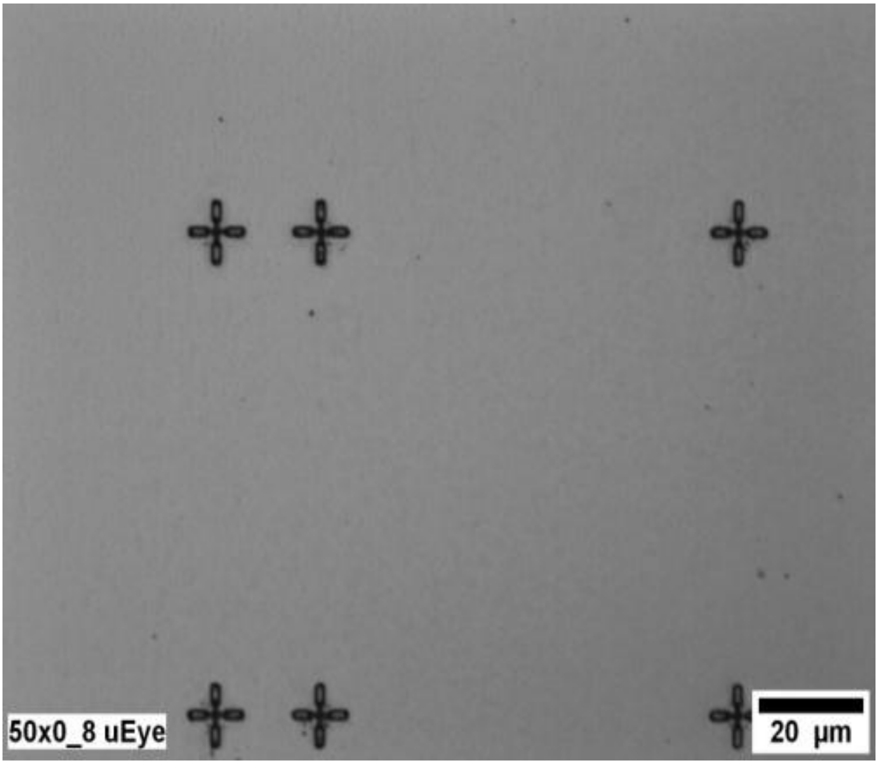

Figure 6.8: Microscope pictures of upper part of the sample after the regrowth of p-InP, p-Q 1.2 and p-InGaAs.

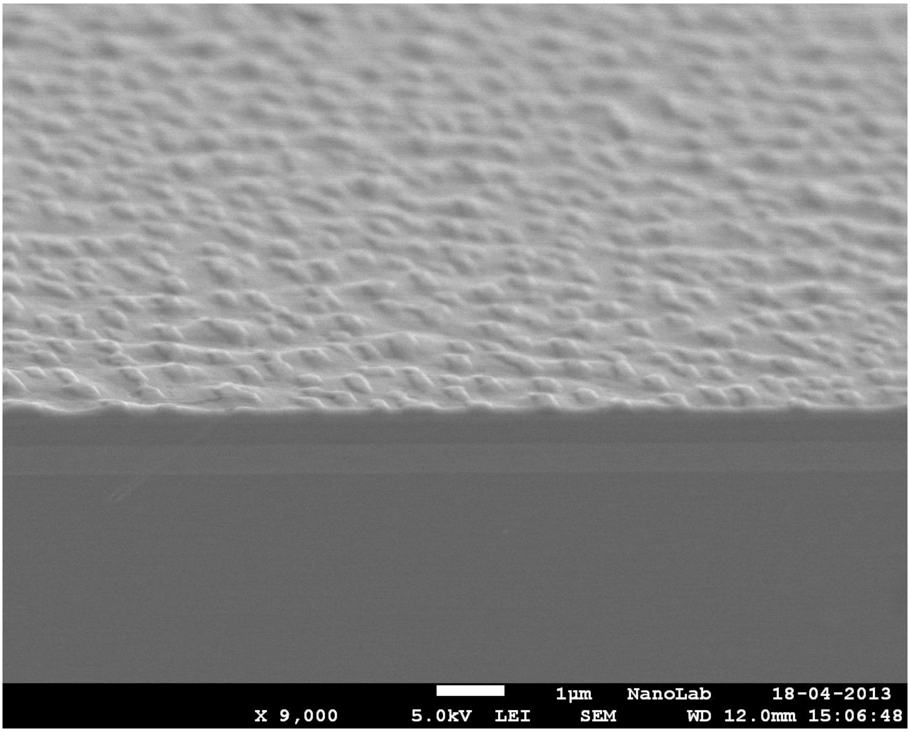

Figure 6.9: SEM picture of bad regrowth part of the sample after the regrowth of p-InP, p-Q 1.2 and p-InGaAs.

6.2.4 InGaAs etching

After all the regrowths, an etching process will be performed to partially remove the p-InGaAs layer. After Si_xN_y deposition and EBL lithography, the EBL resist (ZEP) pattern is developed (See Fig.6.10). Next Cr lift off is used to obtain the etching mask for the Si_xN_y. Finally, a dry etching process (RIE) of 1 cycle (2 minutes) is used to etch away the unmasked parts of the 100 nm InGaAs layer. Fig.6.11 shows the measured etching depth profile. One can see that the bottom surface is a bit rough, this is because the markers for the etching depth measurement is located at the bad regrowth part of the sample(see Fig. 6.9)

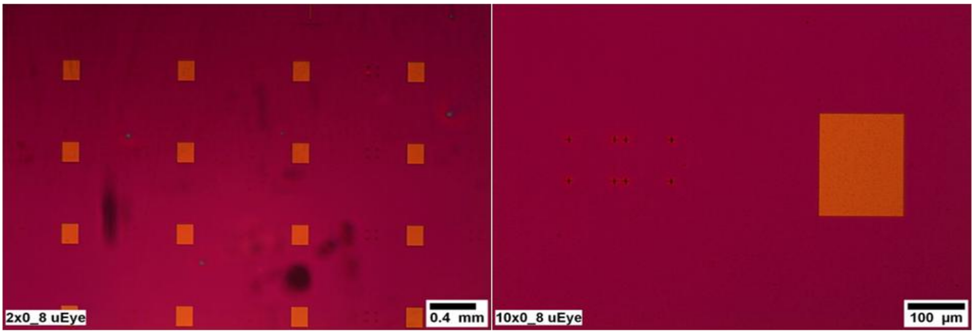

Figure 6.10: Microscope pictures of InGaAs pattern after the development of ZEP. a)Overview. b)Zoomed in picture with InGaAs on the right and alignment marks on the left.

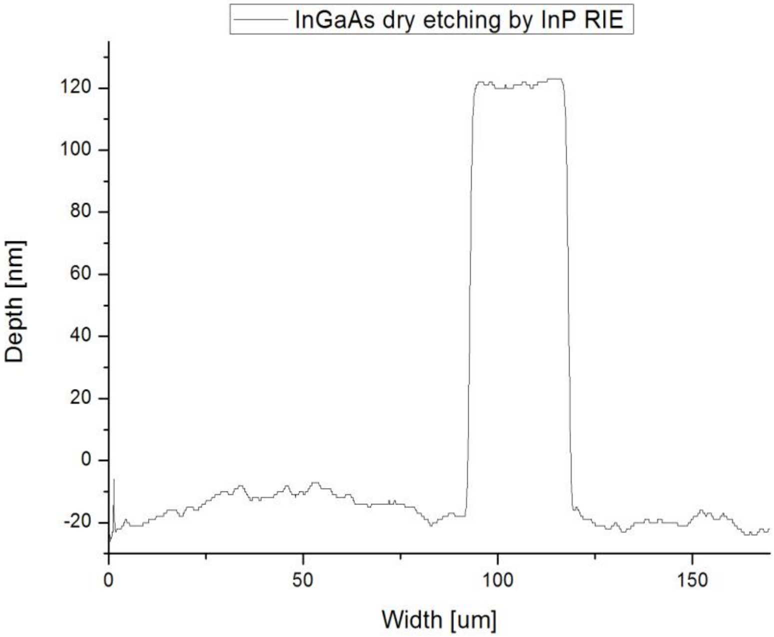

Figure 6.11: Measured etching depth profile. The etching depth is 100 nm after correction for 40nm of Si_xN_y on top.

6.2.5 Formation of PhC and oxidation trenches

After the InGaAs layers are partially removed, a series of critical process steps will be performed. These steps include the definition and formation of PhC holes, output waveguides and tapers, as well as oxidation trenches. The PhC holes and the output waveguides are used to form the laser cavity and to couple light out of the laser cavity. The oxidation trenches are formed to prevent short circuits between n and p contacts as shown in Fig.6.12. Without these oxidation trenches the un-oxidized AlInAs beneath the metal contact would allow a strong leakage current between the p and n sides of the membrane.

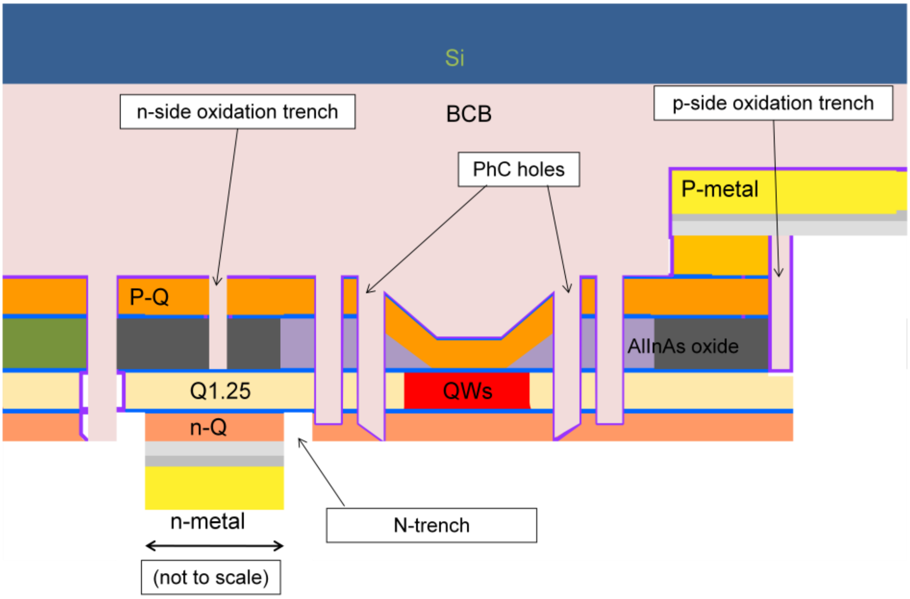

Figure 6.12: A schematic figure of the finally realized laser.

Fig.6.13 and Fig.6.14 are showing the realized structure after Si_xN_y etching and resist removal. They include PhC holes, the output waveguide, the tapers and the oxidation trenches.

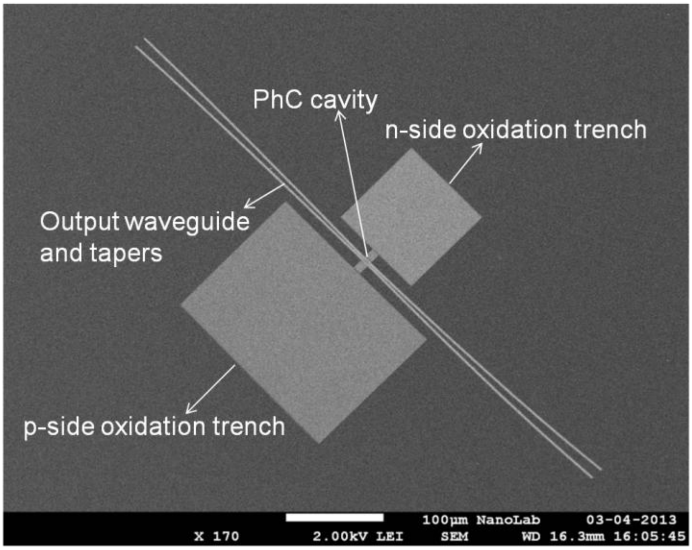

Figure 6.13: SEM picture with an overview of one device after the definition of PhC holes, output waveguides, tapers and oxidation trenches.

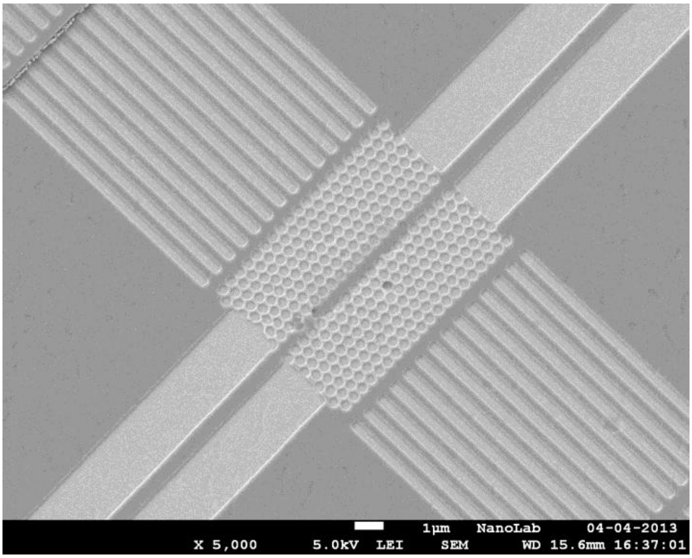

Figure 6.14: Zoomed in SEM picture of one device after the definition of PhC holes, output waveguides, tapers and oxidation trenches.

After the pattern definition, a dry etching process (RIE) of 4 cycles (8 minutes) is used to etch PhC holes, output waveguides and oxidation trenches. Figures 6.15 and 6.16 show the etched profile and the etching depth. These cross section pictures are taken from the bad regrowth part. The etching depth of the tapers and the oxidation trenches are different because of the lag effect of the RIE etching, which basically means the smaller the opening in the etching mask, the slower the etching will be. Here it should be mentioned that the actual etching rate of dry etching is much faster than expected (based on previous tests), which is the first indication that some layers could be missing. In the next section we will explore this further.

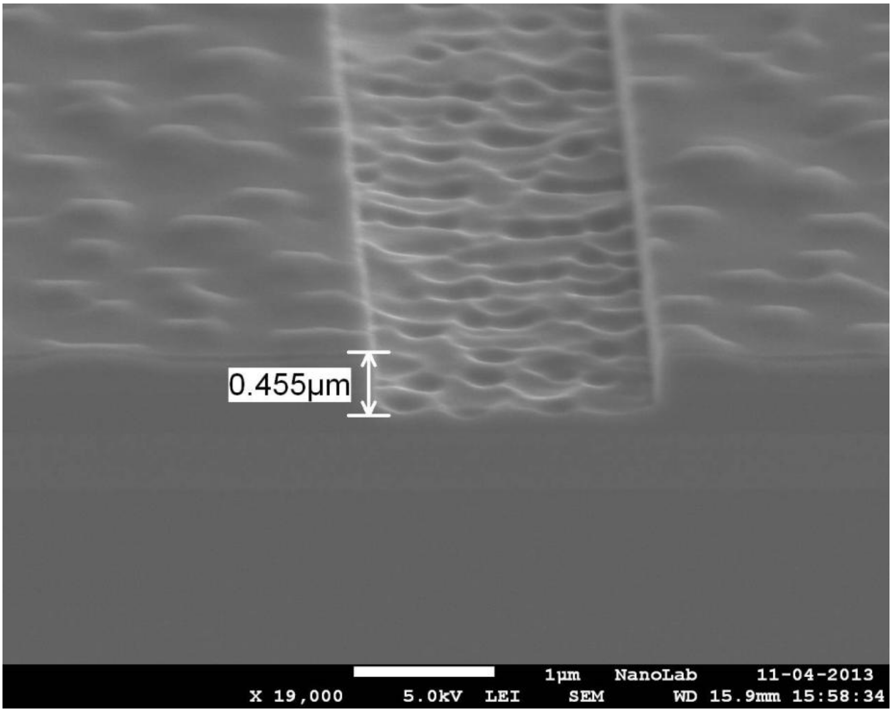

Figure 6.15: Dry etching of the tapers with etching depth.

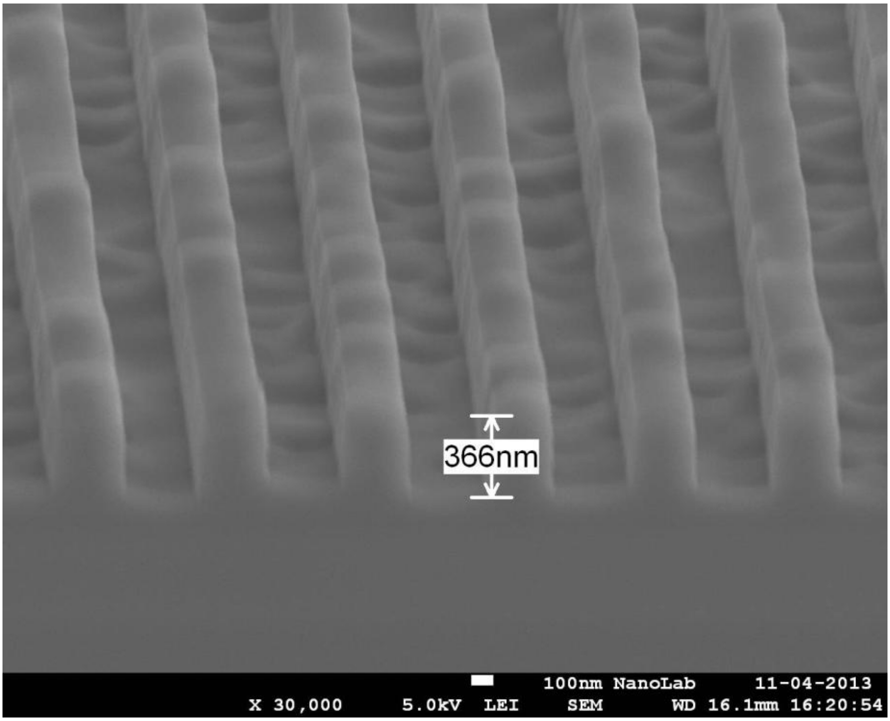

Figure 6.16: Dry etching of the oxidation trench with etching depth.

6.2.6 AlInAs oxidation

After the PhC holes and the oxidation trenches are etched, lateral oxidation will be performed in order to form the current blocking layer (see Chapter 4). Since the required oxidation depth is relatively small (between 200-300 nm), the oxidation time (@500 ^{o}C) is relatively short (20 mins). A front runner (test sample) is cleaved from the bad part of the sample and is oxidized first. However, as Fig.6.17 shown no oxidation of AlInAs, which should show up as a dark line through the ridges (see Chapter 4), is observed.

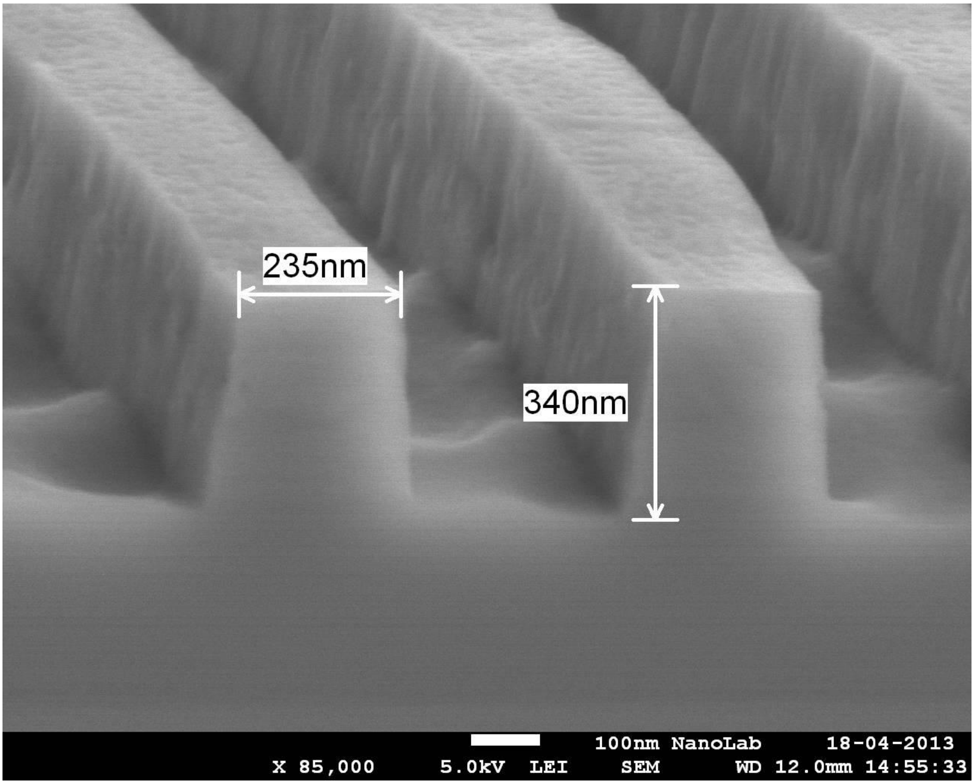

Figure 6.17: Trenches after oxidation. This picture is taken from the test sample cleaved from the bad regrowth part of the real sample.

In order to exclude the possibility that the missing oxidation is due to the bad regrowth quality, a second test is done with a sample cleaved from the good regrowth part of the sample (See Fig.6.18). The oxidation conditions are the same as before (500 ^{o}C for 20 mins). However, still no oxidation of AlInAs is observed.

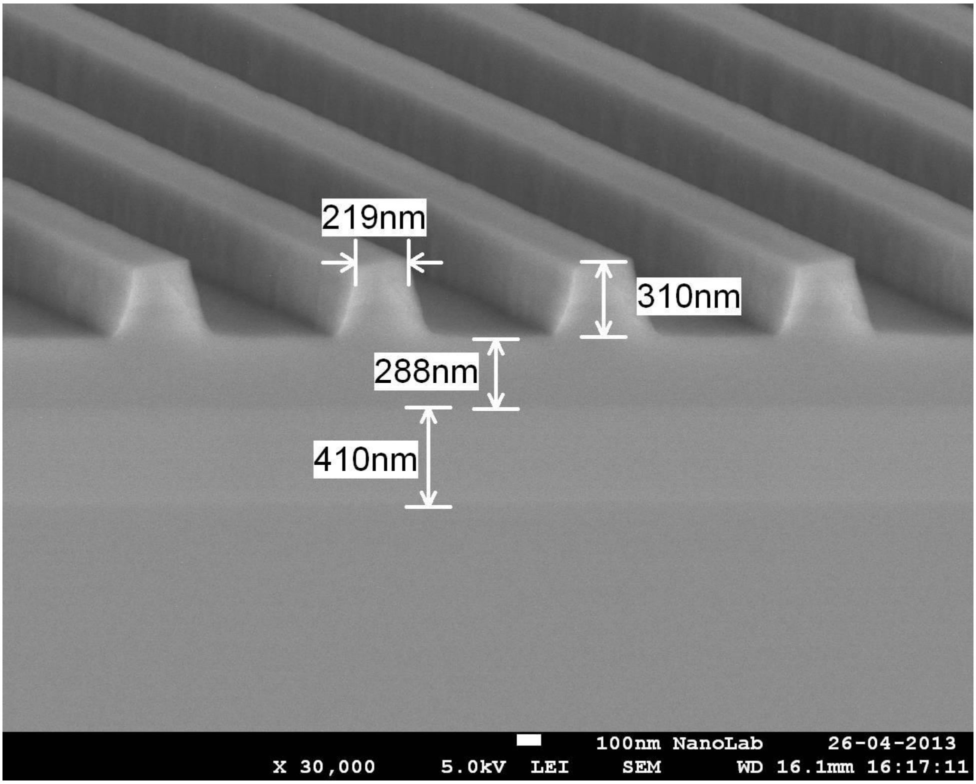

Figure 6.18: Trenches after oxidation. This SEM picture is taken from the 2nd test sample cleaved from the good regrown part of the sample.

In order to detect if the aluminum containing layer is still present, an Energy-Dispersive X-ray Spectroscopy (EDS)[13] analysis is done in SEM. EDS is an analytical technique used for elemental analysis of a sample. It relies on the investigation of the interaction of X-ray excitation with the sample. Its characterization capabilities are based on the principle that each element has a unique atomic structure, resulting in a unique set of peaks on the scattered X-ray spectrum [6.2]. First, in order to make sure that the EDS in our SEM is able to detect aluminum, a previously oxidized sample with

---

[13] The EDS is done together with Eric Jan Geluk and the author thanks him for the help.

AlInAs is checked. Fig.6.19 shows this oxidized AlInAs sample. The dark region shows the oxidized AlInAs-layer of this sample. One can see that the focus of the SEM picture is not good. This is because EDS has to be performed at a working distance of 8 mm, which is different from the normal working distance of the SEM (15 mm). The EDS spectrum is shown in Fig.6.20. The peak (around 1.5 keV) representing aluminum is clearly visible.

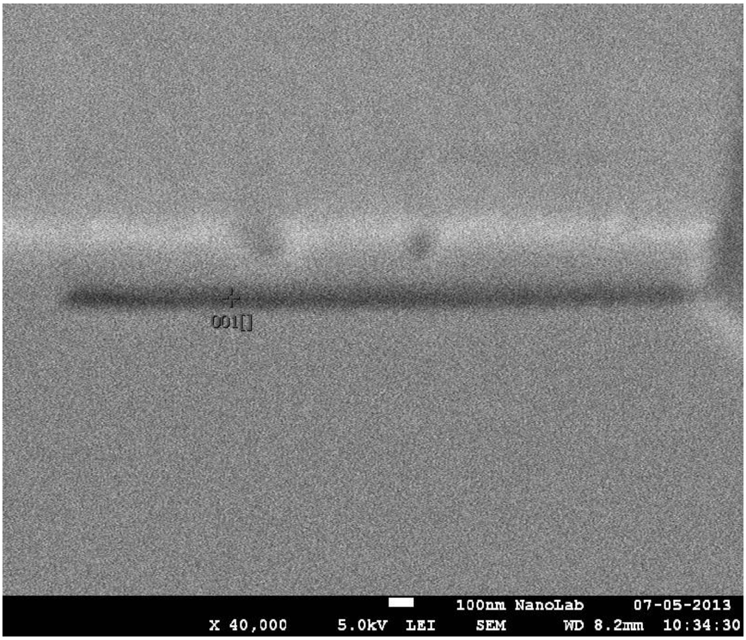

Figure 6.19: An SEM of picture of AlInAs oxidation sample for EDS. Point 001 shows where the EDS analysis is performed. The focus of the SEM picture is not good. This is because EDS has to be performed at a working distance of 8 mm, which is different from the normal working distance of the SEM (15 mm).

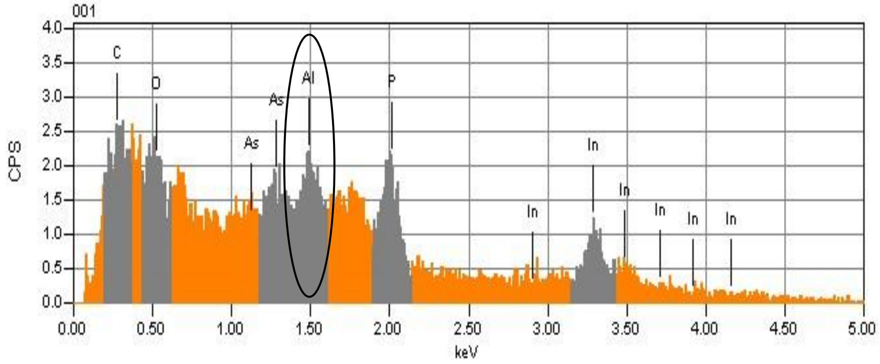

Figure 6.20: EDS spectrum from the oxidized AlInAs. Within the circle is the peak representing aluminum.

Therefore the EDS analysis is sensitive enough to detect aluminum in the AlInAs layer. The same analysis is then performed for the present sample. However, as shown in Fig. 6.21 and Fig.6.22, no aluminum is detected either from the taper or from the oxidation trenches.

From the log files kept on the epitaxial growth it is clear that the AlInAs-layer was originally grown. It appears that AlInAs is attacked and etched away with an HF solution during the hard mask removal process. In our process HF is used to remove the Si_xN_y hard mask. This doesn’t attack the common semiconductor materials used, such as InP, InGaAs and InGaAsP. However, according to the literature, AlInAs can be attacked by HF [6.3]. In our process, the AlInAs-layer is protected by a 5 nm InP cap layer. This cap layer was apparently accidentally removed during cleaning steps. Therefore the AlInAs- layer was exposed and is unintentionally removed with HF before the final regrowth.

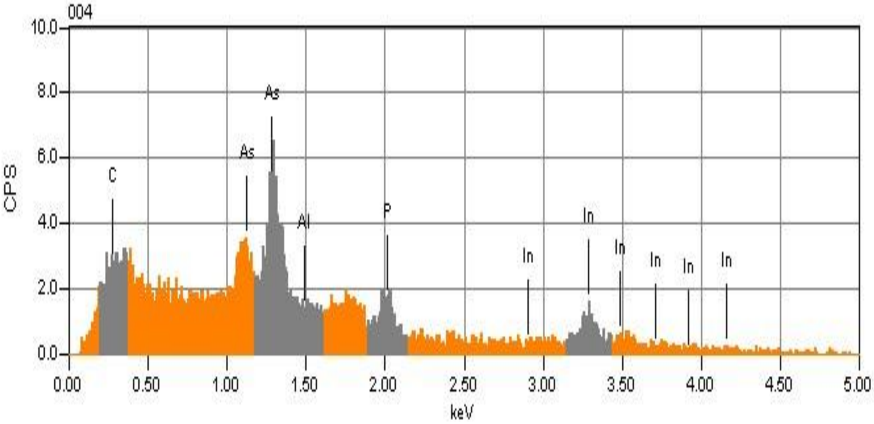

Figure 6.21: EDS spectrum of the taper of the laser sample.

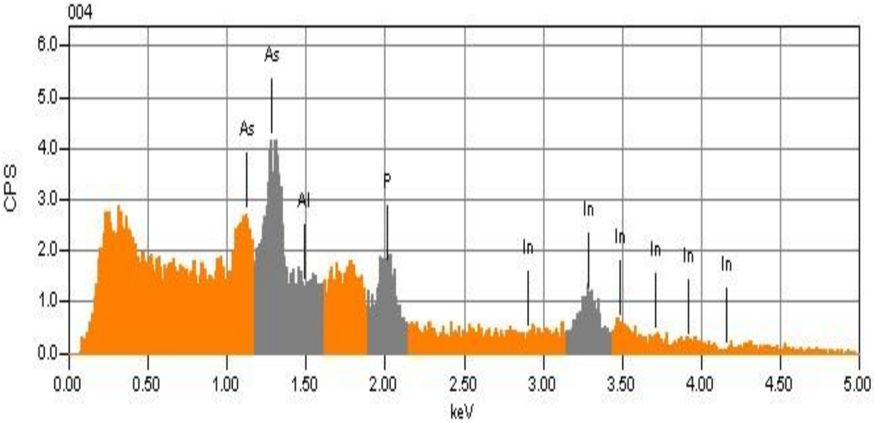

Figure 6.22: EDS spectrum of oxidation trench of the laser sample.

Without an oxidized AlInAs layer for the current blocking, an electrically pumped PhC laser is no longer possible, because in the membrane geometry short-circuiting will occur. It is however still possible to make an optically pumped PhC laser. This requires optimized grating couplers, which will be presented in the next section.

6.2.7 Grating definition.

The design and working principle of the grating coupler have already been explained (See section 2.3.1). However, for optical pumping of the lasers two types of grating are required: one to inject light from a 1300 nm laser into the cavity, in order to create gain, and one to couple 1550 nm laser light from the circuit into an optical fiber. For the pumping light, the grating is designed for optimal coupling of the wavelength of 1320 nm. This grating has a period of 500 nm and a filling factor 50%. The output grating is designed optimally for a wavelength of 1550 nm, with a period of 610nm and a filling factor 50%. Due to the missing AlInAs-layer the original grating designs could not be used anymore. It is found however that this can be corrected by leaving part of the last InP sacrificial layer in place. Fig.6.23 shows the simulation of grating couplers for both 1320 nm and 1550 nm as a variation of the remaining thickness of the InP sacrificial layer.

Since the grating parameters need to be controlled within the nanometer range, E-Beam lithography is used to define them. In order to get the right dimension, a dose test is applied to find the right dose. Fig.6.24 shows a grating made with the optimal dose factor. After the EBL, the gratings are formed by a dry etching step (RIE) with an etching depth of 70 nm.

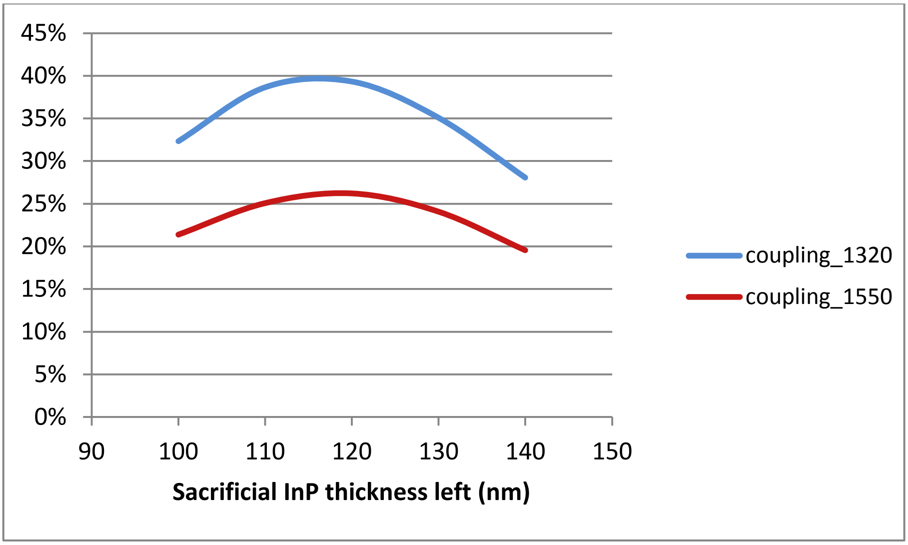

Figure 6.23: Simulation result of the grating coupling efficiency vs sacrificial layer thickness.

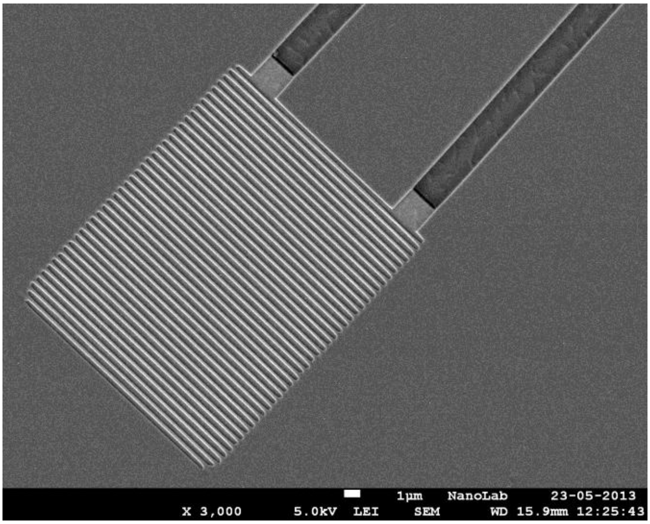

Figure 6.24: SEM picture of the grating (1320nm) with the right dose.

6.2.8 Bonding

After finishing the fabrication process, the last step is the bonding[14] of the InP sample on Si and subsequent substrate removal. Before bonding, a layer of SiO_2 is deposited on both the InP sample (200 nm thick SiO_2) and on the Si wafer (1750 nm thick SiO_2) in order to increase the adhesion of BCB. Then a layer of BCB (100 nm) is spin-coated onto the InP sample. The sample is bonded up-side down on the host-substrate, which also has a 100 nm spun BCB-layer. The combined BCB-layer is then cured for 1 hour at 280 ℃ in a vacuum environment. After bonding, the InP-substrate is removed using wet-etching in an InP selective etchant ($4HCl:1H_2O$) at 35 ^oC until the first InGaAs etch stop layer. Next, the etch-stop layer InGaAs is removed with wet etching ($10H_2O:H_2SO_4:H_2O_2$). The last InP sacrificial layer is only removed partially (to correct the gratings for the missing AlInAs-layer) by dry etching (RIE). Finally a cleaning process (stripping and diluted H_3PO_4 etching) is performed.

6.3 Conclusions and discussion

In this Chapter, the fabrication process of the first IMOS photonic crystal laser is presented. It turns out that multilayer regrowth is a very difficult process. After some trials half of one sample survived all the regrowth steps. However, after the AlInAs oxidation, no oxidized AlInAs was observed. It appears that the AlInAs layer is attacked by the HF solution which is used for removing the hard mask (Si_xN_y) . Without oxidized AlInAs layer as the current blocking layer, electrically pumped PhC lasers are not possible anymore, since short-circuiting will occur. However, optically pumped PhC lasers are still possible. After the definition of grating couplers, the sample is bonded on a host-Si wafer with BCB. In the next Chapter, the characterization of this chip will be present.

---

[14] The BCB bonding is done in cooperation with Ghent University, Belgium and the author thanks Shahram keyvaninia for his help in the bonding.

Chapter 7

Characterization of the First IMOS Laser Design

This chapter focuses on the characterization of the first IMOS laser design. Section 7.1 explains the characterization setup and the measurements. Section 7.2 shows the morphology evaluation of the sample after bonding. In Section 7.3 the micro Pl measurements are reported to check the optical emitting properties of the QWs. This section is finished with conclusions and discussions in section 7.4.

As explained in the previous chapter, during the fabrication the AlInAs oxidation layer was accidentally removed by concentrate HF solution which is used for removing the hard mask (Si_xN_y) before the last regrowth step. Without oxidized AlInAs layer as the current blocking layer, electrically pumped PhC lasers are not possible anymore, since short-circuiting will occur. However, there still seemed to be a possibility to realize the PhC membrane laser, using optical pumping. For this an adjustment to the original designed processing has been made: part of the last sacrificial InP layer is kept in order to have the input/output gratings operating at λ=1.3 µm (pump light) and λ=1.5 µm (laser output). This chapter reports on the results obtained with this.

7.1 Characterization.

The setup for the characterization[15] of the IMOS lasers (see Fig. 7.1) is similar to that used for the characterization of passive devices (section 2.3). However, instead of using a laser source at a wavelength of 1.55 µm, as for passive components, this time a laser source with a shorter wavelength (1.3 µm) is used as a pumping source. The reason for the choice of this wavelength is that the straight line defect PhC waveguide with the active region creates a cavity mode at the resonant wavelength (1.55 µm), but is transparent for the pumping wavelength (1.3 µm). Therefore the pump light can be coupled into the active region through the line-defect waveguide and be effectively absorbed in the active region [7.1]. In this way population inversion, and thus gain, can be created in the cavity. The measurement is done at room temperature. The CW pumping laser source has an output power of 11 dBm. However, only a very low power (-60dBm) is measured from the output fiber. Moreover, no optical signal around 1.55 µm can be

---

[15] The characterization is done together with Longfei Shen, Yuqing jiao, Josselin Pello and Lucie Fernandez.

detected with an optical spectrum analyzer (OSA). We also tried to collect light from the top of the PhC cavity. A very small amount of pumping light signal (1.3 µm) was detected by the OSA and no optical signal around 1.55 µm was seen. All the measurements show a high optical loss. In order to find out the source of this high loss, first a morphology evaluation of the sample (after bonding) is performed. This will be reported in the next section.

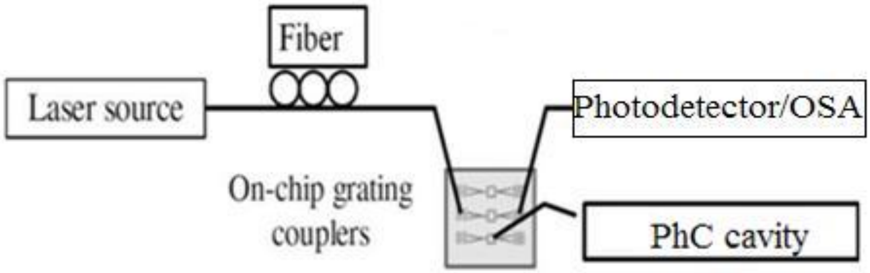

Figure 7.1: Schematic view of the characterization set-up used for the active devices.

7.2 Morphology evaluation.

To determine the reasons for the very high loss that is found, a SEM evaluation is done to check the morphology of the sample after bonding. It is seen from Fig. 7.2 and Fig. 7.3 that many of the PhC cavities are broken, collapsed or even removed. However, the waveguide and tapers still look good (see Fig. 7.4) although some sidewall roughness is present. It is believed that the damages to the PhC cavities occur because the mechanical strength of the membrane is strongly reduced after the PhC holes are defined and etched. This could make the membrane PhC cavity too fragile to resist force. Due to the presence of the only partially removed sacrificial InP layer, the accumulated force on the PhC region resulting from the pressure exerted in the bonding process, can be relatively high.

Therefore, during the bonding process, many of the PhC cavities are damaged. Nevertheless, the waveguide and taper part of the membrane are strong enough to resist the bonding pressure. In these parts the etching depth is larger, since there is no lag effect, so that the partial InP-layer is removed from the trenches. This reduces the force, since the area with bonding press is reduced. This is also supported by the successful bonding of the various passive components presented in Chapter 2.

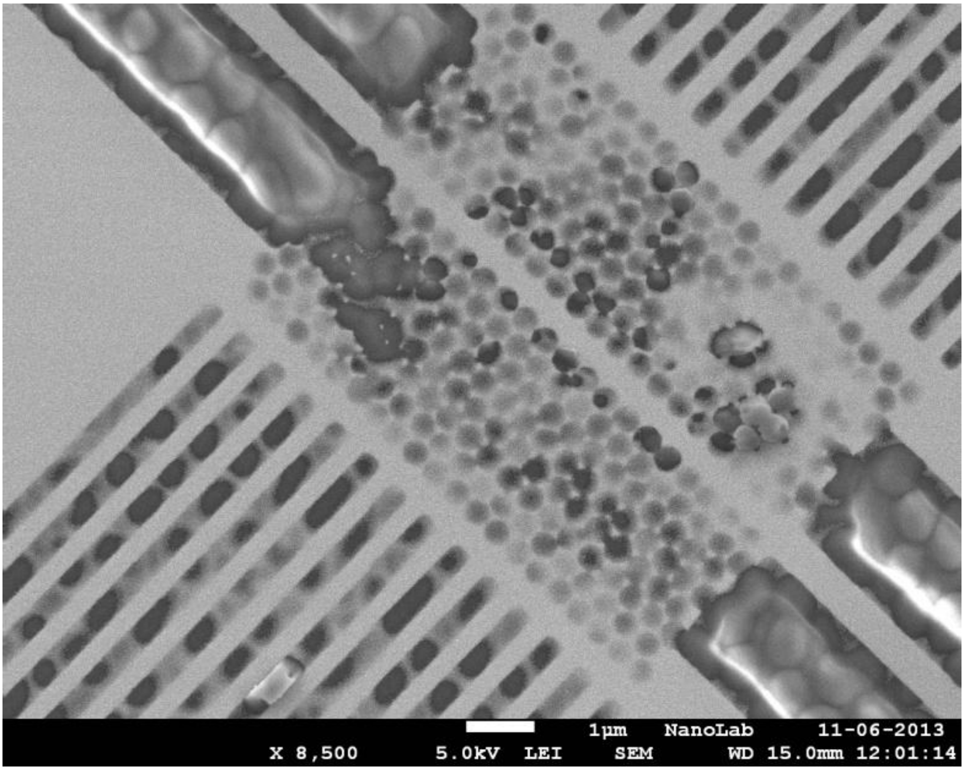

Figure 7.2: One of the damaged PhC cavities after bonding.

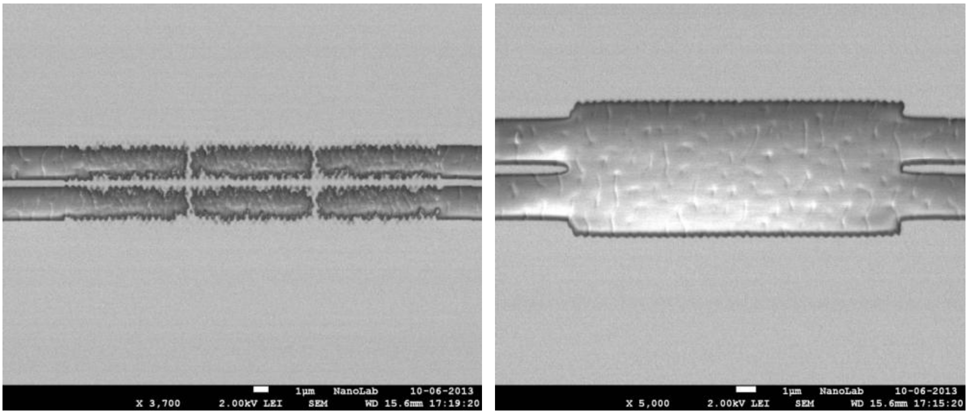

Figure 7.3: a) One of the collapsed PhC cavities after bonding. b) One of the complete removed PhC cavities after bonding.

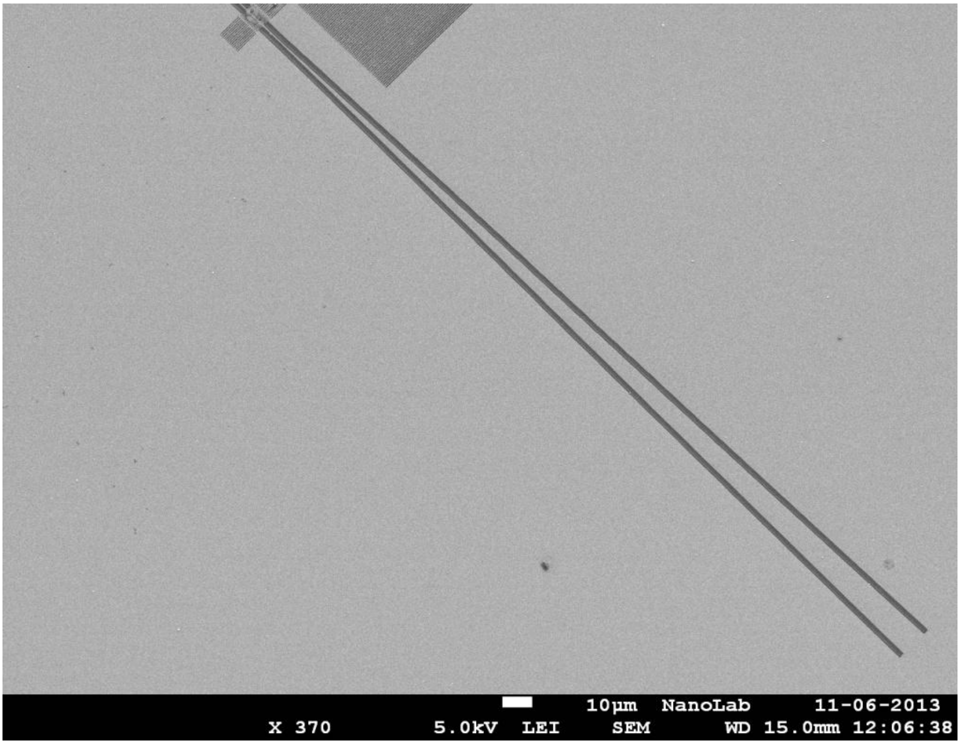

Figure 7.4: The waveguide and tapers of PhC devices after bonding.

7.3 Micro photoluminescence analysis.

As in Chapter 3, Micro photoluminescence (μPL) is used to evaluate the emission of the quantum wells (QWs) in the submicron active region. The motivation is to determine whether the QWs are damaged by the processing.

7.3.1 Micro PL setup

For the experimental characterization of the fabricated structures, a room temperature μPL set-up is used. Fig. 7.5 shows the schematic representation of this set-up. The sample is placed on an x-y-z stage whose its position is controlled with a piezoelectric controller. An microscope objective is used for excitation and collection of the luminescence to characterize the structures. A continuous wave laser (λ = 660 nm) is used to excite the realized structures. The exciting beam has a spot size of around 6 μm. The excitation of the QWs and the collection of the PL signal are done with a high numerical aperture (NA) microscope objective (50X or 100X, N.A.=0.5). Finally the signal is spectrally analyzed with a grating and detected in a liquid nitrogen cooled InGaAs detector array.

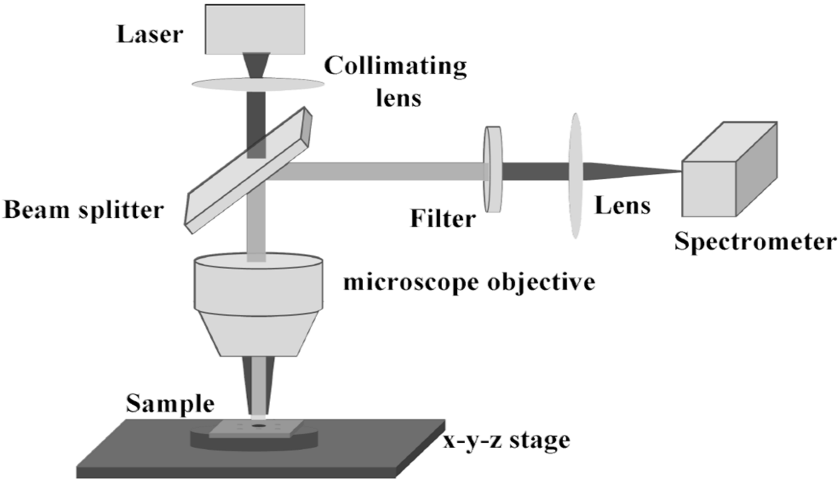

Figure 7.5: Micro PL setup

7.3.2 μPL measurement

The first μPL measurement[16] is done with the base wafer, which is a full wafer with 4 InGaAsP QWs, before applying any processing or regrowth. The spectrum is shown in Fig. 7.6. One can see that the peak wavelength is around 1.55 μm, as designed, with a FWHM of about 70 nm.

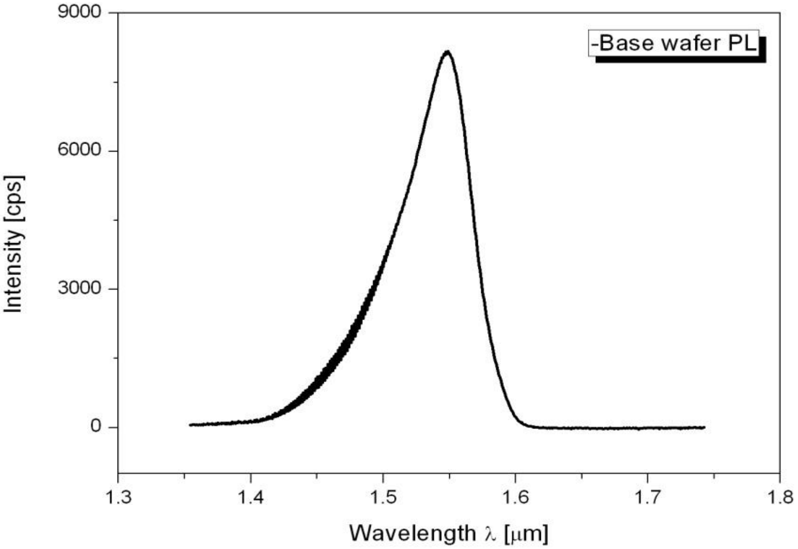

Figure 7.6: Micro PL of the base wafer (4 InGaAsP QWs)

Next, μPL was done for the final laser sample. However, no signal around 1.5 μm is detected. A possible reason for this might be that the pumping light is absorbed in the top layers, which are the InP layers and Q (1.2) layers, before reaching the QWs (see Fig.7.7).

---

[16] The μPL is done together with Rob van der Heijden and the author thanks him for his help in the measurement.

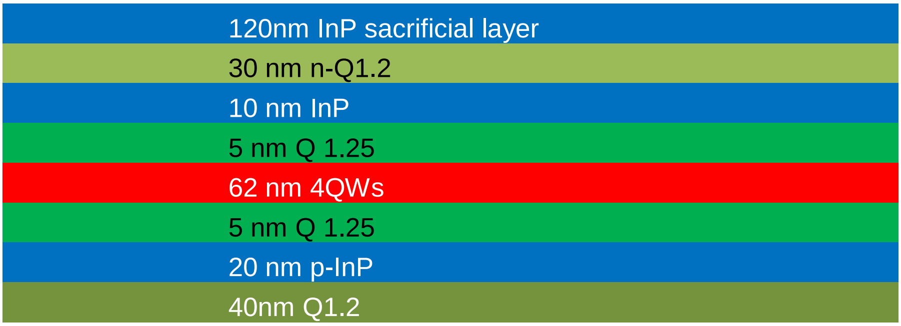

Figure 7.7: Layer stack of membrane after bonding

In order to make an estimation of the amount of 660 nm light that reached the QWs, the following derivations are performed. The complex expression of the refractive index is given in Eq. 7.1, where n_r is real part and k is the imaginary part:

$$n = n_r + jk \tag{7.1}$$

The propagation of the pumping light can be described by Eq. 7.2. Here A_0 represents the amplitude, L is propagation depth and λ is the wavelength of the input light (λ = 0.66 μm).

$$A = A_0 e^{\frac{jn2\pi L}{\lambda}} \tag{7.2}$$

using the complex expression for the refractive index from Eq. 7.1, then we have

$$A = A_0 e^{\frac{jn_r 2\pi L}{\lambda}} e^{\frac{-k2\pi L}{\lambda}} \tag{7.3}$$

To calculate the power of the pumping light, we multiply the amplitude expression with its complex conjugate.

$$P = AA^* \tag{7.4}$$

Then finally we have the expression of the power of the pumping light, as a function of propagation depth, which is:

$$P = A_0^2 e^{\frac{-2k2\pi L}{\lambda}} \tag{7.5}$$

For the InP layers, k=0.3 [7.2], and the total thickness L=0.13 µm, thus

$$P_{\mathrm{InP}} = 0.48 * A_0^2 \tag{7.6}$$

The same calculation for Q (1.25) k=0.37 [7.2], with a total thickness L=0.035 µm:

$$P_{\mathrm{Q}} = 0.81 * A_0^2 \tag{7.7}$$

Together we obtain:

$$P_{\mathrm{QW}} = 0.38 * A_0^2 \tag{7.8}$$

This means still a significant amount of pumping light (38%) can still reach the QWs, Thus a PL signal from the QWs can be expected. The fact that none is observed indicates that the remaining QWs themselves might be degraded and do not emit anymore. In order to investigate this hypothesis, the results and analysis in Chapter 3 need to be called back. In Chapter 3 it is shown that processing induced defects will degrade the QWs (see Section 3.4.2). For example, dry etching will create a lot of defects on the sidewalls of the active regions and the high temperature in the regrowth process will help these defects to diffuse into the QWs. However, the degradation of the active material (InGaAsP QWs) in the tests described in Chapter 3 due to processing is limited because of the small number of dry etching and regrowth steps. However, for the laser sample fabrication described in Chapter 6, a much more complex processing is performed. For example, more dry etching steps are done and therefore more defects are created. Also, the number of regrowth steps is increased from one to three because of the requirement of current blocking and p-doping layers. Thus, due to the high temperature of the regrowth, defects can diffuse to the QWs and degrade them severely.

Furthermore, the shape of the active region has a large impact on this degradation mechanism. In Chapter 3 a relation between defect density and area of the QWs is found from the trap model analysis (see section 3.4.2 d). As one can see in Fig 7.7, the normalized defect density is increasing with the ratio of the circumference of the active region divided by the area. Because of the requirement for the PhC cavities, the active region of the laser sample has to be a rectangular shape with a large length and a small width, as given in Table 7.1. One can see that the ratio circumference/area of these shapes is so large that they exceed the range of Fig.7.8. According to Fig 7.8, these large ratios (circumference/area) implies that the defect density introduced by process is very high. Consequently, these defects will degrade the quality of the QWs, so that they cannot emit light anymore. All of these factors together provide a plausible explanation for the absence of a light signal around 1.5 μm in the μPL measurement.

Table 7.1 The parameters of the active region used in PhC cavities

Active region	Length (μm)	Width (μm)	Circumference (μm)	Area (μm^2)	Circumference/Area (μm^{-1})
1	4	0.2	8.4	0.8	10.5
2	4	0.3	8.6	1.2	7.2
3	4	0.5	9	2	4.5

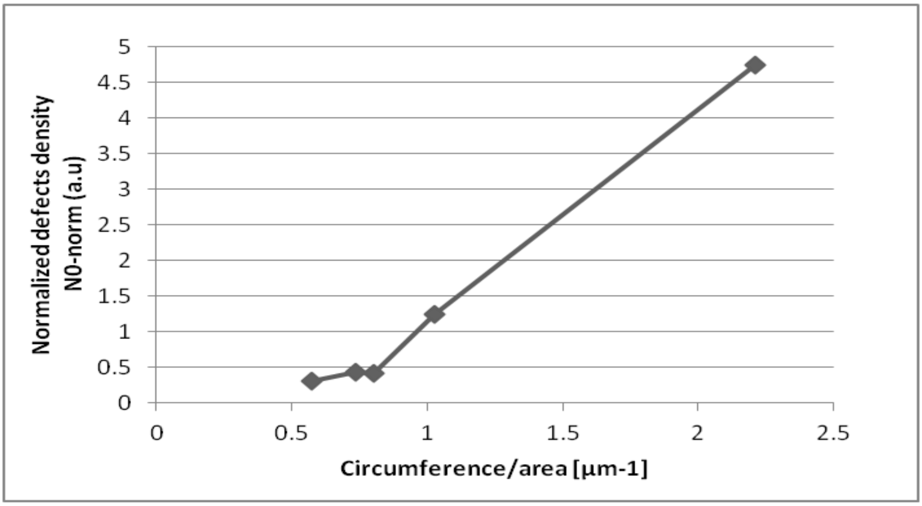

Figure 7.8: Normalized defect density vs circumference/area

7.4 Conclusion

The characterization in Chapter 7 unfortunately shows that the devices don’t perform as hoped for. The measurement results show a high optical loss. After checking in the SEM it is seen that many of the PhC cavities are damaged, because of the force implemented during the bonding process. However, the waveguide and tapers still stand well. We believed that this is because the mechanical strength of the membrane part of the PhC cavities is strongly reduced after the etching of the PhC hole arrays. This makes the membrane at the PhC cavity too fragile to resist the pressure in the bonding process, which result in a extra high force due to the presence of a remaining InP layer on top of the PhC. Nevertheless, the mechanical strength of the waveguide and the taper part of the membrane is still strong enough to resist the bonding force. This is also proven by the various IMOS passive components realized with good quality, as shown in Chapter 2.

Furthermore, a series of µPL measurements are performed to check the optical quality of the QWs. No emitting light from the QWs is detected.

Despite presence of the multiple layers on top of the QWs, calculations show that a sufficient amount of light can still reach the QWs. This indicates that the lack of QWs emission is due to degradation from processing induced defects. Analysis based on the processing steps, especially the dry etching and the regrowth that the sample went through, and the trap model theory in Chapter 3 support this hypothesis.

In the next chapter the lessons that can be drawn from these attempts will be discussed and recommendations will be given for the future research directions.

Chapter 8

Conclusions and recommendations

This final chapter summarizes the work presented in the previous chapters. In Section 8.1, the conclusions of this thesis are given. In Section 8.2, the outlook and the recommendations for future work are discussed.

8.1 Conclusions

As the first PhD thesis on IMOS, the results presented here represent progress towards a new platform for the next generation PICs. IMOS makes it possible to use InP based membranes, which contain both passive and active devices, on top of silicon chips. Reporting on the early research, this thesis focuses on the technology development, the device design, the fabrication and the characterization of photonic components for the IMOS platform. The long term goal is to put such membranes on electronic chips (CMOS) to provide high-speed on-chip data transport.

First, in Chapter 2, the first generation IMOS passive components (waveguides, MMI’s, etc) with small dimensions and good performance have been demonstrated. These are the basic circuitry building blocks for future PICs on IMOS. The good performance and small dimensions of the first generation IMOS passive devices shows the integration potential of the IMOS platform.

Since full PICs contain both passive and active components, a successful active-passive integration in IMOS is essential. In Chapter 3, an active-passive integration with sub-micrometer active areas, based on selective area regrowth, is developed. The interface between the active and passive areas shows good quality in terms of morphology. Moreover, the micro PL measurement shows that the QWs in the sub-micron size active region are still able to emit light which indicates that the degradation of the active material due to these processing steps is limited. A successful active-passive integration within submicron range will enable the possibility of very small lasers with very small threshold currents and low power consumption. This small dimension also makes it suitable for integration with silicon CMOS which is the long term goal for the IMOS platform.

Next in Chapter 4, in order to realize direct electrical pumping and inject carriers efficiently into the IMOS active devices, a dielectric aperture is realized using oxidized AlInAs. Various oxidation tests have been done for the process exploration and optimization. The influence of temperature and time on the oxidation depth and the surface morphology is determined. It is found that high temperatures and long oxidation times increase the oxidation depth dramatically, but can also degrade the surface quality because of phosphorus depletion. Electrical measurements show that AlInAs oxidation gives a significant increase by 3 orders of magnitude in the electrical resistance, which make this technique very promising for current blocking in the IMOS platform. The AlInAs oxidation technique developed in this thesis has already been applied to other IMOS active devices [8.1]. Nevertheless, it should be mentioned that AlInAs oxidation also causes strain in the layers. Since oxidation changes the composition of the AlInAs layer, this layer is no longer lattice matched to InP. An oxidized AlInAs layer should therefore not be exposed to additional stress (e.g. during cleaving) since it then loses its stability.

Based on the technology development in the previous chapters, in Chapter 5 a line defect PhC waveguide cavity is designed and simulated. Optical simulation results show that this cavity gives good performance in terms of the quality factor and the tolerance to manufacturing imperfections. Calculations also show the influence of the physical factors such as doping, AlInAs oxidation and BCB bonding. Moreover, since an electrically pumped photonic crystal laser is pursued, electrical simulations for the layer stack are also performed, in order to optimize the carrier injection. Based on the electric simulation results, an optimized layer stack is designed which shows strongly reduced threshold currents.

In Chapter 6, in cooperation with SMARTPHOTONICS and Ghent University, the manufacturing of the designed laser in Chapter 5 is described. The mask design, process plan and fabrication results of the device are explained. It turns out that multilayer regrowth is a difficult process. After several runs, half of one sample survived all the regrowth steps. However, after the AlInAs oxidation, no oxidized AlInAs was observed. It appears that a protective cap layer was accidentally removed in a cleaning step, so that the AlInAs layer is attacked by the HF solution which is used for removing the Si_xN_y hard mask. Without the oxidized AlInAs layer for the current blocking, electrically pumped PhC lasers are not possible anymore, since short-circuiting will occur. However, optically pumped PhC lasers are still possible. After the definition of grating couplers, the sample is bonded on a host-Si wafer with BCB.

The characterization in Chapter 7 shows that the devices don’t perform as expected. The measurement shows a high optical loss. After checking in the SEM it is seen that many of PhC cavities are damaged because of the force exerted during the bonding process. Further Micro PL measurements didn’t detect any emitted light from the QWs, which indicates that the QWs have strongly been degraded due to the processing.

8.2 Outlook and Recommendations

The results presented in this thesis indicate the feasibility of developing PICs in IMOS, including both active and passive functions. However, a number of issues still need to be addressed before the concept is fully operational. First, in this thesis, the InP sample is processed and then bonded on the Si wafer. Because of the strong force between InP die and Si host wafer, a lot of PhC cavities are damaged. Together with the bonding yield issues, for the long term, it is advisable to use a post-bonding method. This means that first the bonding of InP on Si is done, then one can start the process from a successfully bonded membrane. This will greatly reduce the yield problem.

Although the first generation passive components show good performance, further improvement of the performance is still possible. For instance, the waveguide propagation loss is still relatively high. This is mainly due to the side wall roughness. The negative EBL resist HSQ, which is already used to make ultra-small plasmonic lasers, can yield better results . Furthermore, a thinner positive EBL resist (PMMA) can be used to define the very small active structures. In principle thinner e-beam resist results in less scattering of the electrons and thus improve the resolution.

For the active devices, it is advisable to make optical pumped devices which are simpler in design or fabrication, before going directly to the electrical pumping. In Chapter 4, it is shown that AlInAs oxidation, which is a mature technology for VCSELs, can also be used for the IMOS platform. However, one should keep in mind that, the oxidation temperature is as high as 500 ^{o}C. If materials are used which can't survive such a high temperature, this technique should not be used for current confinement functions. Moreover it should be mentioned that AlInAs oxidation causes strain in the layers. Since oxidation changes the composition of the AlInAs layer, this layer is no longer lattice matched to InP. Thus an oxidized AlInAs layer should not be exposed to external stress, since it then can lose its mechanical stability.

Finally, although regrowth provides the freedom to the designers to optimize each required function, the other side of the picture for this approach is that multiple extra growth steps are required on processed surfaces. This makes it difficult to obtain a highly reproducible regrowth quality and therefore it may cause a yield problem. Last but not least, the thermal management of the membranes needs to be addressed for future research, especially for the active devices, since the adhesive layer (BCB) used for bonding is not a good thermal conductive material.

The results so far show that IMOS is potentially a promising platform for PICs. Nevertheless many issues need to be addressed and more technology development is required to make IMOS a mature platform for the next generation PICs.

References

[1.1] TEXAS INSTRUMENTS
http://www.ti.com/corp/docs/kilbyctr/downloadphotos.shtml

[1.2] http://inventors.about.com/od/istartinventions/a/intergrated_circuit.htm

[1.3] Moore, Gordon E. "Cramming more components onto integrated circuits", Electronics 38, 1965.

[1.4] Bowen Wang, "Light control by nanostructured metal surfaces and photonic crystals in nanobeams and freestanding membranes", PhD thesis, October, 2011.

[1.5] Mehmet Ali Dündar, "Optofluidic and photothermal control of InGaAsP photonic crystal nanocavities", PhD thesis, september, 2011.

[1.6] W. Bogaert, et al., "SOI nanophotonic waveguide structures fabricated with deep UV lithography", IEEE Photon. Technol. Lett. 16, p.1328 (2008).

[1.7] G. Roelkens, et al.,"Adhesive Bonding of InP/InGaAsP Dies to Processed Silicon-On-Insulator Wafers using DVS-bis-Benzocyclobutene", Journal of The Electrochemical Society, vol. 153, pp. G1015–G1019, 2006.

[1.8] G. Roelkens, et al"III-V/Si Photonics by die to wafer bondig", Materials Today. vol 10, Nr 7-8, pp.36-43,July-August,2007.

[1.9] Uzma Khalique, "Polarization based Integration Scheme (POLIS)", PhD thesis, October 2008.

[1.10] M.R. Gokhale, P.V. Studenkov, J. U. Mchale, J. Thomson, J. Yao and J.V. Sanders, "Uncooled, 10Gb/s 1310 nm electroabsorption modulated laser", presented at the Optical Fiber Communication Conf,Atlanta, GA, 2003.

[1.11] P.V. Studenkov., M.R. Gokhale, J. Wei, W.Lin, I. Glesk, P.R. Prucnal and S.R. Forrest, "Monolithic integration of an all optical Mach-Zehnder demultiplexer using an asymmetric twin-waveguide structure", IEEE Photon Technol. Lett., vol.13, no.6, p.600-602, 2001.

[1.12] V.M. menon, W. Tong, C. Li, F. Xia, I. Glesk, P.R. Prucnal and S.R. Forrest, "All optical-wavelength conversion using a regrowth free monolithically integrated Sagnac interferometer", IEEE Photon Technol. Lett., vol.15, no.2, p.254-256, 2003.

[1.13] ASIP. http://www.asipinc.com

[1.14] J.J.G.M. van der Tol, Y.S. Oei, U. Khalique, R.Notzel, M.K.Smit,w “InP-based photonic circuits: Comparison of monolithic integration techniques”, Progress in Quantum Electronics, Vol 34, July 2010.

[2.1] R. P. Nagarajan and M.K. Smit, “Photonic integration”, IEEE LEOS Newsletter. vol 21, Nr. 3, pp. 4-10.

[2.2] F. Bordas, F. Van Laere, G. Roelkens, E. J. Geluk, F. Karouta, P.J. van Veldhoven, R. Nötzel, D. Van Thourhout, R. Baets and M.K. Smit,” Compact Grating Coupled MMI on DVS-BCB Bonded InP-Membrane”, Proc. ECIO 2008, Eindhoven (NL).

[2.3] Pello, J., Tol, J.J.G.M. van der, Keyvaninia, S., Veldhoven, P.J. van, Ambrosius, H.P.M.M., Roelkens, G.C. & Smit, M.K. (2012). “High-efficiency ultrasmall polarization converter in InP membrane”. Optics Letters, 37(17), 3711-3713.

[2.4] Frederik Van Laere,”Photonic Integrated Circuits and Fibre Couplers Based on InP Bonded Membranes”, PhD thesis, November, 2008.

[2.5] M. L. Dakss, L. Kuhn, P. F. Heidrich and B. A. Scott . Grating coupler for efficient excitation of optical guided waves in thin films. Applied Physics Letters, 16(12):523–525, 1970.

[2.6] T. Tamir and S. T. Peng . Analysis and design of grating couplers. Applied Physics, 14(3):235–254, 1977.

[2.7] R. Zhang et al. (2009). Sub-micrometer active-passive integration for InP-based membranes on silicon. Proceedings 14th Annual Symposium of the IEEE Photonics Benelux Chapter, 5-6 November 2009, Brussels, Belgium (pp. 121-124).

[2.8] J.J.G.M. van der Tol, R. Zhang, J. Pello, F. Bordas, G. Roelkens, H. Ambrosius, P. Thijs, F. Karouta and M.K. Smit, “Photonic Integration in Indium-Phosphide Membranes on Silicon” , IET Optoelectronics, Vol. 5, Iss. 5, pp. 218–225, 2011.

[2.9] Dumon, P.; Bogaerts, W.; Wiaux, V.; Wouters, J.; Beckx, S.; Van Campenhout, J.; Taillaert, D.; Luyssaert, B.; Bienstman, P.; Van Thourhout, D.; Baets, R., "Low-loss SOI photonic wires and ring resonators fabricated with deep UV lithography," Photonics Technology Letters, IEEE , vol.16, no.5, pp.1328,1330, May 2004.

[2.10] Bian, Z.; Liu, Bin; Shakouri, Ali, "InP-based passive ring-resonator-coupled lasers," Quantum Electronics, IEEE Journal of , vol.39, no.7, pp.859,865, July 2003.

[2.11] Vernik, I.V.; Ohki, T.A.; Ketchen, M.B.; Bhushan, M., "Performance characterization of PD-SOI ring oscillators at cryogenic temperatures," SOI Conference (SOI), 2010 IEEE International , vol., no., pp.1,2, 11-14 Oct. 2010.

[2.12] Martin T. Hill, Harmen J. S. Dorren, Tjibbe de Vries, Xaveer J. M. Leijtens, Jan Hendrik den Besten, Barry Smalbrugge, Yok-Siang Oei, Hans Binsma, Giok-Djan Khoe&Meint K. Smit,“A fast low-power optical memory based on coupled micro-ring lasers,” Nature 432, 206-209 , Novemberm, 2004.

[2.13] Yebo, N. A.; Taillaert, D.; Roels, J.; Lahem, D.; Debliquy, M.; Van Thourhout, D.; Baets, R., "Silicon-on-Insulator (SOI) Ring Resonator-Based Integrated Optical Hydrogen Sensor," Photonics Technology Letters, IEEE , vol.21, no.14, pp.960,962, July15, 2009.

[2.14] M. Bachmann, P. A. Besse, and H. Melchior, "General self-imaging properties in N × N multimode interference couplers including phase relations," Appl. Opt. 33, 3905-3911 (1994)

[2.15] Jingtao Zhou, Huajun Shen, Huihui Zhang, and Xinyu Liu, "Design and fabrication of a compact multimode interference splitter with silicon photonic nanowires," Chin. Opt. Lett. 7, 1041-1044 (2009).

[2.16] R. Zhang, F. Bordas, J.J.G.M. van der Tol, P. Thijs, G. Roelkens ,T. de Vries and M.K. Smit, “Active-Passive Integration in III-V Membranes on Silicon”, International Nano-optoelectronics Workshop 2009, Stockholm and Berlin, Germany, August 2-16, 2009.

[3.1] F. Bordas, G. Roelkens, R. Zhang, E.J. Geluk, F.Karouta, J.J.G.M. van der Tol, P.J. van Veldhoven, R.Nötzel, D. van Thourhout, R.G.F. Baets and M.K. Smit, “Compact passive devices in InP membrane on silicon.” Proceedings of the 35th European Conference on Optical Communication (ECOC 2009) 20 - 24 September 2009, Vienna(pp. 4.2.4-1/2).

[3.2] J.J.G.M. van der Tol, Y.S. Oei, U. Khalique, R.Notzel, M.K.Smit,w “InP-based photonic circuits: Comparison of monolithic integration techniques”, Progress in Quantum Electronics ,Vol 34, July 2010.

[3.3] R. Zhang, F. Bordas, J.J.G.M. van der Tol, H. Ambrosius, G. Roelkens, M.A.Dundar and M.K. Smit, “Sub-micrometer Active-Passive Integration for InP-based Membranes on Silicon” Proc. ECIO 2010, Cambridge (UK), paper ThH1.

[3.4] L.A. Giannuzzia, F.A. Stevieb, “A review of focused ion beam milling techniques for TEM specimen preparation” Micron 30 197–204, February 1999.

[3.5] Mehmet Ali Dündar, " Optofluidic and photothermal control of InGaAsP photonic crystal nanocavities", PhD thesis, September 2011.

[3.6] R. Zhang, J.J.G.M. van der Tol and M.K. Smit," Trap Model Analysis on Submicron Active-Passive Integration for InP-based Membranes on Silicon (IMOS)" Proceedings of the 17th Annual symposium of the IEEE Photonics Benelux Chapter , 29-30 November 2012, Mons, Belgium.

[3.7] Joseph Micallef,et al "Cation inter-diffusion in GaInP/GaAs Single Quantum Wells ", Proceeding of Material. Resource Society. Symposium. Vol. 484, 1998.

[3.8] R. Zhang, Frederic Bordas, Jos van der Tol, Peter Thijs, Huub Ambrosius, Gunther Roelkens, Mehmet Dundar, Tjibbe de Vries, and Meint Smit, "Sub-micrometer active-passive integration for InP-based membranes on silicon. Proceedings 14th Annual Symposium of the IEEE Photonics Benelux Chapter, 5-6 November 2009, Brussels, Belgium (pp. 121-124).

[4.1] Bryan Ellis, Marie A. Mayer, Gary Shambat, Tomas Sarmiento, James Harris, Eugene E. Haller and Jelena Vuc kovic, "Ultralow-threshold electrically pumped quantum dot photonic-crystal nanocavity laser" ,NATURE PHOTONICS , VOL 5, MAY 2011.

[4.2] O. Painter, et al." Two-Dimensional Photonic Band-Gap Defect Mode laser", *Science* 284, 1819 (1999);

[4.3] Park, H. G. et al. Electrically driven single-cell photonic crystal laser. Science 305, 1444–1447 (2004).

[4.4] Park, H. G. et al. Characteristics of electrically driven two-dimensional photonic crystal lasers. IEEE J. Quantum Electron. 41, 1131–1141 (2005).

[4.5] Shinji Matsuo, Koji Takeda, Tomonari Sato, Masaya Notomi, Akihiko Shinya, Kengo Nozaki, Hideaki Taniyama, Koichi Hasebe, and Takaaki Kakitsuka, "Room-temperature continuous-wave operation of lateral current injection wavelength-scale embedded active-region photonic-crystal laser," Opt. Express **20**, 3773-3780 (2012).

[4.6] H. Gebretsadik, K. Kamath, W-D. Zhou, and P. Bhattacharya, "Lateral oxidation of InAlAs in InP-based heterostructures for long wavelength vertical cavity surface emitting laser applications," Appl. Phys. Lett. 72 (2), 12 January 1998.

[4.7] D. L. Huffaker,O. Baklenov, L. A. Graham, B. G. Streetman, and D. G. Deppe ," Quantum dot vertical-cavity surface-emitting laser with a dielectric aperture," Appl. Phys. Lett. 70 (18), 5 May 1997.

[4.8] Norihiro Iwai, Toshikazu Mukaihara, Nobumitsu Yamanaka, Mitsumasa Ito, Satoshi Arakawa, Hitoshi Shimizu and Akihiko Kasukawa, “1.3 μm Laser Array on p-type Substrate using Selective Oxidation of AlInAs” , Furukawa Review No.20, April 2001.

[4.9] J.J.G.M. van der Tol, R. Zhang, J. Pello, F. Bordas, G. Roelkens, H. Ambrosius, P. Thijs, F. Karouta and M.K. Smit, “Photonic Integration in Indium-Phosphide Membranes on Silicon” , IET optoelectronics, June, 2010.

[4.10] R. Zhang, J.J.G.M. van der Tol, H. Ambrosius, P. Thijs, B. Smalbrugge, T. de Vries, G. Roelkens, F. Bordas, and M.K. Smit, “Oxidation of AlInAs for Current Blocking in a Photonic Crystal Laser”, Proc. COMMAD 2010, Canberra (Australia), paper105.

[4.11] R. Zhang, J.J.G.M. van der Tol, P. Thijs, and M.K. Smit, “ Oxidation of AlInAs for Current Blocking in a Photonic Crystal Laser.”, Proceedings of the 15th Annual symposium of the IEEE Photonics Benelux Chapter, 18-19 November 2010, Delft, Netherland.

[4.12] L. M. Augustin,” Polarization Handling in Photonic Integrated Circuits” PhD thesis, page 51, June, 2008.

[4.13] Premchander Perumal, Jong Min Kim and Yong Tak Lee,” Investigations of the characteristics of strain-free oxidation on InAlAs epilayer lattice matched to indium phosphide”, Appl. Phys. Lett. 88, 201914, 2006.

[4.14] N. Iwai, T. Mukaihara, M. Itoh, N. Yamanaka, S. Arakawa, H. Shimizu and A. Kasukawa, “1.3pm GalnAsP SL-QW AI-oxide confined inner stripe lasers on plnP substrate with AllnAs-oxide confinement layer”, ELECTRONlCS LETTERS, Vol.34, No.14, July, 1998.

[4.15] H. Gebretsadik, K. Kamath, W-D. Zhou, and P. Bhattacharya, “Lateral oxidation of InAlAs in InP-based heterostructures for long wavelength vertical cavity surface emitting laser applications”, Appl. Phys. Lett. 72 (2), January, 1998.

[5.0] Koji Takeda, Tomonari Sato, Akihiko Shinya, Kengo Nozaki, Wataru Kobayashi, Hideaki Taniyama, Masaya Notomi, Koichi Hasebe, Takaaki Kakitsuka & Shinji Matsuo,” Few-fJ/bit data transmissions using directly modulated lambda-scale embedded active region photonic-crystal lasers”, Nature Photonics 7, 569–575 (2013)

[5.1] Bowen Wang, “Light control by nanostructured metal surfaces and photonic crystals in nanobeams and freestanding membranes”, PhD thesis, October, 2011.

[5.2] E. Yablonovitch, “Inhibited Spontaneous Emission in Solid-State Physics and Electronics”, Phys. Rev. Lett. 58, 2059 (1987).

[5.3] S. John, “Strong localization of photons in certain disordered dielectric superlattices”, Phys. Rev. Lett. 58, 2486 (1987).

[5.4] E. Yablonovitch, T. J. Gmitter, and K. M. Leung, “Photonic band structure: The face-centered-cubic case employing nonspherical atoms”, Phys. Rev. Lett. 67, 2295 (1991).

[5.5] Masahiro Nomura, Satoshi Iwamoto, Katsuyuki Watanabe, Naoto Kumagai, Yoshiaki Nakata, Satomi Ishida, and Yasuhiko Arakawa, “Room temperature continuous-wave lasing in photonic crystal nanocavity”, OPTICS EXPRESS, Vol. 14, No. 13, June, 2006.

[5.6] M. Bayindir, B. Temelkuran, and E. Ozbay, “Photonic-crystal-based beam splitters”,Appl. Phys. Lett 77, 3902 (2000).

[5.7] Eiichi Kuramochi, Masaya Notomi, Satoshi Mitsugi, Akihiko Shinya, and Takasumi Tanabe, “Ultrahigh-Q photonic crystal nanocavities realized by the local width modulation of a line defect” Appl. Phys. Lett. 88, 041112 2006.

[5.8] Yoshihiro Akahane, Takashi Asano, Bong-Shik Song & Susumu Noda.” High-Q photonic nanocavity in a two-dimensional photonic crystal” , NATURE VOL 425 30 October, 2003.

[5.9] Park, H. G. et al. Characteristics of electrically driven two-dimensional photoniccrystal lasers. IEEE J. Quantum Electron. 41, 1131–1141 (2005).

[5.10] Bowen Wang, “Light control by nanostructured metal surfaces and photonic crystals in nanobeams and free standing membranes”, PhD thesis, October, 2011.

[5.11] Abigaël Adriana Maria Kok, “Pillar photonic crystals in integrated circuits”, PhD thesis, June 2008.

[5.12] Shinji Matsuo, Akihiko Shinya, Takaaki Kakitsuka, Kengo Nozaki, Toru Segawa, Tomonari Sato,Yoshihiro Kawaguchi and Masaya Notomi,” High-speed ultracompact buried heterostructure photonic-crystal laser with 13 fJ of energy consumed per bit transmitted” NATURE PHOTONICS VOL 4 SEPTEMBER 648 2010.

[5.13] Masaya Notomi and Hideaki Taniyama, “On-demand ultrahigh-Q cavity formation and photon pinning via dynamic waveguide tuning”, OPTICS EXPRESS,Vol. 16, No. 23, November, 2008.

[5.14] http://www.rp-photonics.com/q_factor.html

[5.15] R. J. Hussey, G. I. Sproule, J. P. McCaffrey, and M. J. Graham,”Characterization of Oxides Formed on InP, InGaAs, InAlAs, and InGaAs/InAlAs Heterostructures at 300–500°C”, Oxidation of Metals, Vol. 57, Nos. 5/6, June 2002.

[5.16] Uzma Khalique, “Polarization based Integration Scheme (POLIS)”, PhD thesis, October 2008.

[5.17] http://www.nextnano.de/

[5.18] Michael Bass, Eric W . Van Stryland, David R . Williams, William L.Wolfe, Pamela L.Derry, Luis Figueroa, Chi-Shain Hong, “HANDBOOK OF OPTICS”, Second Edition, QC369 .H35,1995.

[6.1] Abigaël Adriana Maria Kok, “Pillar photonic crystals in integrated circuits”, PhD thesis, June 2008.

[6.2] Kanda K. Energy dispersive X-ray spectrometer: U.S. Patent 5,065,020[P]. 1991-11-12.

[6.3] A.R. Clawson,” Guide to references on III±V semiconductor chemical etching”, Materials Science and Engineering, 31 (2001).

[7.1] Shinji Matsuo, Akihiko Shinya, Takaaki Kakitsuka, Kengo Nozaki, Toru Segawa, Tomonari Sato,Yoshihiro Kawaguchi and Masaya Notomi,” High-speed ultracompact buried heterostructure photonic-crystal laser with 13 fJ of energy consumed per bit transmitted” NATURE PHOTONICS VOL 4 SEPTEMBER 648 2010.

[7.2] S.Adachi, al ”Properties of Indium Phosphide” Emis Datareviews Series No. 6, Published by INSPEC, The Institution of Eletrical Engineers, London and New York.

[8.1] Bhat, S.P., Tol, J.J.G.M. van der, Roelkens, G.C. & Smit, M.K. (2012). Feasibility study of an InP Membrane On Silicon(IMOS) laser. Poster presented at Proceedings of the 16th European Conference on Integrated Optics (ECIO2012), April 18-20, 2012, Sitges, Spain.

List of abbreviations

As	arsenide
Au	gold
BCB	benzocyclobutene
CDL	critical dimension loss
COBRA	COmmunication technologies Basic Research and Applications
CMOS	Complementary Metal Oxide Semiconductor
CW	continuous wave
Cr	chromium
DBR	distributed Bragg reflector
EDS	Energy-Dispersive X-ray Spectroscopy ()
EBL	electron-beam lithography
FDTD	finite-difference time domain
FIB	focused ion beam
FPR	free propagation region
FSR	free spectral range
FWHM	full-width-at-half-maximum
Ga	gallium
HF	hydrofluoric acid
ICP-RIE	inductively coupled plasma - reactive ion etching
ICs	Integrated circuits
In	Indium
InP	Indium Phosphide
IMOS	InP-based Membrane on Silicon
µPL	micro photoluminescence

MOVPE	metal-organic vapor-phase epitaxy
MMI	Multimode interference
n.i.d.	non-intentionally doped
NA	numerical aperture
OSA	optical spectrum analyzer
PML	perfectly-matched layers
P	phosphide
PICs	photonic integrated circuits
PECVD	plasma-enhanced chemical vapor deposition
POLIS	polarization based integration scheme
PhC	photonic crystal
Pt	platinum
Q factor	quality factor
QW	quantum well
QWI	quantum well intermixing effect
RIE	reactive ion etching
Si	silicon
Si_xN_y	silicon nitride
SSI	small-scale integration
SNR	signal-to-noise ratio
SOA	semiconductor optical amplifier
SOI	silicon-on-insulator
TW	twin-guide
Ti	titanium
VCSEL	vertical-cavity surface-emitting laser
VLSI	very large-scale integration

Appendix

A1-Key process flow of the E-PhC laser

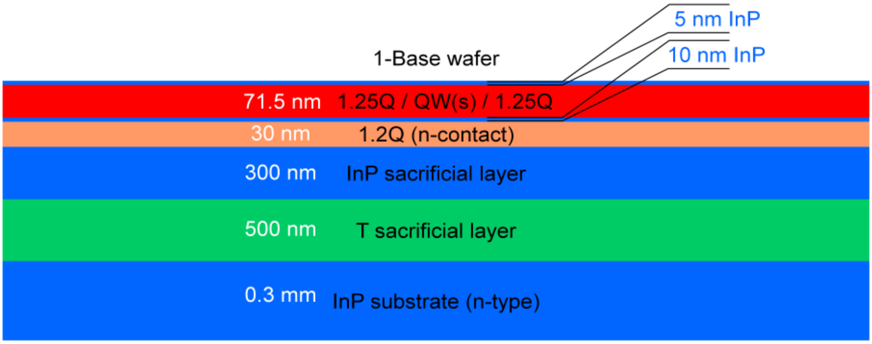

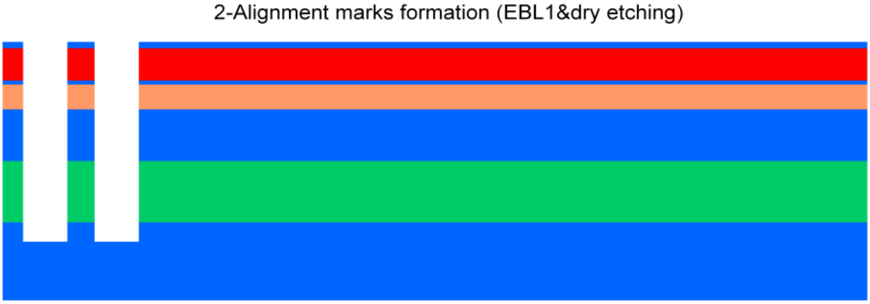

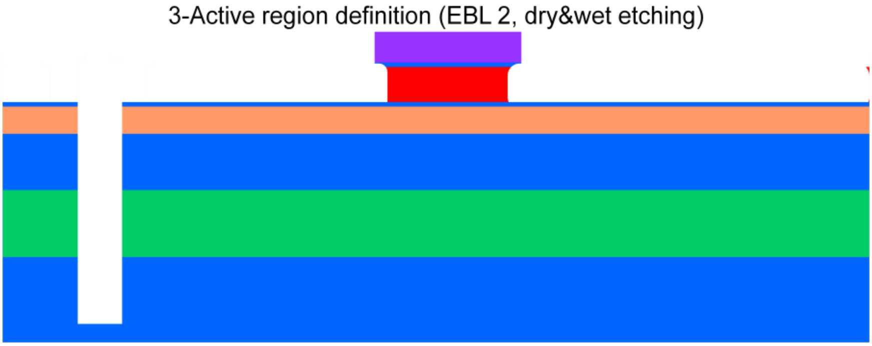

4-Regrowth1&2- Q (1.25) and AlInAs regrowth

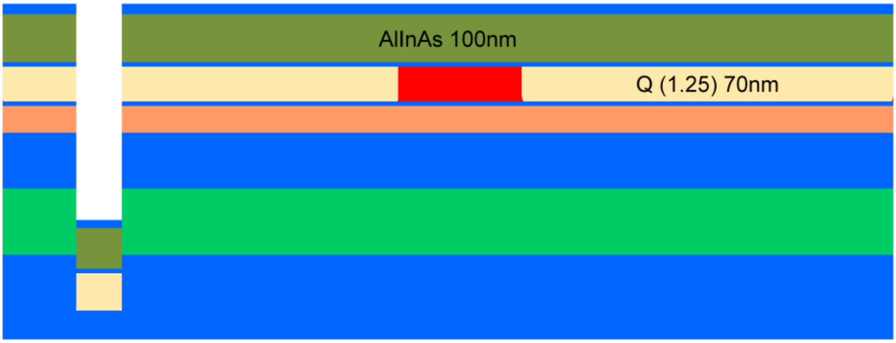

5-Selective removal of AlInAs (EBL-3&wet etching)

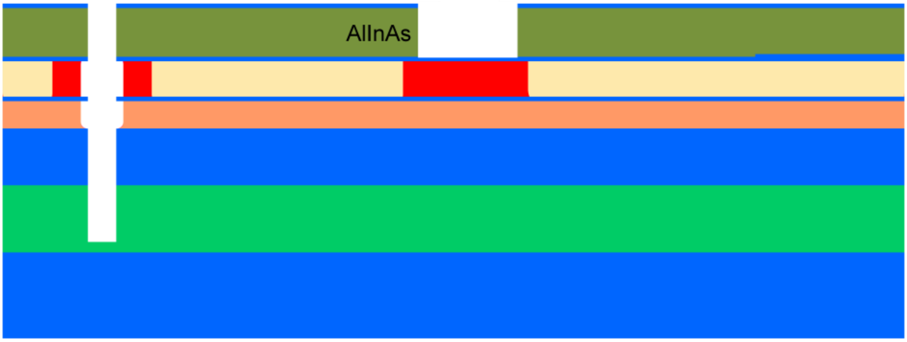

6-Regrowth3-P-InP, P-Q and p-InGaAs

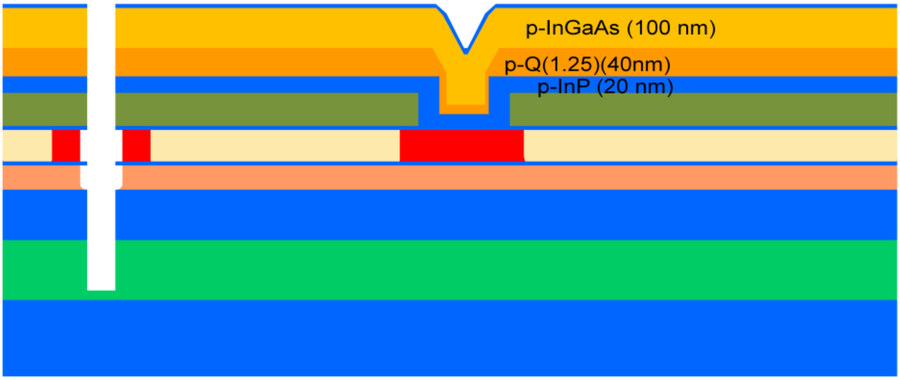

7-Selective removal of p-InGaAs (EBL 4& dry etching)

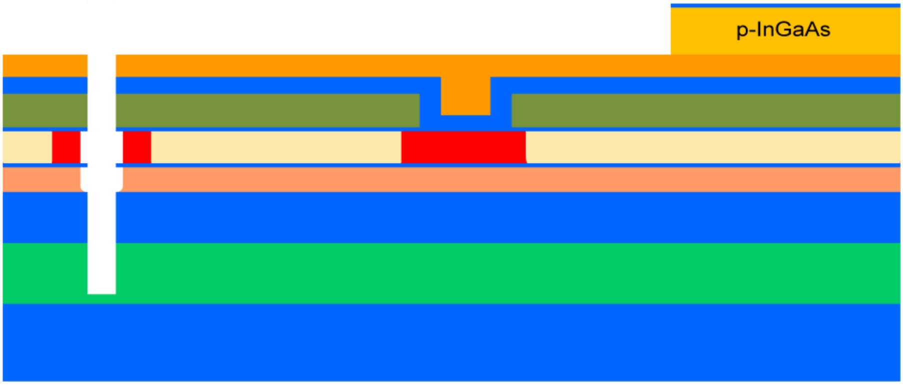

8-PhC holes, waveguide and oxidation grooves definition (EBL 5& dry etching)

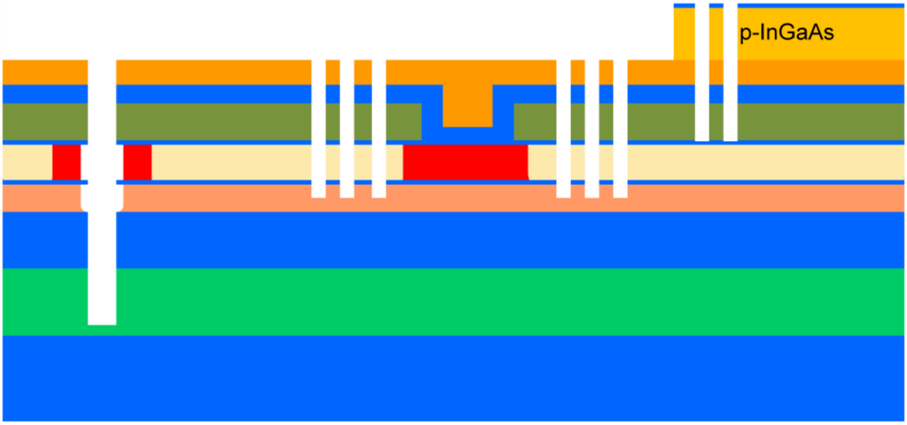

9-Grating definition (EBL 6& dry etching)

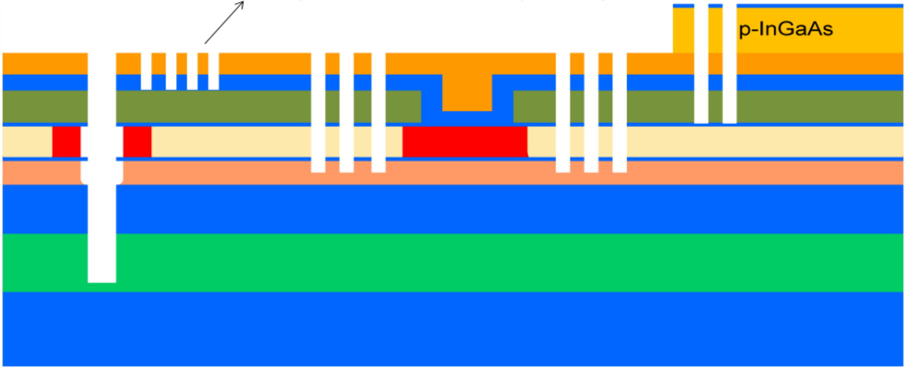

10-AlInAs oxidation

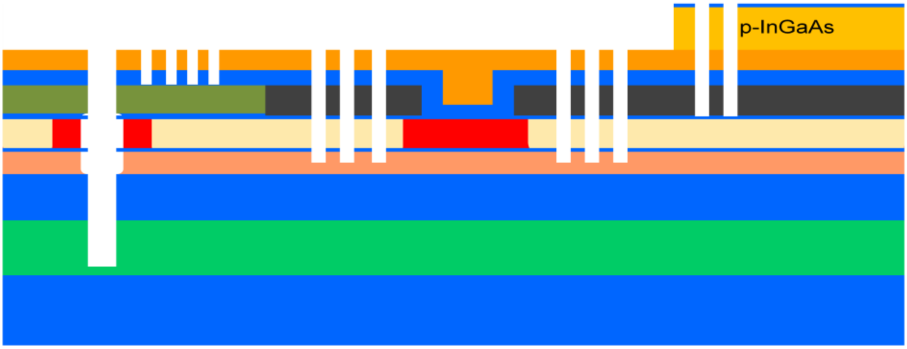

11-P-contact formation (EBL 7, metallization& lift off)

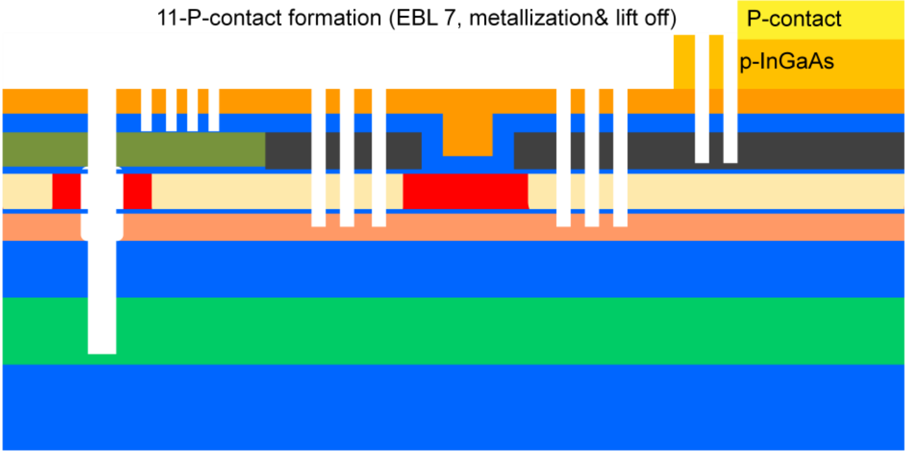

12-BCB bonding and substrate and sacrificial layer removal

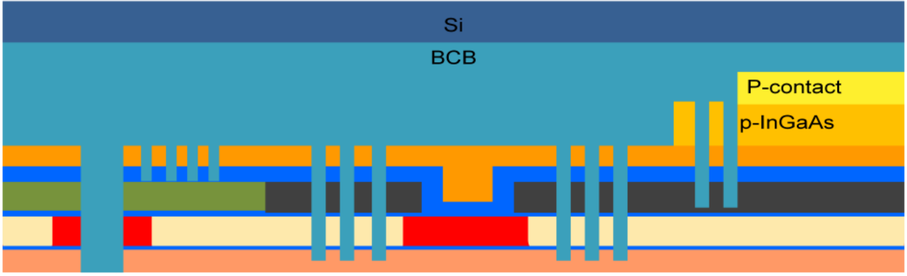

13-n-contact formation (EBL 8, metallization & lift off)

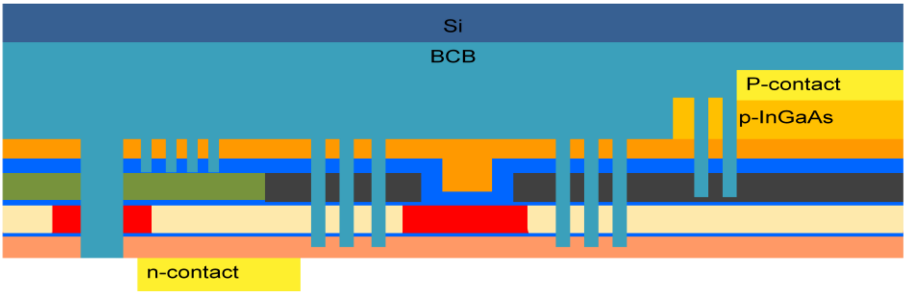

14-P-contact opening

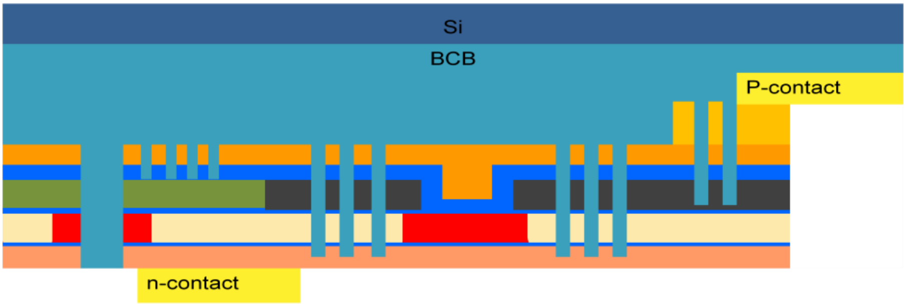

15-n-trench formation (EBL 10&dry etching)

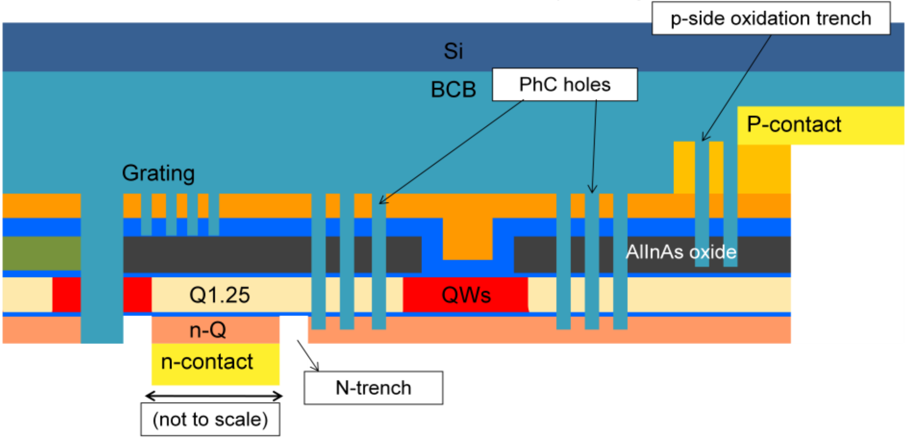

List of publications

- R. Zhang, F. Bordas, J.J.G.M. van der Tol, H. Ambrosius, G. Roelkens, M.A.Dundar and M.K. Smit, "Sub-micrometer Active-Passive Integration for InP-based Membranes on Silicon" Proc. ECIO 2010, Cambridge (UK), paper ThH1.
- R. Zhang, et al. "Oxidation of AlInAs for Current Blocking in a Photonic Crystal Laser", Proc. COMMAD 2010, Canberra (Australia), paper105.
- Bordas, F., Roelkens, G., Zhang, R., et al.: 'Compact passive devices in InP membrane on silicon', Opt. Express, accepted
- R. Zhang et al. (2009). Sub-micrometer active-passive integration for InP-based membranes on silicon. *Proceedings 14th Annual Symposium of the IEEE Photonics Benelux Chapter, 5-6 November 2009, Brussels, Belgium* (pp. 121-124).
- R. Zhang, Tol, J.J.G.M. van der, Thijs, P. & Smit, M.K. (2011). Design and simulation of a photonic crystal laser in InP-based membranes on silicon. In P. Bienstman, G. Morthier, G. Roelkens & et al. (Eds.), *Proceedings of the 16th Annual symposium of the IEEE Photonics Benelux Chapter, 01-02 December 2011, Ghent, Belgium* (pp. 169-172).
- J.J.G.M. van der Tol, R. Zhang, J. Pello, F. Bordas, G. Roelkens, H. Ambrosius, P. Thijs, F. Karouta and M.K. Smit, "Photonic Integration in Indium-Phosphide Membranes on Silicon" , IET Optoelectronics, Vol. 5, Iss. 5, pp. 218–225, 2011.
- R. Zhang, J.J.G.M. van der Tol, P. Thijs, and M.K. Smit, " Oxidation of AlInAs for Current Blocking in a Photonic Crystal Laser.", Proceedings of the 15th Annual symposium of the IEEE Photonics Benelux Chapter, , 18-19 November 2010, Delft, Netherland

- R. Zhang, J.J.G.M. van der Tol and M.K. Smit,” Design and simulation of a photonic crystal cavity in InP-based Membranes on Silicon. Proc. ECIO 2012, 17-19 April,2012 , Barcelona, Spain. paper 139
- Bordas, F., Roelkens, G., Zhang, R., Geluk, E.J., Karouta, F., Tol, J.J.G.M. van der, Veldhoven, P.J. van, Nötzel, R., Thourhout, D. Van, Baets, R.G.F. & Smit, M.K. (2009). “Compact passive devices in InP membrane on silicon.” *Proceedings of the 35th European Conference on Optical Communication (ECOC 2009) 20 - 24 September 2009, Vienna*(pp. 4.2.4-1/2).
- R. Zhang, S. Popov, S. Ricciardi, A. T. Friberg, S. Sergeyev,” Tolerance of polymeric microcavity laser against shape imperfections”, The topical conference on Nanophotonics, May 26-29,2008,Nanjing, China.
- R. Zhang, F. Bordas , J.J.G.M. van der Tol, P. Thijs, G. Roelkens ,T. de Vries and M.K. Smit, “Active-Passive Integration in III-V Membranes on Silicon”, International Nano-optoelectronics Workshop 2009, Stockholm and Berlin, Germany, August 2-16, 2009.
- R. Zhang, J.J.G.M. van der Tol and M.K. Smit,” Trap Model Analysis on Submicron Active-Passive Integration for InP-based Membranes on Silicon (IMOS)” *Proceedings of the 17th Annual symposium of the IEEE Photonics Benelux Chapter , 29-30 November 2012, Mons, Belgium*
- R. Zhang, S. Popov, S. Ricciardi, A. T. Friberg, S. dSergeyev,”Distortion tolerance against geometry imperfections in polymeric microcavity dye laser”, Journal of Nonlinear Optical Physics & Materials,2009.

Summary

Technology and Device Development for Active/Passive integration on InP_based Membrane on Si (IMOS)

The complexity of photonic integrated circuits has been raised significantly in the last few years, following Moore’s law in Photonics. To satisfy the need for even higher complexity, devices have to be made smaller and less power consuming. In this thesis, a new platform (InP-based Membrane on Silicon), which could potentially allow more compact integration capacity for the photonic integration circuits is described. As the early researches, this thesis focuses on the technology development, device design, fabrication and characterization of photonic components for the IMOS platform. The long term goal is to put this membrane on electronic chips (CMOS) to provide the high-speed on-chip data transport so that the Moore’s Law can be maintained even further.

First the first generation of IMOS passive components, such as waveguides and MMIs etc with small dimensions are demonstrated with good performance. These are the basic circuitry building blocks for future PICs on IMOS. The good performance and small dimensions of the first generation IMOS passive devices shows potential integrated complexity of IMOS platform. Next since PICs contain both passive and active components, a successful active-passive integration in IMOS is essential. In this thesis an active-passive integration with sub-micrometer active areas based on selective area regrowth technique is developed. The interface between active and passive areas shows good quality in terms of morphology. Moreover, it is found that in the sub-micrometer size active area, the degradation of the active material (InGaAsP QWs) due to processing is limited and controllable. Afterwards in order to realize inject carriers more efficiently into the IMOS active devices, a dielectric aperture is realized by AlInAs oxidation. The influence of temperature and time on the oxidation rate and the surface morphology are investigated. Moreover electrical measurements show that AlInAs oxidation gives an significant increase in the electrical resistance, which make this technique very promising for current confinement functions in the IMOS platform. And this technique developed in this thesis has already been applied to other IMOS active devices.

After the technology development, a line defect photonic crystal cavity is designed and simulated. Optical simulations results show that this cavity gives good performance in terms of quality factor and tolerance to manufacturing imperfections. Moreover, electrical simulation for the layer stack is also proceeded in order to inject the carriers in an efficient manner. Based on the electric simulation results, an optimized layer stack is proposed and it shows much smaller threshold current compared with the original one. In cooperation with SMARTPHOTONICS and Gent university, the manufacturing of the designed laser is pursued. However it turns out that multilayer regrowth is a very difficult process and after several trials only half of one sample survived all the regrowth steps. After the AlInAs oxidation, surprisingly no oxidized AlInAs was observed. It appears that the AlInAs layer is attacked by the HF solution which is used for removing the hard mask (SixNy). Without oxidized AlInAs layer as the current blocking layer, electrically pumped PhC lasers are not possible anymore, since short-circuiting will occur. However, optically pumped PhC lasers are still possible. After the definition of grating couplers, the sample is bonded on a host-Si wafer with BCB. The characterizations show that the devices don’t perform as we hoped for. The measurement shows a high optical loss. After checking in the SEM it is seen that many of photonic crystal cavities are damaged because of the force implemented during the bonding process. A further Micro PL measurements didn’t detect any emitting light from the remaining QWs which indicates that the QWs have already degraded due to the processing and stop emitting light.

All in all, the results presented in this thesis indicate the possibility of developing photonic components in IMOS for including both active and passive functions. Nevertheless quite a few issues need to be addressed and more technology developments are required to make IMOS a mature platform for the next generation PICs.

Acknowledgement

Finally, I come to the only part of thesis where I can be a little bit "emotional"☺.

First I would like to thank Meint, my promoter and the PhI group leader, for providing me with the opportunity to work in a highly skilled environment. I admire his optimism, efforts and contributions to the Photonic Integration, especially the ecosystem of InP-PICs. Privately I also appreciate all the efforts you and Marijke made for our PhI BBQ in your house☺!

I would like to express my sincere gratitude to my two "academic fathers": Dr. Fouad Karouta and Dr. Jos van der Tol. Fouad, thank you for give me the opportunity to work in the PhI group. Dat's heel jammer that we only worked together for three months before you left for Australia. Jos, thank you very much for "raising me up" academically. Your office door is always open to your students. I talk with a lot of PhD friends, not all of them are as lucky as me. I learned a lot of things from you: "Research is not just executing the tasks. More importantly it is about the understanding of what you are doing and why you are doing it". In the football pitch, we are also teammates. You always like winning and being the champions. Fortunately we made one Champion at the season of 2011☺.

I want to thank Fred Bordas, the first IMOS postdoc. Thank you for your training, support and help. The research work you've done, lay down the foundation for the IMOS technology. And it is my honor to represent these works in chapter 2 of this thesis in which I was involved is under your guidance.

I want to thank all my IMOS fellows. Jossolin, thank you for your help in my difficult time. You are also finishing this year. I wish you a perfect defense. Srivathsa, my indian friend, thank you for your help, especially in the wet etching test of AlInAs etching. Sorry that my foot frequently cross “China-India boundary”, but trust me I never want to invade your territory, neither our government☺. Yuqing thank you for your help and suggestions in the bonding and characterization and in my graduation. Longfei, I just realized we are triple Alumnus: Zhejiang University, KTH and TU/e. That’s not so common! Thank you for your help in my characterization. I wish you make a super fast “PhD”☺

Dzmitry, my dearest friend, you are always my terrible “headache” and you will always be my best friend☺

The sincere recognition shall be given to our lovely clean room technicians, Tijbbe, Barry, Erik Jan, Jeroen Bolk for their help during my cleanroom processing. Without your nice work, our chips can never been made successfully.

Mehmet, thank you very much for helping with Micro PL measurement in my first year. I am going to see u soon in ASML. Shahram, thank you for doing the bonding for me even if you are already busy with your own project. I hope also finish your PhD perfectly. Dominik, thank you very much for your help with the electrical simulations. I would like to acknowledge Jolanda Levering, the secretary of our group, thank you for your kind help and answers to all my questions. Jing, wish you success with your defense on the National Day of China, October 1st. I am going to see you soon in ASML. Saeed, Victor, Domenico, Manuela, Emil, Hadi, Alonso, Antonio, Valentina Sylwester, Dima, Deepak, Kasia, Stanislaw, Elton, Giovanni, Weiming, Xaveer and Erwin, Luc, Aura, Rui, it was really a pleasure to work with you all.

I would like to acknowledge my committee members, prof. Gunther Roelkens, Prof. Mike Wale, Dr. Huub Ambrosius, Prof. Andrea Fiore for all their suggestions to help me improve the quality of my thesis.

Privately I appreciate all the support from my friends in the Netherlands. Zhao Kang, my good friend, I was so lucky to meet you in Netherland. Yang yang, thank you for the help with my mask design. Feixiong, if you didn't introduce Tian to me, I am still single even today☺. Moreover, Feixiong, and Calvin, thanks a lot for helping with the thesis layout. Minda, thank you for carrying me to the hospital when I had that series football injury. Those who helped me, I will never forget! Tong Wei and Huang ling, Hui jianhua and Li jing, Wangyi and Yangxi, Gao Hao, Shiqi, Dujuan, Beibei, ... thank you all, I cannot imagine the life in Eindhoven without you guys. I also want to give my gratitude to my foreign friends. Robert, Marieke and our angle Jolieke, Tian and I are so luck to meet you in Netherlands. Thank you for all your hosting and veel success with your "green business", Robert☺. To my Indian friends: Abhinav, I wish you a success career in US. Prometheus I wish a successful PhD.

Last but certainly not the least, I would like to dedicate this thesis to my dearest parents and my fiancée Tian. As said in《Godfather》: Without families, a man can never be a real man".

Rui Zhang
July 30th, 2013
Eindhoven, the Netherlands

Curriculum Vitae

Rui Zhang was born in Shaanxi province, P.R. China in 1983. He received his Bachelor’s degree (Majored in Electronics) at 2006 from Beijing Institute of Technology, China. In 2006, based on the excellent records during the Bachelor study, he was recommended to Zhejiang University to continue Master’s study in the field of optical engineering. At 2007 he participated the “Joint Master programme” between Zhejiang University, China and Royal Institute of Technology (KTH), Sweden. At 2008 he received his Master degree (Photonics) from Royal Institute of Technology and Zhejiang University (Optical Engineering) respectively. His Master thesis is about the theoretical modeling of micron cavity dye lasers. From 2008, he joined the Photonic Integration group for his PhD researches. His main research field is to on the technology development, device design, fabrication and characterization of photonic components on InP_based membrane on Si (IMOS) for the next generation Photonic Integrated Circuits.